A&A 674, A37 (2023)
https://doi.org/10.1051/0004-6361/202243797
© The Authors 2023

Astronomy & Astrophysics
Special issue

Gaia Data Release 3

Gaia Data Release 3

Mapping the asymmetric disc of the Milky Way⋆

Gaia Collaboration: R. Drimmel[1,⋆⋆], M. Romero-Gómez[2], L. Chemin[3], P. Ramos[2,4], E. Poggio[5,1], V. Ripepi[6], R. Andrae[7], R. Blomme[8], T. Cantat-Gaudin[2,7], A. Castro-Ginard[9], G. Clementini[10], F. Figueras[2], M. Fouesneau[7], Y. Frémat[8], K. Jardine[11], S. Khanna[12,1], A. Lobel[8], D. J. Marshall[13], T. Muraveva[10], A. G. A. Brown[9], A. Vallenari[14], T. Prusti[15], J. H. J. de Bruijne[15], F. Arenou[16], C. Babusiaux[17,16], M. Biermann[18], O. L. Creevey[5], C. Ducourant[19], D. W. Evans[20], L. Eyer[21], R. Guerra[22], A. Hutton[23], C. Jordi[2], S. A. Klioner[24], U. L. Lammers[22], L. Lindegren[25], X. Luri[2], F. Mignard[5], C. Panem[26], D. Pourbaix[27,28,†], S. Randich[29], P. Sartoretti[16], C. Soubiran[19], P. Tanga[5], N. A. Walton[20], C. A. L. Bailer-Jones[7], U. Bastian[18], F. Jansen[30,⋆⋆⋆], D. Katz[16], M. G. Lattanzi[1,31], F. van Leeuwen[20], J. Bakker[22], C. Cacciari[10], J. Castañeda[32], F. De Angeli[20], C. Fabricius[2], L. Galluccio[5], A. Guerrier[26], U. Heiter[33], E. Masana[2], R. Messineo[34], N. Mowlavi[21], C. Nicolas[26], K. Nienartowicz[35,36], F. Pailler[26], P. Panuzzo[16], F. Riclet[26], W. Roux[26], G. M. Seabroke[37], R. Sordo[14], F. Thévenin[5], G. Gracia-Abril[38,18], J. Portell[2], D. Teyssier[39], M. Altmann[18,40], M. Audard[21,36], I. Bellas-Velidis[41], K. Benson[37], J. Berthier[42], P. W. Burgess[20], D. Busonero[1], G. Busso[20], H. Cánovas[39], B. Carry[5], A. Cellino[1], N. Cheek[43], Y. Damerdji[44,45], M. Davidson[46], P. de Teodoro[22], M. Nuñez Campos[23], L. Delchambre[44], A. Dell'Oro[29], P. Esquej[47], J. Fernández-Hernández[48], E. Fraile[47], D. Garabato[49], P. García-Lario[22], E. Gosset[44,28], R. Haigron[16], J.-L. Halbwachs[4], N. C. Hambly[46], D. L. Harrison[20,50], J. Hernández[22], D. Hestroffer[42], S. T. Hodgkin[20], B. Holl[21,36], K. Janßen[51], G. Jevardat de Fombelle[21], S. Jordan[18], A. Krone-Martins[52,53], A. C. Lanzafame[54,55], W. Löffler[18], O. Marchal[4], P. M. Marrese[56,57], A. Moitinho[52], K. Muinonen[58,59], P. Osborne[20], E. Pancino[29,57], T. Pauwels[8], A. Recio-Blanco[5], C. Reylé[60], M. Riello[20], L. Rimoldini[36], T. Roegiers[61], J. Rybizki[7], L. M. Sarro[62], C. Siopis[27], M. Smith[37], A. Sozzetti[1], E. Utrilla[23], M. van Leeuwen[20], U. Abbas[1], P. Ábrahám[63,64], A. Abreu Aramburu[48], C. Aerts[65,66,7], J. J. Aguado[62], M. Ajaj[16], F. Aldea-Montero[22], G. Altavilla[56,57], M. A. Álvarez[49], J. Alves[67], F. Anders[2], R. I. Anderson[68], E. Anglada Varela[48], T. Antoja[2], D. Baines[39], S. G. Baker[37], L. Balaguer-Núñez[2], E. Balbinot[12], Z. Balog[18,7], C. Barache[40], D. Barbato[21,1], M. Barros[52], M. A. Barstow[69], S. Bartolomé[2], J.-L. Bassilana[70], N. Bauchet[16], U. Becciani[54], M. Bellazzini[10], A. Berihuete[71], M. Bernet[2], S. Bertone[72,73,1], L. Bianchi[74], A. Binnenfeld[75], S. Blanco-Cuaresma[76], T. Boch[4], A. Bombrun[77], D. Bossini[78], S. Bouquillon[40,79], A. Bragaglia[10], L. Bramante[34], E. Breedt[20], A. Bressan[80], N. Brouillet[19], E. Brugaletta[54], B. Bucciarelli[1,31], A. Burlacu[81], A. G. Butkevich[1], R. Buzzi[1], E. Caffau[16], R. Cancelliere[82], R. Carballo[83], T. Carlucci[40], M. I. Carnerero[1], J. M. Carrasco[2], L. Casamiquela[19,16], M. Castellani[56], L. Chaoul[26], P. Charlot[19], V. Chiaramida[34], A. Chiavassa[5], N. Chornay[20], G. Comoretto[39,84], G. Contursi[5], W. J. Cooper[85,1], T. Cornez[70], S. Cowell[20], F. Crifo[16], M. Cropper[37], M. Crosta[1,86], C. Crowley[77], C. Dafonte[49], A. Dapergolas[41], P. David[42], P. de Laverny[5], F. De Luise[87], R. De March[34], J. De Ridder[65], R. de Souza[88], A. de Torres[77], E. F. del Peloso[18], E. del Pozo[23], M. Delbo[5], A. Delgado[47], J.-B. Delisle[21], C. Demouchy[89], T. E. Dharmawardena[7], P. Di Matteo[16], S. Diakite[90], C. Diener[20], E. Distefano[54], C. Dolding[37], H. Enke[51], C. Fabre[91], M. Fabrizio[56,57], S. Faigler[92], G. Fedorets[58,93], P. Fernique[4,94], Y. Fournier[51], C. Fouron[81], F. Fragkoudi[95,96,97], M. Gai[1], A. Garcia-Gutierrez[2], M. Garcia-Reinaldos[22], M. García-Torres[98], A. Garofalo[10], A. Gavel[33], P. Gavras[47], E. Gerlach[24], R. Geyer[24], P. Giacobbe[1], G. Gilmore[20], S. Girona[99], G. Giuffrida[56], R. Gomel[92], A. Gomez[49], J. González-Núñez[43,100], I. González-Santamaría[49], J. J. González-Vidal[2], M. Granvik[58,101], P. Guillout[4], J. Guiraud[26], R. Gutiérrez-Sánchez[39], L. P. Guy[36,102], D. Hatzidimitriou[103,41], M. Hauser[7,104], M. Haywood[16], A. Helmer[70], A. Helmi[12], M. H. Sarmiento[23], S. L. Hidalgo[105,106], N. Hładczuk[22,107], D. Hobbs[25], G. Holland[20], H. E. Huckle[37], G. Jasniewicz[108],

⋆ The data for Tables 1 and 2, Figs. 16, 17, 21, and B.1 are only available at the CDS via anonymous ftp at cdsarc.cds.unistra.fr (130.79.128.5) or via https://cdsarc.cds.unistra.fr/viz-bin/cat/J/A+A/674/A37

⋆⋆ Corresponding author: R. Drimmel, e-mail: ronald.drimmel@inaf.it

⋆⋆⋆ Retired.

Open Access article, published by EDP Sciences, under the terms of the Creative Commons Attribution License (https://creativecommons.org/licenses/by/4.0), which permits unrestricted use, distribution, and reproduction in any medium, provided the original work is properly cited.
This article is published in open access under the Subscribe to Open model. Subscribe to A&A to support open access publication.

A. Jean-Antoine Piccolo[26], Ó. Jiménez-Arranz[2], J. Juaristi Campillo[18], F. Julbe[2], L. Karbevska[36,109], P. Kervella[110], G. Kordopatis[5], A. J. Korn[33], Á Kóspál[63,7,64], Z. Kostrzewa-Rutkowska[9,111], K. Kruszyńska[112], M. Kun[63], P. Laizeau[113], S. Lambert[40], A. F. Lanza[54], Y. Lasne[70], J.-F. Le Campion[19], Y. Lebreton[110,114], T. Lebzelter[67], S. Leccia[6], N. Leclerc[16], I. Lecoeur-Taibi[36], S. Liao[115,1,116], E. L. Licata[1], H. E. P. Lindstrøm[1,117,118], T. A. Lister[119], E. Livanou[103], A. Lorca[23], C. Loup[4], P. Madrero Pardo[2], A. Magdaleno Romeo[81], S. Managau[70], R. G. Mann[46], M. Manteiga[120], J. M. Marchant[121], M. Marconi[6], J. Marcos[39], M. M. S. Marcos Santos[43], D. Marín Pina[2], S. Marinoni[56,57], F. Marocco[122], L. Martin Polo[43], J. M. Martín-Fleitas[23], G. Marton[63], N. Mary[70], A. Masip[2], D. Massari[10], A. Mastrobuono-Battisti[16], T. Mazeh[92], P. J. McMillan[25], S. Messina[54], D. Michalik[15], N. R. Millar[20], A. Mints[51], D. Molina[2], R. Molinaro[6], L. Molnár[63,123,64], G. Monari[4], M. Monguió[2], P. Montegriffo[10], A. Montero[23], R. Mor[2], A. Mora[23], R. Morbidelli[1], T. Morel[44], D. Morris[46], C. P. Murphy[22], I. Musella[6], Z. Nagy[63], L. Noval[70], F. Ocaña[39,124], A. Ogden[20], C. Ordenovic[5], J. O. Osinde[47], C. Pagani[69], I. Pagano[54], L. Palaversa[125,20], P. A. Palicio[5], L. Pallas-Quintela[49], A. Panahi[92], S. Payne-Wardenaar[18], X. Peñalosa Esteller[2], A. Penttilä[58], B. Pichon[5], A. M. Piersimoni[87], F.-X. Pineau[4], E. Plachy[63,123,64], G. Plum[16], A. Prša[126], L. Pulone[56], E. Racero[43,124], S. Ragaini[10], M. Rainer[29,127], C. M. Raiteri[1], M. Ramos-Lerate[39], P. Re Fiorentin[1], S. Regibo[65], P. J. Richards[128], C. Rios Diaz[47], A. Riva[1], H.-W. Rix[7], G. Rixon[20], N. Robichon[16], A. C. Robin[60], C. Robin[70], M. Roelens[21], H. R. O. Rogues[89], L. Rohrbasser[36], N. Rowell[46], F. Royer[16], D. Ruz Mieres[20], K. A. Rybicki[112], G. Sadowski[27], A. Sáez Núñez[2], A. Sagristà Sellés[18], J. Sahlmann[47], E. Salguero[48], N. Samaras[8,129], V. Sanchez Gimenez[2], N. Sanna[29], R. Santoveña[49], M. Sarasso[1], M. S. Schultheis[5], E. Sciacca[54], M. Segol[89], J. C. Segovia[43], D. Ségransan[21], D. Semeux[91], S. Shahaf[130], H. I. Siddiqui[131], A. Siebert[4,94], L. Siltala[58], A. Silvelo[49], E. Slezak[5], I. Slezak[5], R. L. Smart[1], O. N. Snaith[16], E. Solano[132], F. Solitro[34], D. Souami[110,133], J. Souchay[40], A. Spagna[1], L. Spina[14], F. Spoto[76], I. A. Steele[121], H. Steidelmüller[24], C. A. Stephenson[39,134], M. Süveges[135], J. Surdej[44,136], L. Szabados[63], E. Szegedi-Elek[63], F. Taris[40], M. B. Taylor[137], R. Teixeira[88], L. Tolomei[34], N. Tonello[99], F. Torra[32], J. Torra[2,†], G. Torralba Elipe[49], M. Trabucchi[138,21], A. T. Tsounis[139], C. Turon[16], A. Ulla[140], N. Unger[21], M. V. Vaillant[70], E. van Dillen[89], W. van Reeven[141], O. Vanel[16], A. Vecchiato[1], Y. Viala[16], D. Vicente[99], S. Voutsinas[46], M. Weiler[2], T. Wevers[20,142], Ł. Wyrzykowski[112], A. Yoldas[20], P. Yvard[89], H. Zhao[5], J. Zorec[143], S. Zucker[75], and T. Zwitter[144]

(Affiliations can be found after the references)

Received 15 April 2022 / Accepted 6 June 2022

ABSTRACT

Context. With the most recent *Gaia* data release, the number of sources with complete 6D phase space information (position and velocity) has increased to well over 33 million stars, while stellar astrophysical parameters are provided for more than 470 million sources, and more than 11 million variable stars are identified.

Aims. Using the astrophysical parameters and variability classifications provided in *Gaia* DR3, we selected various stellar populations to explore and identify non-axisymmetric features in the disc of the Milky Way in configuration and velocity space.

Methods. Using more about 580 000 sources identified as hot OB stars, together with 988 known open clusters younger than 100 Myr, we mapped the spiral structure associated with star formation 4−5 kpc from the Sun. We selected over 2800 Classical Cepheids younger than 200 Myr that show spiral features extending as far as 10 kpc from the Sun in the outer disc. We also identified more than 8.7 million sources on the red giant branch (RGB), of which 5.7 million have line-of-sight velocities. This later sample allows the velocity field of the Milky Way to be mapped as far as 8 kpc from the Sun, including the inner disc.

Results. The spiral structure revealed by the young populations is consistent with recent results using *Gaia* EDR3 astrometry and source lists based on near-infrared photometry, showing the Local (Orion) Arm to be at least 8 kpc long, and an outer arm consistent with what is seen in HI surveys, which seems to be a continuation of the Perseus arm into the third quadrant. The subset of RGB stars with velocities clearly reveals the large-scale kinematic signature of the bar in the inner disc, as well as evidence of streaming motions in the outer disc that might be associated with spiral arms or bar resonances. A local comparison of the velocity field of the OB stars reveals similarities and differences with the RGB sample.

Conclusions. This cursory study of *Gaia* DR3 data shows there is a rich bounty of kinematic information to be explored more deeply, which will undoubtedly lead us to a clearer understanding of the dynamical nature of the non-axisymmetric structures of the Milky Way.

Key words. Galaxy: kinematics and dynamics – Galaxy: structure – Galaxy: disk – Galaxy: bulge – catalogs

1. Introduction

The determination of the structure and kinematics of the Milky Way has been investigated for more than a century. Researchers have been able to describe the morphology of external galaxies using deep photometric surveys, but the structure and evolution of our own Galaxy still remains a mystery in many aspects. Difficulties rise from the fact that we are observing it from the inside and cannot construct a complete picture as we can for other galaxies. Until recently, it was necessary to infer large-scale characteristics of the Milky Way from a limited number of stars located in the solar neighbourhood. Efforts to overcome this limitation over the past two decades

† Deceased.

have progressed through a combination of large-scale photometric and spectroscopic surveys, such as the SDSS[1], RAVE[2], APOGEE[3], LAMOST[4], and GALAH[5]. *Gaia* has revolutionised this field, starting with the first *Gaia* data release (DR1), providing new insights into the stability of the Galactic disc (e.g. Gaia Collaboration 2018a; Antoja et al. 2018), its merger history (e.g. Helmi et al. 2018; Belokurov et al. 2018), and its structure through the discovery of new open clusters (e.g. Cantat-Gaudin et al. 2018; Castro-Ginard et al. 2019), to name a few. These results largely used the unprecedented number of about 7 million stars with 6D phase-space information in the second *Gaia* data release (DR2). The sample with Radial Velocity Spectrometer (RVS) measurements of Gaia Collaboration (2018a), with full 6D phase-space measurements, already showed that the disc of the Milky Way is not kinematically axisymmetric. Since then, a large number of contributions have been published that provided new results and characteristics of the Milky Way disc. We refer to Brown (2021) for an updated review of the Milky Way with *Gaia*, compared to a pre-*Gaia* view (e.g. Bland-Hawthorn & Gerhard 2016). The purpose of this contribution is to highlight the new information that is contained in the most recent *Gaia* data release regarding the structure of the Milky Way disc as revealed in configuration and velocity space.

Because it is rich in gas and has a disc structure, it was immediately expected that the Milky Way would have non-axisymmetric structures, like other spiral galaxies. Clear evidence of spiral structure from the distribution of local OB associations was reported in the 1950s (Morgan et al. 1953). Since then, the location of spiral arms has been studied using different tracers, such as giant molecular clouds, masers associated with high-mass star formation, H II regions, and young stars (OB stars, Cepheids, and young open clusters). Using parallaxes and proper motions of masers from the BESSEL survey, Reid et al. (2019) built logarithmic models of the Galactic spiral arms. The main arms identified in the model are the Norma-Outer arm, the Perseus arm, the Sagittarius-Carina arm (Sag-Car hereafter), and the Scutum-Centaurus arm. Another included arm is the Local Arm, which has been mostly considered as a minor feature with respect to the other arms listed above, as the name suggests. Maps showing the spiral arm segments of the Perseus, Local, and Sag-Car arms were produced by Poggio et al. (2021, hereafter P21) with a local OB sample, Cepheids, and young open clusters, and similarly by Hou (2021) with spectroscopically confirmed OB stars. These maps extended the arm segments towards the third and fourth quadrant, where masers are mostly absent. While some progress has been made in detailing the large-scale spiral structure as evidenced by star formation products, the dynamical nature of these arms and the mechanisms causing their formation remains unknown.

The Galactic bar in the inner disc is another long-known asymmetry of the Galaxy, whose kinematic signatures can be found from the inner to the outer disc. Like many external barred galaxies, the Galactic bar has a boxy-bulge shape, but its length, orientation angle, and angular velocity are not yet well constrained. In this instance, we now have a strong asymmetry in the stellar distribution, at least for the inner regions of the Milky Way. While some evidence of asymmetry in the form of spiral arms extending farther out from the bar in the stellar disc is seen in the near-infrared (NIR; Drimmel 2000; Churchwell et al. 2009), it has been challenging to find confirmation that the Milky Way hosts a density-wave-like structure in its kinematics. From earlier data releases, *Gaia* revealed that the velocity space of the stars is rich with structure. Most notably, the presence of arches and ridges in the $V_\phi - R$ space (galactocentric azimuthal velocity and radius) indicate large-scale kinematic phenomena in the Galactic disc (Antoja et al. 2018; Ramos et al. 2018; Fragkoudi et al. 2019; Khanna et al. 2019a). Disentangling these into identified resonances with the bar (Trick et al. 2019, 2021; Fragkoudi et al. 2019; Monari et al. 2019; Laporte et al. 2020) and/or spiral arms and/or external perturbations is an ongoing process (Hunt et al. 2019; Khanna et al. 2019a; Khoperskov & Gerhard 2022) and has proven to be difficult, mostly due to our detailed knowledge of the of stellar kinematics being contained within at most a few kiloparsecs of the Sun at most.

To assist us in understanding the kinematics of the Milky Way, comparisons between the observations and models will be important, and some of the previous works already mentioned have used this approach. Other recent works focused on how the spiral arms or a Galactic bar change the expected radial, tangential, and vertical kinematic maps (i.e. Faure et al. 2014; Monari et al. 2016, 2019; Hunt & Bovy 2018; Tepper-Garcia et al. 2021), based on either test particle simulations or pure N-body simulations. The observable used to compare with the data can either be directly mapping the average or dispersions of the velocity components on the Galactic plane, or checking the known moving groups in the solar neighbourhood or the ridges in the diagram of azimuthal velocity versus radius. In any case, an appropriate comparison of models to data must take the selection effects and uncertainties in the data into account. It is important to determine how they affect the prediction in contrast to ideal noise-free data. Romero-Gómez et al. (2015) showed the capabilities of the *Gaia* nominal mission in constraining the bar characteristics and constructing *Gaia* mock catalogues based on the *Gaia* science performance prescriptions for disc red clump stars.

In addition to the bar, spiral arms, and the Galactic warp, there has been some kinematic evidence of additional asymmetries that may indicate disequilibrium on a larger scale. With the RAVE survey, Williams et al. (2013) showed the presence of large-scale streaming motion in the disc and revealed differences above and below the Galactic plane. With SDSS data, Widrow et al. (2012) discovered similar wave-like compression or rarefaction features seen in both number density and bulk velocity, as well as towards the Galactic anticentre with LAMOST data (Carlin et al. 2013). The large-scale velocity field has also been mapped using highly precise line-of-sight velocities and distance tracers such as red clump giants (Bovy et al. 2015; Khanna et al. 2019b). (We adopt the term 'line-of-sight velocities' in place of 'radial velocities' for spectroscopically determined heliocentric velocity components in the direction of the source to avoid confusion with galactocentric 'radial velocity'). Their results indicated streaming motion on scales much larger than about 2.5 kpc, but the analysis was likely limited by incompleteness in data coverage. As a demonstration of the enhanced astrometry and photometry in *Gaia* EDR3, Gaia Collaboration (2021a) mapped the kinematics of the disc out to 14 kpc from the Galactic centre (GC). By selecting data in a narrow azimuthal range (20° about the Galactic anticentre), they studied the azimuthal and vertical velocity components without requiring line-of-sight velocities. The large sample in their study allowed the dissection of the stellar rotation curve in the young and in the older population of stars. Additionally, they showed that kinematic features (such as ridges in $V_\phi - R$ space) seen in the inner disc with *Gaia* DR2 extended out to at least $R = 14$ kpc. By separately considering the stars above and below the Galactic plane, they also revealed that the lower disc has predominantly higher rotational velocities than the upper disc.

[1] Sloan Digital Sky Survey (Jurić et al. 2008; York et al. 2000).
[2] RAdial Velocity Experiment (Steinmetz et al. 2020).
[3] Apache Point Observatory Galactic Evolution Experiment (Majewski et al. 2017; Jönsson et al. 2020).
[4] Large Sky Area Multi-Object Fiber Spectroscopic Telescope (Cui et al. 2012; Zhao et al. 2012).
[5] GALactic Archaeology with HERMES (De Silva et al. 2015).

Table 1. Summary of the mean parameters for the cluster sample log t: logrythm base 10 of the cluster age in years.

Cluster	ℓ [deg]	b [deg]	N	$\mu_{\alpha}*$ [mas yr^{-1}]	$\sigma_{\mu_{\alpha}*}$ [mas yr^{-1}]	μ_{δ} [mas yr^{-1}]	$\sigma_{\mu_{\delta}}$ [mas yr^{-1}]	ϖ [mas]	σ_{ϖ} [mas]	$v_{\rm los}$ [km s^{-1}]	$\sigma_{v_{\rm los}}$ [km s^{-1}]	$N_{v_{\rm los}}$	log t	n_0
ASCC 10	155.558	−17.801	147	−1.840	0.197	−1.396	0.157	1.530	0.047	−17.07	0.54	84	8.42	5
ASCC 101	67.978	11.608	106	0.940	0.228	1.200	0.250	2.548	0.052	−19.04	0.53	56	8.69	1
ASCC 105	62.860	2.025	148	1.429	0.147	−1.626	0.147	1.817	0.039	−16.83	0.62	71	7.87	3
						...								
UBC 1628	319.829	−4.227	10	−2.554	0.032	−2.840	0.043	0.552	0.013	−44.87	18.35	1	8.47	1

Notes. The full table is available at the CDS. N: number of probable members kept to compute astrometric parameters. $\sigma_{\mu_{\alpha}*}$, $\sigma_{\mu_{\delta}}$, and σ_{ϖ} are the observed standard deviations of the members. $\sigma_{v_{\rm los}}$: computed line-of-sight velocity uncertainty. $N_{v_{\rm los}}$: number of members used to compute the cluster line-of-sight velocity. n_0: number of members with an absolute magnitude brighter than 0.

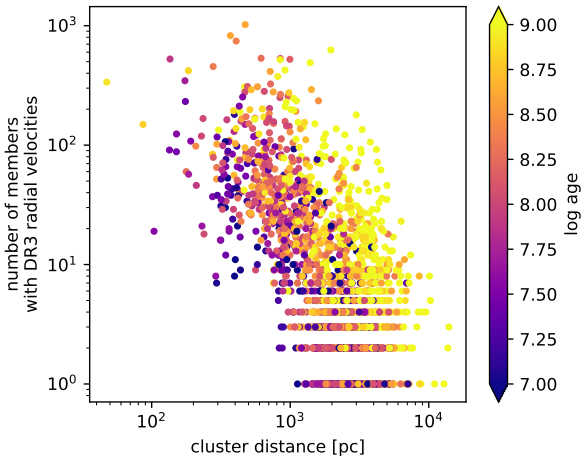


Fig. 1. Number of cluster members with available line-of-sight velocities in *Gaia* DR3 as a function of cluster distance and age.

In this paper, we show the extraordinary capabilities of *Gaia* DR3 to shed light on the structure and kinematic issues mentioned above. We use similar tracers as in other works, using only the new information provided in *Gaia* DR3 to select our samples, and then to map the density and kinematics over a large portion of the disc. The paper is organised as follows. Section 2 describes the selection of the four tracers used in this work, namely open clusters, Cepheids, OB stars, and red giant branch (RGB) stars, providing a description of their main properties. Section 3 describes the derivation of the positions, velocities, and uncertainties, including a short study of possible systematic effects. Section 4 maps the tracers into configuration space to show how they are distributed in relation to each other. Section 5 focuses on mapping the kinematics of the OB and RGB stars and on the information they contain about the bar and spiral arms. Section 6 discusses our results in context with other works and highlights the caveats and shortcomings that should be addressed in the future. In Sect. 7 we summarise our conclusions.

2. Selection of tracers

To map the asymmetry of the Galactic disc with *Gaia*, we selected young and old stellar populations: the former as the traditional tracer for the spiral structure that is used at optical wavelengths, where the surface brightness of disc galaxies like our Milky Way, are dominated by star formation products, while less-luminous older populations determine the mass distribution. The latest *Gaia* DR3 release allows us to select samples based on stellar parameters for the first time, which we used to select a sample of OB stars and red giants. The subset of sources with line-of-sight velocities (Katz et al. 2023) has full 6D phase-space information, allowing us to map the velocity field for these samples. In addition, we also investigate the distribution of open clusters and Classical Cepheids (DCEPs), for which we can derive excellent distances as well as ages. In this section we describe how we constructed each of these samples and how distances were derived for each.

2.1. Clusters

We used the list of probable members of the 2017 clusters studied by Cantat-Gaudin et al. (2020) with DR2 data. We obtained the DR3 `source_id` of these sources via the available cross-match table, and removed stars whose EDR3 astrometry revealed them to be outliers by more than 3σ. This list of members was supplemented with the stars from 628 clusters that were recently discovered by Castro-Ginard et al. (2022) in the EDR3 catalogue, and the members found by Tarricq et al. (2022) in the outskirts of 389 nearby clusters. Most of these clusters have associated ages estimated with an artificial neural network applied to the *Gaia* DR2 data (for those in Cantat-Gaudin et al. 2020) or EDR3 photometry, and 988 of them are younger than 100 Myr.

The median astrometric parameters (parallax and proper motion) were computed for all clusters and are provided in Table 1. Before calculating the median parallax, we corrected the individual parallaxes following the recipe provided by Lindegren et al. (2021). Given the statistical precision obtained from using a large number of (corrected) parallaxes, we estimated distances by inverting the median cluster parallax. The uncertainty on the bulk cluster astrometry was estimated as the quadratic sum of the statistical uncertainty (standard deviations in Table 1 divided by the square root of the number of members N) and the uncertainty due to small-scale correlations, taken as 10 µas in parallax and 25 µas yr^{-1} in proper motion (Vasiliev & Baumgardt 2021).

We also computed the median line-of-sight velocity for the 2162 clusters in which at least one member had a DR3 line-of-sight velocity. Out of the 988 clusters younger than 100 Myr, 698 have line-of-sight velocities from DR3. The bulk line-of-sight velocities were computed from an average of 48 members per cluster, although this number varied significantly with age and distance (Fig. 1). For comparison, in *Gaia* DR2, the line-of-sight velocities were only available for an average of 10 stars per cluster. We estimated the line-of-sight velocity uncertainty as

$$\sigma_{\rm los,cluster} = \sqrt{\frac{1}{\sum_{i=1}^{N}\left(\frac{1}{\sigma_{v_{{\rm los},i}}}\right)^2} + 0.5^2}, \quad (1)$$

where $\sigma_{v_{{\rm los},i}}$ are the nominal line-of-sight velocity uncertainties of the N cluster members, and 0.5 km s^{-1} is a conservative

estimate of the line-of-sight velocity accuracy estimated in DR2 (Deepak & Reddy 2018; Katz et al. 2019). Although future investigations of the DR3 line-of-sight velocities are likely to show improved systematics with respect to DR2, this conservative choice has no significant impact on the results of this paper.

2.2. Classical Cepheids

The sample of DCEPs adopted in this work is mainly based on the list of sources in the `vari_cepheid` table, which is published in DR3 as a result of the processing by the Specific Objects Study (SOS) pipeline that was specifically designed to validate and fully characterise DCEPs and RR Lyrae stars observed by *Gaia* (hereafter referred to as SOS Cep&RRL pipeline; see Clementini et al. 2016, 2019, 2023; Ripepi et al. 2023, for full details). This sample is composed of 3286 DCEPs belonging to the Milky Way, 1995 of which pulsate in the fundamental mode (F), 1097 in the first overtone (1O) and 194 are multi-mode (MULTI) pulsators. For these DCEPs, the SOS Cep&RRL pipeline provides pulsation periods, intensity-averaged magnitudes, peak-to-peak amplitudes, Fourier parameters, and other quantities whose full description can be found in Ripepi et al. (2023). The DR3 DCEPs sample was complemented with DCEPs taken by the recent compilations of Pietrukowicz et al. (2021) and Inno et al. (2021). We removed two additional multi-mode DCEPs pulsating in the second and third mode, as well as sources already in the DR3 DCEPs sample, and retained only objects with valid measurements of the mean magnitude in all three *Gaia* passbands and reliable proper motions. We find an additional 564 objects from Pietrukowicz et al. (2021) and 43 objects from Inno et al. (2021), with 27 objects in common. For these 27, we adopted the classifications and periods from Pietrukowicz et al. (2021), giving a total of an additional 580 DCEPs from the literature. However, an additional 81 literature DCEPs were removed as suspect binaries from their position in the period-Wesenheit diagram (see next section). We were therefore left with 486 and 13 DCEPs from the Pietrukowicz et al. (2021) and Inno et al. (2021) catalogues, respectively. The total sample is therefore composed of 3785 DCEPs. However, as we describe below, we further clipped this sample.

2.2.1. Distances and cleaning of the sample

An estimate of the distance to each DCEP in our sample was obtained directly from the definition of the distance modulus $w - W = -5 + 5\log d$, where w and W are the apparent and absolute Wesenheit magnitudes, respectively. The Wesenheit magnitudes are reddening free by construction, assuming that the extinction law is known (Madore 1982). The coefficient of the w magnitude has been derived in the *Gaia* bands on an empirical basis by Ripepi et al. (2019) and is defined as $w = G - 1.90 \times (G_{\rm BP} - G_{\rm RP})$. The absolute Wesenheit magnitude W was calculated using the period-Wesenheit-metallicity (PWZ) relation recently published by Ripepi et al. (2022),

$$W = (-5.988 \pm 0.018) - (3.176 \pm 0.044)(\log P - 1.0) - (0.520 \pm 0.090)[\mathrm{Fe/H}]. \quad (2)$$

To calculate the value of w for the DCEPs in our sample, we used different *Gaia* $(G, G_{\rm BP}, G_{\rm RP})$ magnitude data sets. For the DCEPs in the DR3 `vari_cepheid` table, the SOS Cep&RRL pipeline provides intensity-averaged magnitudes in the three *Gaia* bands, that is, magnitudes that are calculated to best resemble the magnitude that the DCEPs would have if they were non-variable stars. Instead, for the 499 literature DCEPs that are not in the DR3 `vari_cepheid` table, we only have the mean magnitudes estimated in the *Gaia* photometric processing (see Riello et al. 2021, for details) that are available for all sources in the *Gaia* source catalogue. However, using mean magnitudes in the *Gaia* source catalogue for the literature DCEPs sample does not bias our results because it was found that the difference between w magnitudes calculated in the two different ways is only -0.01 ± 0.03 mag (Ripepi et al. 2022). Obtaining reliable values of w is possible only for sources with reliable values of the G, $G_{\rm BP}$, and $G_{\rm RP}$ magnitudes. Objects with a magnitude close to or fainter than $G = 20$ mag are expected to have very poor $G_{\rm BP}$ photometry, thus resulting in unreliable mean $G_{\rm BP}$ magnitudes. We described how we cleaned the sample for this effect at the end of this section.

The other ingredient needed to calculate the distance to each DCEP is W, for which we need the period and iron abundance of each pulsator. The periods were taken from the `vari_cepheid` table or the literature, while the [Fe/H] values are more difficult to obtain. One of the products of *Gaia* DR3 is the iron abundances obtained with the Radial Velocity Spectrometer (RVS) on board *Gaia* (Gaia Collaboration 2023a), which are available in the `astrophysical_parameters` table published with DR3. Here we found spectroscopic values of [Fe/H] and their uncertainties for 949 DCEPs of the *Gaia* DR3 sample and for 27 of the literature DCEPs.

An estimate of the iron abundance for the remaining DCEPs was obtained adopting the metallicity gradient of the Milky Way disc as measured by Ripepi et al. (2022): $[\mathrm{Fe/H}] = (-0.0527 \pm 0.0022)R + (0.511 \pm 0.022)$ with rms = 0.11 dex (this estimate agrees with many other literature estimations; see Ripepi et al. 2022, for details). Even if not particularly precise, the iron abundances obtained in this way allow us to use Eq. (2) to derive reliable distances. According to the PWZ relation in Eq. (2), the impact on the distance to a DCEP produced by an uncertainty of 0.11 dex in metallicity is ∼2.5%, and even considering a conservative uncertainty of 0.2 dex in [Fe/H], the uncertainty on the distance would be a still tolerable 5%.

After the values of w and W were estimated as explained above, it was straightforward to calculate the distance to each DCEP in our sample and its uncertainty. This was calculated by error propagation: $\sigma_{\rm d} = 0.4605\sigma_\mu d$, where σ_μ is the uncertainty on the distance modulus, calculated by adding the uncertainties on w and W in quadrature, which in turn were estimated by propagating the uncertainties on the *Gaia* magnitudes for w, and for W from the uncertainties in the coefficients of Eq. (2), and the uncertainty on the iron abundance (the uncertainty on the periods is negligible).

An analysis of the derived distances and relative uncertainties revealed that many faint objects had unreliable distances and/or very large uncertainties as a result of the large photometric uncertainties, especially in the $G_{\rm BP}$ band. To provide a cleaner sample for further analysis, we experimented with the data and reached the conclusion that retaining only DCEPs with distances smaller than 30 kpc and a relative distance uncertainty better than 10% is a good compromise between precision and completeness. This selection removed 240 DCEPs from the *Gaia* DR3 sample and 230 literature DCEPs, leaving us with a total final dataset of 3306 DCEPs that were useful for further analysis. The G-magnitude distribution of this selected sample is shown in Fig. 2. The number of faint objects, especially from the literature sample, has now been drastically reduced.

2.2.2. Line-of-sight velocities

The spectra collected with the RVS spectrometer on board *Gaia* allow measuring time-series of the line-of-sight velocity (RV) values for millions of stars with a G magnitude brighter than

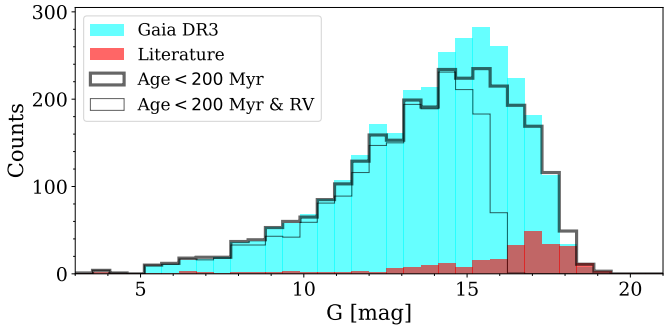


Fig. 2. Histogram of the G magnitude for the DCEP sample. We plot in cyan and red the histograms for the objects from the *Gaia* DR3 catalogue and those taken from the literature, respectively. The thick line shows the magnitude distribution of the DCEPs after the selection in age (<200 Gyr), while the thin line shows the histogram of the objects selected in age that also possess a line-of-sight velocity measurement. In the last two cases, the *Gaia* DR3 and literature samples were merged.

~15−16 mag (for details, see Sect. 6.4.8 of Sartoretti et al. 2022). In DR3 the RV time series are released for a selected sample of 774 DCEPs. (Fifteen and nine of these objects belong to the Large and Small Megallanic Clouds, respectively). For this subsample, the SOS Cep&RRL pipeline computed average RV values and relative uncertainties by fitting the RV curves folded according to the stars' periods and makes them available in the `vari_cepheid` table (see Clementini et al. 2023; Ripepi et al. 2023, for details). Nevertheless, for a much larger number of DCEPs in our sample, mean RVs estimated from the spectroscopic pipeline are available in the main `gaia_source` table. We verified whether these arithmetically computed mean RV values are usable for variable objects such as DCEPs by comparing the RV values in the `vari_cepheid` and the `gaia_source` tables. We found a perfect agreement with a mean difference of $0.6 \pm 6\,\mathrm{km\,s^{-1}}$ and no visible trend (see also Clementini et al. 2023). On this basis, we decided to use the `gaia_source` catalogue RVs for our DCEP sample. In total, we have RV estimates for 2059 DR3 and 67 literature DCEPs. The uncertainties on these values can be evaluated on the basis of Fig. 6.13 by Sartoretti et al. (2022).

2.2.3. Ages of DCEPs

It has been known for a long time that the DCEPs follow a period-age (PA) relation (see e.g. Bono et al. 2005; Anderson et al. 2016, and references therein). More recently, De Somma et al. (2021) devised a more accurate period-age-metallicity (PAZ) relation based on an updated theoretical pulsation scenario. Because the DCEP PWZ relation allows us to obtain individual accurate distances, it follows that the DCEP PAZ allows us to date any region in the Galactic disc in which a DCEP is present. To take advantage of this powerful tool, we adopted the following equation (see Table 9 of De Somma et al. 2021):

$$\log t = (8.423 \pm 0.006) - (0.642 \pm 0.004)\log P - (0.067 \pm 0.006)[\mathrm{Fe/H}], \quad (3)$$

with rms = 0.081; t, P, and [Fe/H] are the age (years), the period (days), and the iron abundance (dex). This relation is valid for F-mode pulsators, and it was calculated using evolutionary tracks including overshooting. As the PAZ relation is not available for 1O-mode DCEPs (see De Somma et al. 2021, for full details), we decided to fundamentalise their periods according to the Feast & Catchpole (1997) relation: $P_\mathrm{F} = P_\mathrm{1O}/(0.716-0.027\log P_\mathrm{1O})$, where P_F and P_1O are the F and 1O mode DCEP periods, respectively. In this way, we were able to calculate the ages for every DCEP in our sample. As we wished to use the DCEPs to trace the Milky Way arms, we decided to use only DCEPs younger than 200 Myr. Therefore the sample used in the following is composed of 2808 pulsators, 1948 of which also have line-of-sight velocity measurements. Table 2 shows selected properties of our selected DCEPs that are not published in other *Gaia* catalogues or papers.

2.3. OB stars

To select young stars on the upper main sequence, we used the effective temperatures provided in DR3, selecting stars with $T_\mathrm{eff} > 10\,000$ K. For hot stars, two sets of effective temperatures are provided in DR3 in general. One set is provided by a general stellar parameterizer from photometry (hereafter GSP-Phot; see Andrae et al. 2023), which estimates stellar parameters using the *Gaia* $G_\mathrm{BP}/G_\mathrm{RP}$ spectrophotometry, astrometry, and G band photometry. GSP-Phot makes different sets of parameter estimates using different stellar libraries, and for each source then chooses one of these as the best estimate. Here we use this set of best parameters as reported in the main *Gaia* source table. Another set of parameters is estimated from a software module (ESP-HS) that was optimised specifically for hot stars and uses the *BP*/*RP* spectrophotometry, without the astrometry, together with the RVS spectra if they are available as well (Creevey et al. 2023; Fouesneau et al. 2023). This second set of parameters is made available in the `astrophysical_parameters` table. Because of different quality filters for these different methods, *Gaia* sources may have one or both sets of effective temperatures, or remain without a temperature estimate. Only about half the sample of stars with $T_\mathrm{eff} > 10\,000$ K from either method has temperatures from both. From a detailed comparison of those sources with stellar parameters from one or both methods, we settled on the following criteria: For the stars with only GSP-Phot temperatures, we used the spectral type determined by ESP-HS for all sources with *Gaia BP*/*RP* spectrophotometry as an additional assurance of quality. That is, $T_\mathrm{eff} > 10\,000$ K and the ESP-HS spectral type flag set to O, B, or A; for the stars with only ESP-HS temperatures, we required that the effective temperature be in the range $10\,000 < T_\mathrm{eff} < 50\,000$ K, as it was found that the small fraction of sources with $T_\mathrm{eff} > 50\,000$ K are likely to be unreliable (Fouesneau et al. 2023); for sources with both sets of stellar parameters, we required that the effective temperature $T_\mathrm{eff} > 8000$ K for GSP-Phot and $T_\mathrm{eff} > 10\,000$ K for ESP-HS, letting the confirmation from GSP-Phot verify the sources with ESP-HS hotter than 50 000 K.

We note that we only used the effective temperature for the selection. A comparison of our temperatures against those found in the literature (Mathur et al. 2017; Abolfathi et al. 2018; Xiang et al. 2022) for stars in the range 8000−10 000K shows an rms difference smaller than 900 K and offsets smaller than 400 K. While the differences increase for higher measured T_eff, they remain small enough to that we remain confident that they should nevertheless be in our sample. We also note that the use of ESP-HS products for all three of the cases above effectively poses an apparent magnitude limit on this sample of 17.65 in G.

As a temperature selection introduces undesired subdwarfs and white dwarfs in our sample, we imposed the additional criterion $G + 5\log(\varpi/100) < 2. + 1.8(G_\mathrm{BP}-G_\mathrm{RP})$ to remove sources fainter than our target upper main-sequence stars. The colour term takes extinction and reddening into account, where 1.8 is approximately the slope of the reddening vector in

Table 2. Selected parameters for the DCEPs sample.

Source_id	ℓ (deg)	b (deg)	d (kpc)	μ (mag)	σ_μ (mag)	[Fe/H] (dex)	$\sigma_{[Fe/H]}$ (dex)	Flag	Source	logAge (dex)	σ_{logAge} (dex)
4060910068247394432	0.38444	1.96190	8.02	14.522	0.129	0.50	0.20	1	P21	8.594	0.016
4049125051634137600	0.45968	−5.42326	14.46	15.801	0.117	0.19	0.20	1	P21	8.706	0.015
4048895253682114432	0.47058	−6.65562	19.14	16.410	0.114	−0.05	0.20	1	Gaia_DR3	8.623	0.015
4056461478623363968	359.98638	−1.45395	15.81	15.995	0.157	0.11	0.20	1	Gaia_DR3	7.715	0.015

Notes. The full table is available at the CDS. The source_id is the *Gaia* source_id, ℓ and b are the galactic coordinates; d is the heliocentric distance in kpc; μ and σ_μ are the distance modulus and its uncertainty; [Fe/H] and σ[Fe/H] are the iron abundance and its uncertainty; flag = 0 or 1 means that the metallicity was taken from the astrophysical parameters or calculated from the metallicity gradient of the Galactic disc; source lists the provenance of the DCEP source: Gaia_DR3 means that the star is included in the *Gaia* DR3 `vari_cepheids` catalogue, P21 or Inno indicate that the DCEPs were taken from the Pietrukowicz et al. (2021) or Inno et al. (2021) catalogues, respectively; logAge and σ_{logAge} are the decimal logarithm of the age and its uncertainty.

$(G, G_{BP}-G_{RP})$ space. To capture distant sources with negative parallaxes, we rewrote this criterion in the form

$$(\varpi/100.)^5 < 10.^{(2.-G+1.8*(G_{BP}-G_{RP}))} \quad (4)$$

(see Appendix A for an example query). These criteria together give us 923 700 stars, but we find that outside the plane of the Galaxy, we have a significant number of stars in the direction of the Large (LMC) and Small (SMC) Megallanic Clouds, as well as a number of globular cluster members. We removed these contaminants by keeping only stars whose distance from the Galactic plane is smaller than 300 pc. This reduced the sample to 621 609 stars. Finally, we used the astrometric fidelity indicator f_a (with values $0 < f_a < 1$) of Rybizki et al. (2022) to remove sources with suspect astrometry, keeping stars with $f_a > 0.5$ as recommended in Zari et al. (2021). This last criterion removed only 7% of the sample, leaving us with a final sample of 579 577 stars, 91 836 (15.8%) of which have line-of-sight velocities. However, we note that the line-of-sight velocities of a fraction of them were estimated using an RVS spectral template with temperatures that are very different from the effective temperatures that were finally estimated for them, and therefore they are likely to have incorrect line-of-sight velocities (Blomme et al. 2023). Removing stars whose `rv_template_temp` is lower than 7000 K gives us 77 659 stars with valid line-of-sight velocities. Figure 3 shows the G magnitude distribution of our OB sample.

For the purpose of mapping, we need distance estimates for our sources. While *Gaia* provides parallaxes, about 40% of our sample have significant ($\sigma_\varpi/\varpi > 0.20$) parallax uncertainties, so that a simple inversion of the parallax cannot be considered reliable (Bailer-Jones 2015; Luri et al. 2018). Figure 4 shows the distribution of ϖ/σ_ϖ for our sample as well as for the subsample with line-of-sight velocities. For the subset of our stars with GSP-Phot parameters, *Gaia* DR3 also gives us distance estimates based on astrometry and photometry. However, 43% of our sample are sources that have only temperature estimates from ESP-HS, and therefore they lack a distance estimate from GSP-Phot. We therefore adopt the photogeo distances from Bailer-Jones et al. (2021) that are based on astrometric and photometric data, as recommended in Fouesneau et al. (2023), and which are available for our entire sample[6].

We mention that an alternative selection of high-fidelity OB stars is presented in Gaia Collaboration (2023b). The young B-stars from that sample are used for a basic modelling of the Milky Way rotation curve, which results in parameters that are consistent with the mean OB star V_ϕ curve derived below in Sect. 5.

[6] These distances can be found in the *Gaia* Archive as the external table, `external.gaiaedr3_distance`.

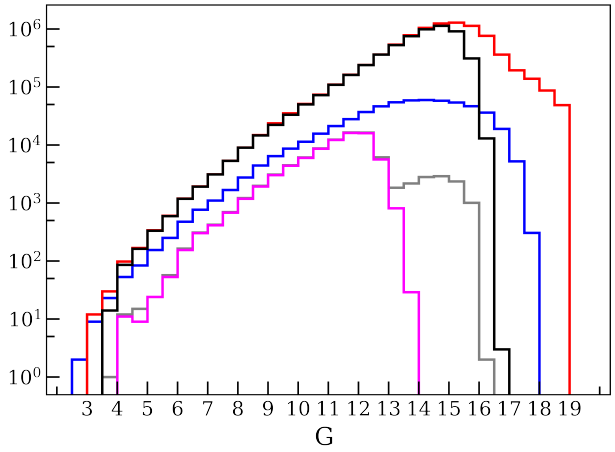


Fig. 3. G magnitude distribution of the selected giants (red) and OB (blue) samples. Black and grey histograms show the subsamples with line-of-sight velocities for the giants and OB stars, respectively. The magenta histogram are OB stars for which the line-of-sight velocities were estimated with templates with a $T_{eff} > 7000$ K. This sample was selected for mapping the velocities of the OB stars.

2.4. Giants

To select stars on the red giant branch (RGB), we used the effective temperatures and surface gravities provided in DR3, selecting stars with $3000 < T_{eff} < 5500$ K and $\log g < 3.0$, as provided by GSP-Phot (Andrae et al. 2023) in the main *Gaia* source table (see Appendix A for an example of the query used). These are given as the best set of parameters using a multi-spectral library approach, which for the RGB correspond to either the MARCS or PHOENIX libraries (Fouesneau et al. 2023). The Kiel diagram for these sources is shown in Fig. 5. We refer to this set as the full RGB sample, and it consists of 11 576 957 sources. The magnitude G distribution for the full RGB sample is shown in Fig. 3, together with the RGB sample with RVS line-of-sight velocities.

As in the OB sample, and in order to perform density and velocity maps, we needed to choose a distance estimator. The distribution of ϖ/σ_ϖ for the RGB sample is very similar to that of the full OB sample shown in Fig. 4, with about 39.5% of the giant sample having a $\varpi/\sigma_\varpi < 5$. All stars in the giant

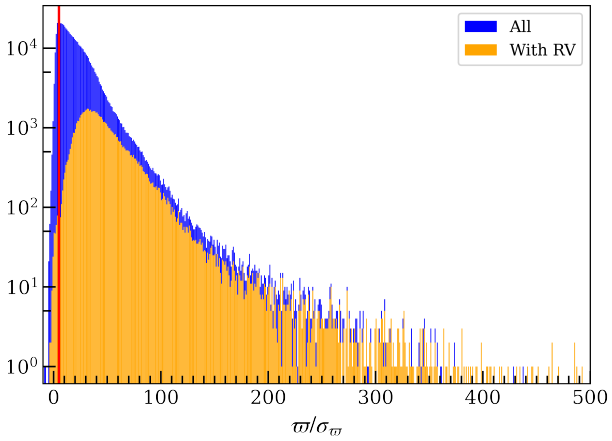


Fig. 4. Distribution of ϖ/σ_ϖ for the OB sample (blue) and the subsample with line-of-sight velocities (orange). The vertical red line is at $\varpi/\sigma_\varpi = 5$.

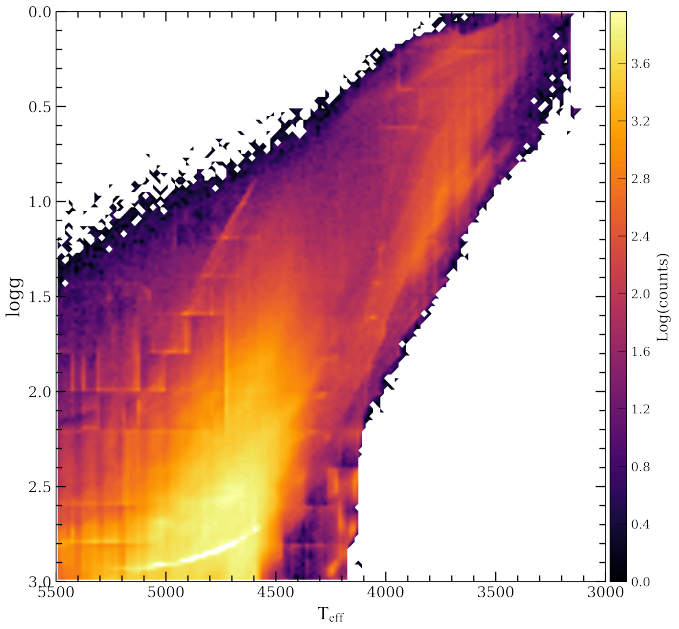


Fig. 5. Kiel diagram for the selected RGB sample with astrometry.

sample have GSP-Phot parameters. One option can therefore be to use the provided distance in *Gaia* DR3 (Andrae et al. 2023). Another option are the geo and photogeo distances from Bailer-Jones et al. (2021, hereafter CBJ2021). In order to choose the appropriate distance estimator for the large extent of the RGB sample, we cross-matched the recent catalogue of red clump stars by APOGEE DR17 (Abdurro'uf et al. 2022) with our RGB sample, using sky coordinates and a radius of 1 arcsec. This resulted in a common sample of 18 322. By comparing the absolute difference between the reported photometric distance and the three different possibilities mentioned above of the stars in common, we observe that the distance estimator with less bias and dispersion is the photogeo distance by Bailer-Jones et al. (2021; see Fig. 6). As shown in Babusiaux et al. (2023), the large parallax uncertainties and the prior used moreover causes the derived GSP-Phot distances to concentrate in density, forming a ring around the Sun at 2 kpc. This makes them inappropriate for studying the inner disc. Therefore, and as in the OB sample, we adopted the photogeo distance estimate for the RGB sample.

In addition, as in the selection of OB stars, we kept only sources with good astrometry, that is, with an astrometric fidelity $f_a > 0.5$. This criterion removed only 14% of the sample, leaving us with a sample of 9 959 807 stars, 6 586 329 of which have line-of-sight velocities.

We found that the above selection also included many sources from the Large and Small Magellanic Clouds, as well as a number of globular clusters. Because the goal of the paper is to study the Galactic disc, we performed an additional cut on the altitude with respect to the Galactic plane, that is, $|Z| < 1$ kpc. We also explored whether this selection might include sources from the Sagittarius dwarf galaxy, which could bias our kinematic study. We find no evidence of Sagittarius dwarf sources in the proper motion map, and while red clump stars in the dwarf galaxy have a magnitude range of 17−18 mag (e.g. Antoja et al. 2020), which falls at the faint end of our sample, they are a negligible fraction in our full sample and are not expected at all in the sample with RVS line-of-sight velocities, so we did not attempt to remove them. The final RGB sample consists then of 8 727 344 sources, with 5 730 578 with RVS line-of-sight velocities.

In Table 3 we summarise the number of stars in each of the selected tracers we used throughout the paper. We provide the number of sources with full 5D astrometry and the subsample including 6D phase-space information (astrometry and line-of-sight velocities).

3. From observations to 6D phase space

3.1. Mapping to configuration space

To map our tracers in a 3D Cartesian coordinate space, we must transform astrometric angular measurements (ϖ, α, δ) into associated lengths. While each of these measurements have associated uncertainties, we are here concerned with objects reaching large distances (i.e. small parallaxes). In this case, our positional uncertainties are completely dominated by the uncertainties in parallax (whose associated positional uncertainty is proportional to the square of the distance), and we can safely ignore the uncertainties (and correlations) with the angular positional measurements. Our problem is now just reduced to determining the heliocentric distance to each tracer and its uncertainty. In the previous section, the distance estimate adopted for each tracer population is described: for the OB and RGB samples, we adopted the photogeo distances of CBJ2021, for the clusters, we took the inverse of their median parallax, and for the Cepheids, we used a photometric distance based on the Leavitt law, as detailed in Sect. 2.2.

It has been known for a long time that some Milky Way DCEPs are members of OCs (see e.g. Anderson et al. 2013, and references therein). It is therefore useful to compare the photometric distances inferred for DCEPs with those of their host OCs, which are based on the median parallax of the OC members. To select possible DCEPs belonging to OCs, we cross-matched the DCEP list with that of all the known OC members. The cross-match was carried out using *Gaia* identifiers and returned 25 matches. The distance comparison is shown in Fig. 7. The overall agreement is very good, approximately below 1σ in all the cases, except for the farthest OC of the sample, namely UBC 608. The discrepancy for this source is smaller than 1.5σ, however.

From the heliocentric distances d, we can easily derive heliocentric Cartesian coordinates (x, y, z) under the assumption of a (non-relativistic) 3D Euclidean geometry. Because we assumed the positions to be known, we took advantage of the provision of (l, b) of each tracer in the *Gaia* archive and used the usual

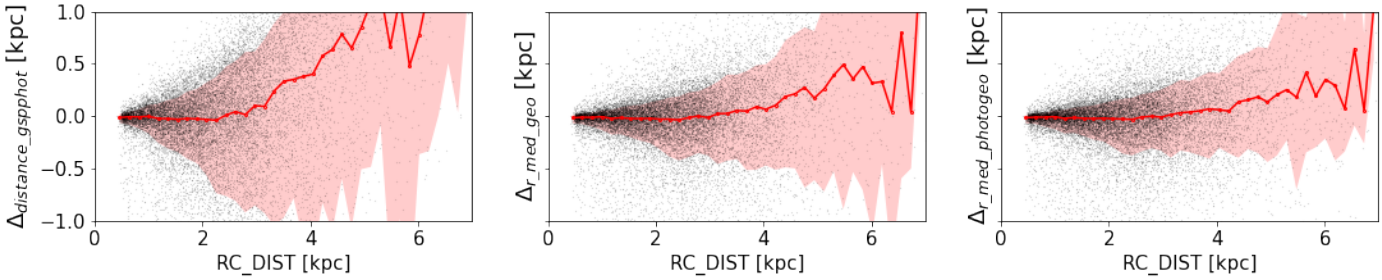


Fig. 6. Absolute difference between the APOGEE red clump distance and three distance estimators considered in this work, GSP-Phot (*left*), geo (*middle*), and photogeo (*right*).

Table 3. Number of stars in each sample according to the selected tracer.

Sample	Astrometry	6D
Clusters (all ages)	2681	2162
Young clusters (age < 100 Myr)	988	698
Classical Cepheids (DCEP)	3312	2127
Classical Cepheids (age < 200 Myr)	2812	1949
Young field stars (OB)	579 577	77 659
Giant field stars (RGB)	8 727 344	5 730 578

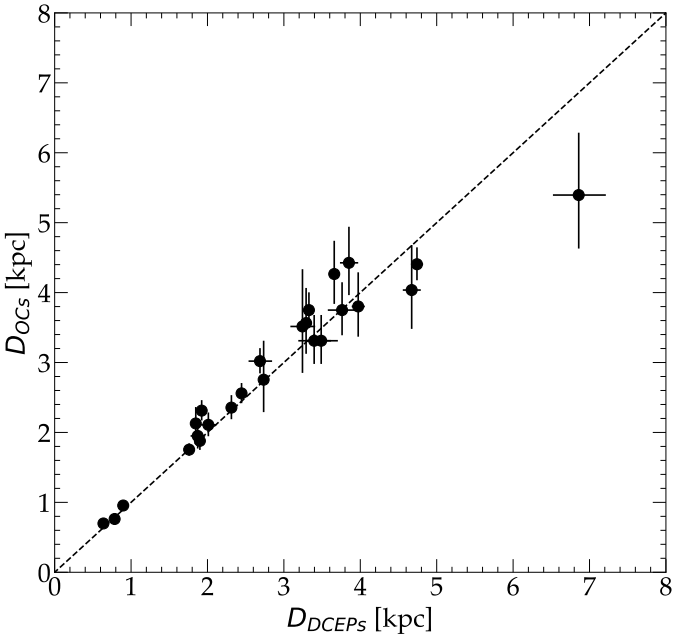


Fig. 7. Comparison of the distances calculated for DCEPs and their host OCs.

transformations,

$$\begin{pmatrix} x \\ y \\ z \end{pmatrix} = d \begin{pmatrix} \cos b \cos l \\ \cos b \sin l \\ \sin b \end{pmatrix}, \tag{5}$$

where positive x is towards the Galactic centre. Galactocentric Cartesian coordinates are then typically derived as a simple translation of the origin,

$$\begin{pmatrix} X \\ Y \\ Z \end{pmatrix} = \begin{pmatrix} x - R_\odot \\ y \\ z + Z_\odot \end{pmatrix}, \tag{6}$$

where $R_\odot$ and $Z_\odot$ are the distance of the Sun from the Galactic centre and above the Galactic ($Z = 0$) midplane.

For our choice of $R_\odot$, we used the geometrical determination based on the line-of-sight velocity and relative astrometry of the resolved SagA* S2 binary, as measured by the latest contribution of the GRAVITY Collaboration (GRAVITY Collaboration 2022), namely $R_\odot = 8277 \pm 9\,(\mathrm{stat}) \pm 30\,(\mathrm{sys})$ pc, although we note that this value disagrees within the uncertainties with the independent determination of $R_\odot$ by Do et al. (2019) ($7.959 \pm 59\,(\mathrm{stat}) \pm 32\,(\mathrm{sys})$) and also with their previous determinations, indicating that our assumed $R_\odot$ may in fact be in error by as much as 200 to 300 parsecs. Our adopted value of $R_\odot$ assumed that the position of SagA* marks the Galactic centre, which is expected from dynamical considerations: A supermassive black hole not already at the centre of a large stellar system will eventually migrate to the centre due to dynamical friction (Gualandris & Merritt 2008). Most recently, Leung et al. (2022) have independently determined $R_\odot = 8.23 \pm 0.12$ kpc based on observed stellar kinematics towards the Galactic centre. This value is consistent with our assumed value, but with a more realistic estimate of its uncertainty. For mapping in configuration space, any systematic error in $R_\odot$ only results in a trivial offset in the maps. However, as discussed further in Sect. 3.4, it can introduce rather undesirable effects when the velocities are mapped in galactocentric cylindrical coordinates.

The transformation into galactocentric coordinates (Eq. (6)) is an approximation because it assumes that the $b = 0$ and $Z = 0$ plane are parallel to each other. While this was the original intent when the galactic coordinate system was defined (Gum et al. 1960; Blaauw et al. 1960), there may well be a residual offset due to the height of the Sun above the $Z = 0$ plane. It was already noted at the time that determinations of $Z_\odot$ from hydrogen radio emission do not coincide with those based on nearby stellar samples. In their pre-*Gaia* review of our knowledge of the Milky Way, Bland-Hawthorn & Gerhard (2016) found that estimates for the distance of the Sun above the midplane fall between 20 and 30 pc, while more recent estimates have generally been smaller (Yao et al. 2017; Widmark 2019; Anderson et al. 2019; Reid et al. 2019). However, evidence of vertical oscillations in the disc of the Milky Way (Bennett & Bovy 2019) and evidence of its disequilibrium state (Antoja et al. 2018) rather complicates this discussion because the local stellar mid-plane of the Galaxy might very well not coincide with a $Z = 0$ plane as defined by the average vertical density distribution of the inner disc. Different vertical modes may be present in the gas (and star formation tracers) and in the stars, or even between different stellar populations, explaining some of the observed variance between the different determinations of $Z_\odot$. As a case in point, using a very local sample of stars, Gaia Collaboration (2021b) reported that $Z_\odot$ varies from -4 pc to 15 pc for young to older stellar

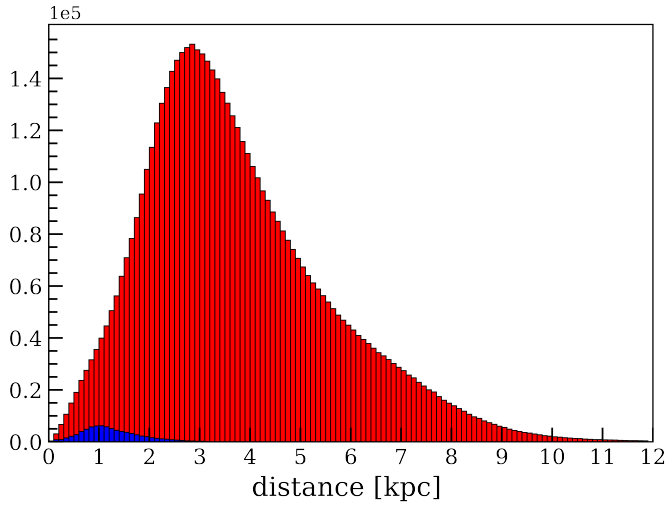


Fig. 8. Distribution of the heliocentric distances from Bailer-Jones et al. (2021) of the RGB (red) and OB stars (blue) with line-of-sight velocities.

populations. The observed small negative offset of SagA* from $b = 0$ also suggests that there is a residual tilt of $\delta\theta$ between the galactic ($b = 0$) plane and the Galactic ($Z = 0$) plane of about only 0.1° (see also the discussion in Bland-Hawthorn & Gerhard 2016). However, since for mapping the large-scale asymmetries in the disc we are primarily concerned with the positions and velocities of our tracers in the (X, Y) plane, where the effect of this tilt is negligible, we conveniently assume $Z_\odot = 0$, so that $Z = z$.

3.2. Mapping to velocity space

To map the velocities, we must now use the spectroscopically measured line-of-sight velocities v_r together with the measured proper motions and the distance estimator described in the previous section. As mentioned above, the OB and RGB samples with measured line-of-sight velocities contain 77 659 and 5 730 578 sources, respectively. In addition, the brighter magnitude limit of the OB sample with line-of-sight velocities also means that the area that can be mapped by the OB stars is much smaller than that of the RGB sample (see Fig. 8).

The relative velocity components in the heliocentric Cartesian coordinates defined by Eq. (5) are

$$\boldsymbol{v}_\mathrm{rel} = \begin{pmatrix} u \\ v \\ w \end{pmatrix} = A'_G\, A \begin{pmatrix} 4.74047\ \mu_{\alpha^*}\ d \\ 4.74047\ \mu_\delta\ d \\ v_\mathrm{r} \end{pmatrix}, \tag{7}$$

where $(\mu_{\alpha^*}, \mu_\delta)$ are the proper motion components, v_r is the line-of-sight (i.e. radial) velocity, A'_G is the transformation matrix from equatorial to galactic coordinates, as given by Eq. (4.62) of the *Gaia* EDR3 online documentation[7], and the matrix A is the normal triad at the star,

$$A = \begin{pmatrix} -\sin\alpha & -\sin\delta\cos\alpha & \cos\delta\cos\alpha \\ \cos\alpha & -\sin\delta\sin\alpha & \cos\delta\sin\alpha \\ 0 & \cos\delta & \sin\delta \end{pmatrix}. \tag{8}$$

Alternatively, the astrometry might first be converted into galactic coordinates by removing A' from Eq. (7) and substituting the proper motion components in ICRS coordinates with those in galactic coordinates, and then computing $\boldsymbol{v}_\mathrm{rel}$ from the proper motions in galactic coordinates. In this case, the triad (Eq. (8)) would be in (l, b) rather than (α, δ).

We note that for the line-of-sight velocities v_r of the OB stars, we applied the following correction (as prescribed in Blomme et al. 2023):

$$v_\mathrm{los} = \texttt{radial_velocity} - 7.98 + 1.135\texttt{grvs_mag}. \tag{9}$$

This was applied to stars for which $8500 \leq \texttt{rv_template_teff} \leq 14\,500$ K and $6 \leq \texttt{grvs_mag} \leq 12$.

The velocities $\boldsymbol{v}_\mathrm{rel} = (u, v, w)$ derived above are relative to the Sun. To place them in a galactocentric reference frame, we must add the solar velocity with respect to the Galactic centre, $\boldsymbol{v}_\odot$,

$$\boldsymbol{v}_* = \boldsymbol{v}_\mathrm{rel} + \boldsymbol{v}_\odot. \tag{10}$$

Traditionally, the solar velocity $\boldsymbol{v}_\odot$ has been estimated from the solar motion with respect to a local standard of rest (LSR) and an adopted value of the velocity of the LSR, which commonly is assumed to be in circular motion about the Galactic centre. However, with the recent precise measurement of the proper motion of the SagA*, together with $R_\odot$, the azimuthal and vertical components of the solar galactocentric velocity can be derived in a more direct and precise way. From Reid & Brunthaler (2020), we have $(\mu_l, \mu_b) = (-6.411 \pm 0.008, -0.219 \pm 0.007)$ mas yr^{-1} for the proper motion of SagA*, which together with $R_\odot$ gives the solar Y and Z-velocity components. The same reduction of the SagA* S2 data by the GRAVITY Collaboration that yielded $R_\odot$ also yields the line-of-sight velocity towards SagA*, interpreted as the reflex motion of the solar velocity towards the Galactic centre. This results in

$$\boldsymbol{v}_\odot = \begin{pmatrix} 9.3 \pm 1.3 \\ 251.5 \pm 1.0 \\ 8.59 \pm 0.28 \end{pmatrix} \mathrm{km\,s^{-1}} \tag{11}$$

if we assume that SagA* is stationary with respect to the Galactic centre. (see Drimmel & Poggio 2018, for further discussion on this approach to deriving $\boldsymbol{v}_\odot$). The uncertainties in $\boldsymbol{v}_\odot$ as well as any error in our adopted $R_\odot$ gives us a systematic error common to all our galactocentric velocities $\boldsymbol{v}_*$. See Sect. 3.4 below for further discussion.

The (u, v, w) components of our galactocentric velocities $\boldsymbol{v}_*$ are rigorously in the same coordinate system as defined by Eq. (5), that is, they are slightly tilted with respect to a (U, V, W) coordinate system whose U–V plane is parallel to the mean $Z = 0$ plane of the Galaxy by the angle $\delta\theta$ mentioned above, if $Z_\odot \neq 0$. However, the systematic error introduced by ignoring this (unknown) tilt is much smaller than the systematic error introduced by the uncertainties in $\boldsymbol{v}_\odot$.

Assuming $Z_\odot = 0$, the galactocentric radial and azimuthal velocities can be found from

$$\begin{aligned} v_R &= -u\cos\phi + v\sin\phi \\ v_\phi &= u\sin\phi + v\cos\phi \\ v_z &= w, \end{aligned} \tag{12}$$

where ϕ is the galactocentric azimuth, taken as positive in the direction of Galactic rotation,

$$\phi = \arctan\left(\frac{Y}{-X}\right) = \arctan\left(\frac{d\cos b\sin l}{R_\odot - d\cos b\cos l}\right), \tag{13}$$

making our (R, ϕ, z) galactocentric cylindrical coordinates a left-handed system.

[7] https://gea.esac.esa.int/archive/documentation/GEDR3/Data_processing/chap_cu3ast/sec_cu3ast_intro/ssec_cu3ast_intro_tansforms.html#SSS1

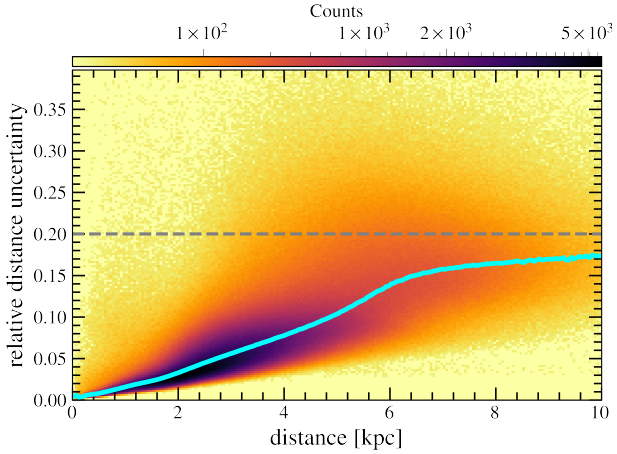


Fig. 9. Relative distance uncertainties of the individual sources, as a function of distance, for the RGB sample with radial velocities. The blue curve shows the median in bins of 50 pc.

3.3. Propagation of uncertainties

To estimate the uncertainties in positions and velocities from the formal errors in astrometry, we chose to concatenate the Jacobian matrices of the consecutive transformations necessary to move from the initial reference frame to the desired one. This means that we implicitly linearised the functions that allow us to convert astrometry into positions and velocities. In other words, we simplified the sequence of non-linear transformations (e.g. see Eqs. (7), (12), and (13)) that convert the coordinates in one reference frame, $\boldsymbol{x}_1$, into the coordinates in another frame, $\boldsymbol{x}_2$, with a single matrix product of the form

$$\boldsymbol{x}_2 = J\boldsymbol{x}_1, \tag{14}$$

by taking only the linear term of the Taylor expansion of the transforming functions. In this case, J corresponds to the Jacobian matrix of the functions used to transform from one frame into the next,

$$J_{i,j} = \frac{\partial f_i(\boldsymbol{x})}{\partial x_j}, \tag{15}$$

where f_i is the function that calculates the ith component of the vector $\boldsymbol{x}_2$ in the desired coordinate frame given the vector $\boldsymbol{x}_1$ in the original coordinate frame.

In practice, we first constructed the covariance matrix in the frame of the *Gaia* astrometry using the proper motion and line-of-sight velocity uncertainties and their associated correlations. As said above, we neglected the uncertainties in sky position, and consequently, all involved terms were set to zero. At the same time, we replaced the uncertainty in parallax with the uncertainty on our distance estimate, σ_d (discussed below), and set the corresponding correlations to zero. The resulting initial covariance matrix for any source is, thus,

$$\Sigma_\mathrm{ICRS} = \begin{pmatrix} 0 & 0 & 0 & 0 & 0 & 0 \\ 0 & 0 & 0 & 0 & 0 & 0 \\ 0 & 0 & \sigma_\mathrm{d}^2 & 0 & 0 & 0 \\ 0 & 0 & 0 & \sigma^2_{\mu^*_\alpha} & \rho_{\mu^*_\alpha\mu_\delta}\sigma_{\mu^*_\alpha}\sigma_{\mu_\delta} & 0 \\ 0 & 0 & 0 & \rho_{\mu^*_\alpha\mu_\delta}\sigma_{\mu^*_\alpha}\sigma_{\mu_\delta} & \sigma^2_{\mu_\delta} & 0 \\ 0 & 0 & 0 & 0 & 0 & \sigma^2_{v_\mathrm{los}} \end{pmatrix}, \tag{16}$$

where $\rho_{\mu^*_\alpha\mu_\delta}$ is the correlation coefficient between the proper motion components, as given in the *Gaia* source table.

Then, with the Jacobian calculated as in Eq. (15), we obtain the covariance matrix in heliocentric Cartesian coordinates (Eqs. (5) and (7)),

$$\Sigma_2 = J\Sigma_1 J^\mathrm{T}. \tag{17}$$

We then again used Eqs. (15) and (17) to successively move first into galactocentric Cartesian (Eqs. (6) and (10)) and, finally, into galactocentric cylindrical coordinates (Eqs. (12) and (13)). At each step, we obtained a full 6×6 covariance matrix that encodes not only the estimated uncertainty in each quantity along its diagonal, but also their correlations. The transformation itself contributes significantly to some of these correlations, for instance, the correlation between the u and v components of the velocity that arises naturally from using the distance in Eq. (7). Nonetheless, the correlation between *Gaia* measurements is also a source of correlations regardless of the coordinate frames. However, the correlations introduced by the coordinate transformations in concert with the distance uncertainties dominate the final correlations between the velocity components, and these are highly direction dependent (see also the following section for further discussion).

Alternatively, we could have chosen to estimate the uncertainties by randomly sampling new mock observables based on the covariance matrix in the initial *Gaia* frame. However, this approach contains some shortcomings: (i) it requires a large number of samples to obtain a robust estimation of the uncertainties, which can be computationally expensive, (ii) we do not know the true error distribution function because the formal errors are estimated from the observables themselves, and (iii) we do not have access to the full posterior distribution function for the distance estimators. While point (i) can be dealt with some patience, points (ii) and (iii) force us to make similar assumptions to those made for the strategy described above, thus limiting the usefulness of this alternative approach.

As a consequence of our decision to use the Jacobians to propagate the uncertainties, we implicitly assumed that the uncertainties of the measured (input) quantities are symmetric. For the proper motions and line-of-sight velocities, this is satisfied, their errors being well described by Gaussian distributions (Gaia Collaboration 2022). However, as described in CBJ2021, the probability distribution functions of the distances are typically skewed, and this is also true of photometric distances, such as those used for the Cepheids. For the CBJ2021 distances, we render the distance uncertainties symmetric by taking the mean of the distances of the provided 16th and 84th percentiles from the median distances, that is, we take as the individual distance uncertainty

$$\sigma_\mathrm{d} = (\texttt{r_hi_photogeo} - \texttt{r_lo_photogeo})/2, \tag{18}$$

where `r_hi_photogeo` and `r_lo_photogeo` are the 84th and 16th percentiles, respectively, of the photogeo distances provided by CBJ2021. Figure 9 shows the variation in the distance uncertainties in our sample with distance for the subset of RGB stars with radial velocities. We note that the median relative uncertainties are smaller than 20%. The distance uncertainties for the OB sample with line-of-sight velocities follows the same trend, but covers a much smaller range of distances.

Using this distance estimator comes at the cost of loosing the correlations between the distances and the proper motions. These correlations are not expected in purely photometric distances, as is the case for the Cepheids, but will be present in as much as the distance is informed by the parallax for the other distance estimates. For the CBJ2021 distances, used for the OB

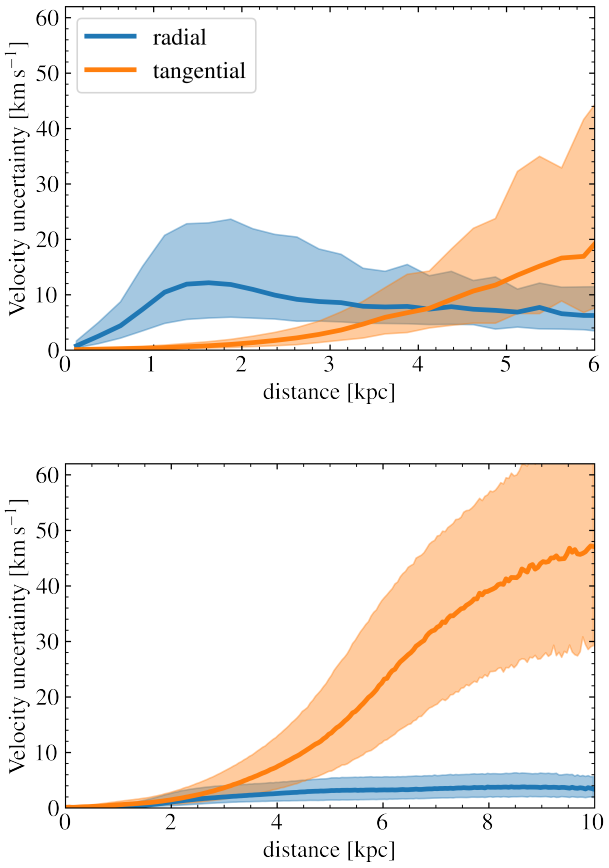


Fig. 10. Median radial (blue) and tangential (orange) velocity uncertainties of the individual sources as a function of distances. The shaded areas show the range between the 16th and 84th percentiles. The upper plot shows the OB stars, and the lower plot shows the RGB stars for the samples with full velocity information.

and RGB samples, the relatively nearby sources, which generally have small relative distance uncertainties, are constrained by the parallaxes, while the more distant sources with larger uncertainties are primarily constrained by the photometry and the CMD prior, so will be only weakly correlated with the proper motions. Therefore, to propagate the uncertainties on the velocities, we considered only the correlations between the proper motion components in the initial covariance matrix (Eq. (16)).

We note that because the tangential (perpendicular to the line-of-sight) velocity components are dependent on both distance and proper motion, their uncertainties are perfectly correlated with the distance uncertainties. As the line-of-sight velocity is not correlated with the astrometry and may be of a different magnitude than the uncertainty in the tangential velocity, the correlations and uncertainties of our velocity components consequently have a strong directional dependence that can potentially introduce false signals or patterns in our maps. Figure 10 shows the median and range of the velocity uncertainties for the OB and RGB samples as a function of distance. We note that the velocity uncertainty of the OB stars with full velocity information, being limited to within a few kiloparsecs of the Sun, is dominated by the uncertainty in the line-of-sight velocities. On the other hand, the uncertainties for the two velocity components of the RGB stars are quite comparable to about 2 kpc, beyond which the tangential component then dominates the uncertainty.

Finally, we also note that our distance uncertainties will again introduce further direction dependencies in the errors and correlations in the final transformation into velocities in galactocentric cylindrical coordinate, via Eqs. (12) and (13). Errors in ϕ can become quite large near the Galactic centre. Moreover, by performing the coordinate transformation to (v_R, v_ϕ) above, we have made ourselves vulnerable to systematic error in our assumed values of $R_\odot$ and $\boldsymbol{v}_\odot$. We explore the effect of these types of uncertainties in the following section.

3.4. Effect of systematic errors

As mentioned above, while the formal errors are quite small, there may be significant systematic errors in our assumed values for $R_\odot$ and $\boldsymbol{v}_\odot$. In addition, as we demonstrate below, even random distance errors can introduce systematic errors in the mean galactocentric velocity components. To investigate the possible effects that these errors can introduce, we constructed a mock catalogue from a rather artificial distribution of stars: We uniformly populated a disc of stars centred on the Sun with a radius of 8 kpc, and added a Gaussian velocity dispersion and an azimuthal velocity with respect to the Galactic centre at $R_{\rm GC}$ that was consistent with what we observe for the RGB sample (see Sect. 5.2), but assumed no mean radial motion (i.e. $v_R = 0$). We also assumed a motion of the observer at the Sun and derived the proper motion and line-of-sight velocities from the relative motions, to which we added fractional uncertainties of 0.01 in the proper motions and 0.1 in the radial velocities. We then rederived the (v_R, v_ϕ) velocity components from the observed (noisy) proper motions, distances, and line-of-sight velocities, and constructed maps of the observed mean velocity field, as described in Sect. 5.

To model the effect of distance uncertainties, we added a 20% Gaussian uncertainty to the true parallax, and then took the inverse of the observed parallax as our distant estimate. We note that this is much larger than the actual uncertainties of our data set, which only reach a relative uncertainty of 20% of the distances at about 10 kpc from the Sun. It is used here simply for the purpose of illustration. However, like the actual distance errors, the probability distribution function of the distance from our inverse-parallax distance estimate is skewed towards larger distances. More importantly, for our rather artificial uniform disc of mock stars, the mean estimated distance will be slightly underestimated systematically for distances less than 8 kpc, but strongly overestimated for distances beyond 8 kpc. These mean biases in the distances of our sample introduce systematic motions in the inferred mean velocity field (V_R, V_ϕ), as shown in the upper two panels of Fig. 11. In the following, we refer to these biases as systematic errors, in the sense that the simulated uncertainties in our experiment systematically induce artefacts in the observed trends, as shown below.

Assuming a more realistic model for our parallax uncertainties of $\sigma_\varpi/\varpi = 0.02\,d_{\rm kpc}$ (i.e. $\sigma_\varpi = 20\,\mu$as), we investigated the effect of assuming erroneous values for $R_\odot$ and the velocity of the Sun with respect to the values that were used to generate the mock observations. We first introduced a systematic error in our assumed value for $R_\odot$, taken to be 200 pc larger than the distance to the Galactic centre used to assign the mean rotational velocities to the mock stars, when we transformed the observed proper motions, distances, and line-of-sight velocities into (v_R, v_ϕ) velocity components. The resulting inferred V_R velocity field is shown in the lower left panel of Fig. 11. Similarly, assuming a correct value for $R_\odot$ consistent with the mock velocities, but assuming an incorrect velocity for the solar v_ϕ component, a similar but inverted pattern in the inferred V_R velocities is observed, with the Sun lying on an axis of

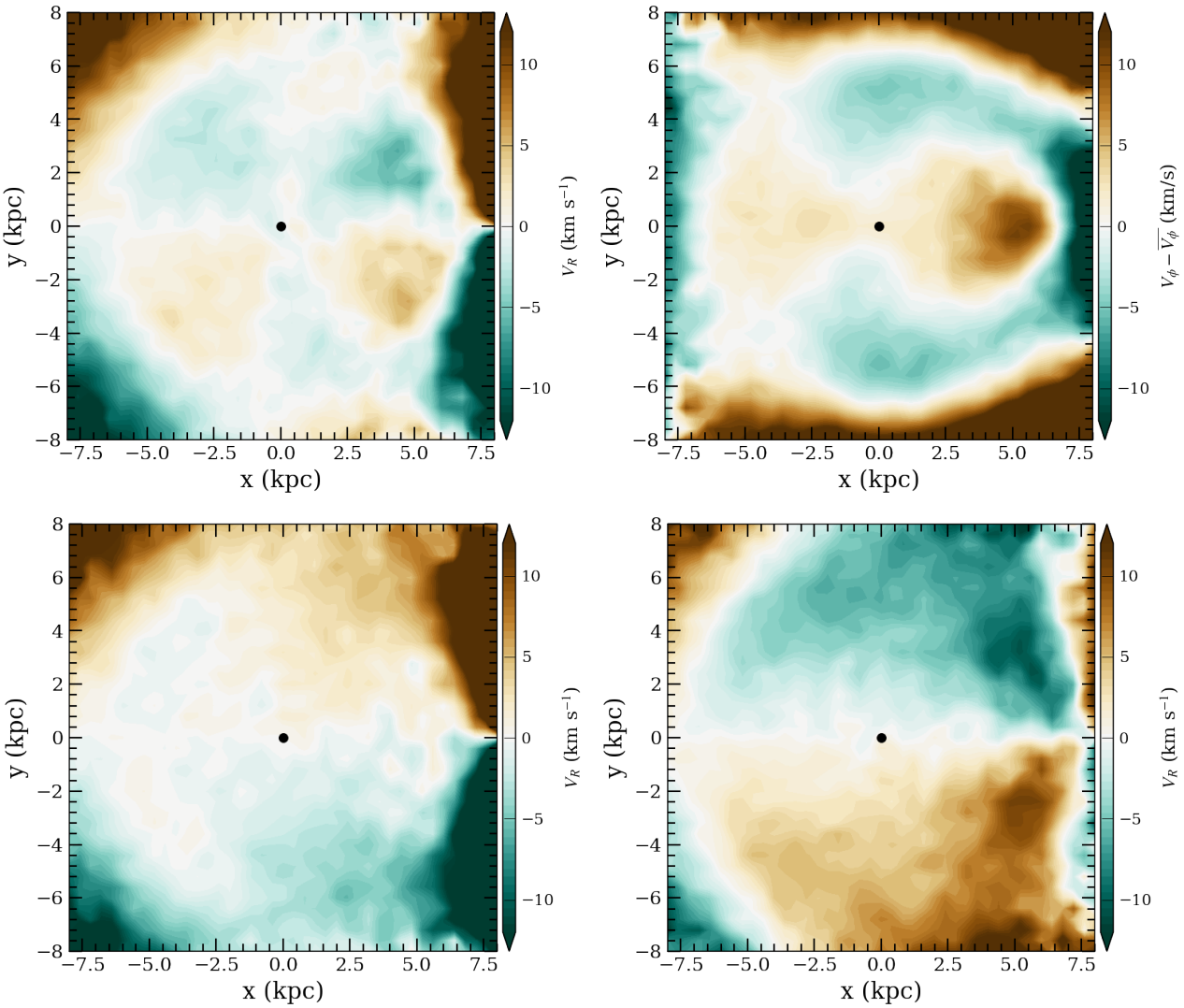


Fig. 11. Systematic velocity trends induced by the simulated uncertainties in our mock catalogue. *Upper left panel*: map of the observed V_R assuming a relative parallax uncertainty = 0.2. *Upper right panel*: same as the left panel, but showing the observed ΔV_ϕ. *Lower left panel*: observed V_R assuming that the true value of $R_\odot$ is 200 pc higher than the adopted value, together with the distance uncertainty model explained in the text. *Lower right panel*: observed V_R assuming that the true value of the solar velocity component $V_{\phi,\odot}$ is 10 km s^{-1} higher than the adopted value, together with the distance uncertainty model explained in the text.

symmetry of the inferred V_R velocity field (lower right panel of Fig. 11).

Another important feature in the velocity maps to be noted is that the velocities beyond the actual distance limit of our mock sample (8 kpc) are very strongly biased. This is an unavoidable feature of any magnitude limited sample, where the real density of the sources sharply decreases beyond some limiting distance. Beyond this distance the sources used to estimate velocities have systematically overestimated distances, and consequently overestimated velocities (in modulus) perpendicular to the line of sight. This limiting distance, beyond which the inferred velocities cannot be trusted, can vary significantly for different lines of sight as a result of the effects of interstellar extinction. In any case, one should resist giving astrophysical significance to features at the edge of velocity maps.

While our assumed systematic errors in the above discussion may be larger than we expect, the purpose of this discussion is to caution anyone interpreting features or patterns seen in velocity maps in galactocentric cylindrical coordinates. As in coordinate space, one should be most suspicious of any patterns in the kinematics that show any symmetry with respect to the Sun's position.

4. Coordinate maps

In this section, we map the spatial distribution of the OB and RGB stars, open clusters, and Cepheid samples described in Sect. 2. Additionally, we present a comparison with some models available in the literature, and discuss the observed similarities and differences.

The left panel of Fig. 12 shows the distribution of the OB stars in the XY-plane of the Galaxy. Far from being homogeneous, the distribution of the OB stars is highly structured, and has numerous regions in which the stellar density is markedly higher than in others. These high-density regions are not randomly distributed, but appear to be organised in spiral arm segments. Specifically, we can identify three quasi-diagonal segments crossing the left panel of Fig. 12: from left to right, we discern the Perseus arm, the Local (Orion) Arm, and an inner stripe corresponding to the Sagittarius-Carina and (possibly) the

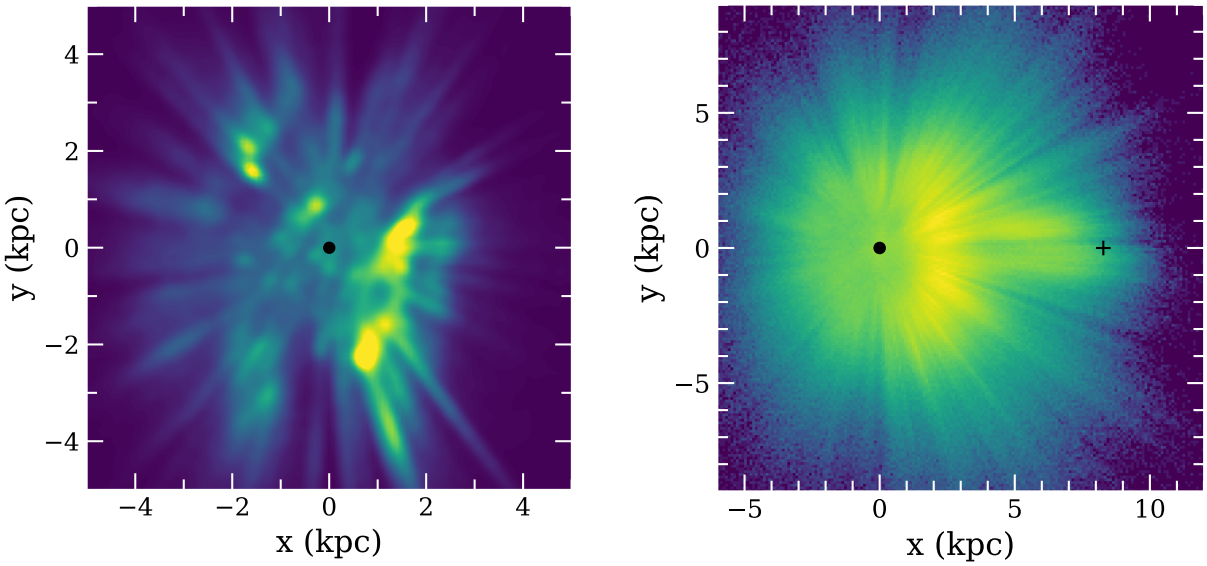


Fig. 12. Spatial distribution in the Galactic plane in heliocentric coordinates of the selected OB stars (*left panel*) and RGB stars with line-of-sight velocities (*right panel*). For the OB stars, we perform a bivariate kernel density estimation using an Epanechnikov kernel with a smoothing length of 200 pc. For the RGB stars, we construct a 2D histogram using cells of 100×100 pc. The Galactic centre is towards the right and is shown with a cross in the right-hand plot. Galactic rotation is clockwise. The position of the Sun is shown with a black dot. A logarithmic stretch is used for the map of the RGB stars to enhance lower-density regions.

Scutum arms. Figure 12 (left panel) maps with unprecedented detail the structural features of the OB stellar population, especially within about 3 kpc from the Sun. Beyond this distance, the distribution becomes increasingly dominated by radial features produced by foreground extinction.

The right panel of Fig. 12 shows the spatial distribution of the 5.7M RGB stars with line-of-sight velocities in the Galactic plane. Again, as for the OB sample, radial "shadow" cones from foreground extinction are clearly visible in the RGB sample, but with higher angular frequencies, as the density here is not derived using a smoothing kernel. In addition to this difference, and in contrast to the OB stars, the RGB sample exhibits a smooth spatial distribution, as expected from a dynamically old stellar population. No clear spiral structure is apparent from the stellar counts, possibly because the giant sample contains typically old stars (compared to the other populations considered in this work). However, we note that a density enhancement is present towards the Galactic centre, presumably due to the Galactic bar. Additionally, we note that an overdense region is apparent at $x \simeq 2{-}3$ kpc, running across a range of y. This is due to the combination of two main factors: (i) we used a magnitude-limited sample, implying that the density decreases with heliocentric distance, and (ii) the intrinsic distribution of RGB stars in the Galactic disc increases towards the inner parts of the Galaxy (as expected from an exponential disc).

To better explore the Galactic spiral structure, we applied the same approach to our OB sample as was adopted by P21 to map the stellar overdensity, defined as

$$\Delta_\Sigma(X, Y) = \frac{\Sigma(X, Y) - \langle\Sigma(X, Y)\rangle}{\langle\Sigma(X, Y)\rangle},$$

where the local surface density $\Sigma(X, Y)$ and the mean surface density $\langle\Sigma(X, Y)\rangle$ were constructed using kernel density estimators with bandwidths of 0.3 and 2 kpc, respectively, adopting an Epanechnikov kernel. The resulting map is shown in Fig. 13. The red diagonal stripes in Fig. 13 correspond to the segments of the nearest spiral arms, consistent with the features identified in the left panel of Fig. 12. Based on Figs. 12 and 13, the emerging picture of the local Galactic spiral structure agrees well with what was found in P21 (see their Figs. 1B and 1C).

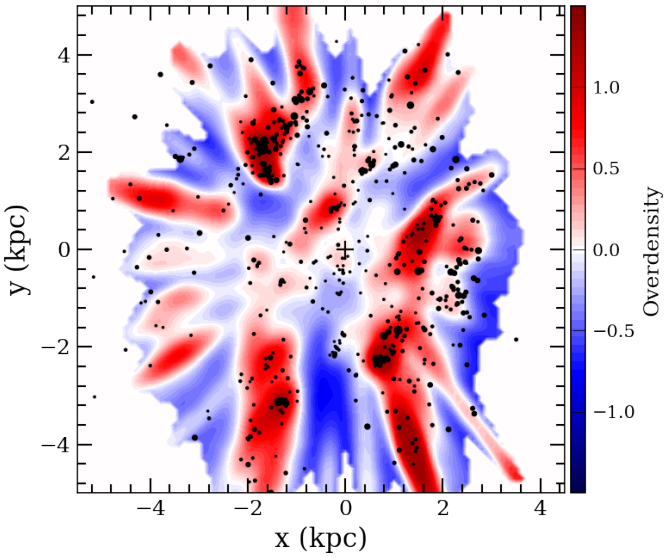


Fig. 13. Overdensity map of the OB stars overplotted with the positions of the open clusters younger than 63 Myr and with $n_0 > 5$, plotted with filled circles whose size is proportional to $\sqrt{n_0}$. The cross indicates the position of the Sun.

The same Fig. 13 shows a comparison between the OB overdensity map and the young (<63 Myr) and bright (i.e. with at least five members brighter than $M_G = 0$) open clusters (OCs). Distances to the OCs were obtained by inverting the median parallax of each cluster, as described above in Sect. 2.1. Figure 13 shows a good agreement between the open clusters distribution and the spiral structure mapped by the OB sample.

Figure 14 shows the spatial distribution of all clusters younger than $\log t = 7.8$ (~63 Myr). Although the young clusters

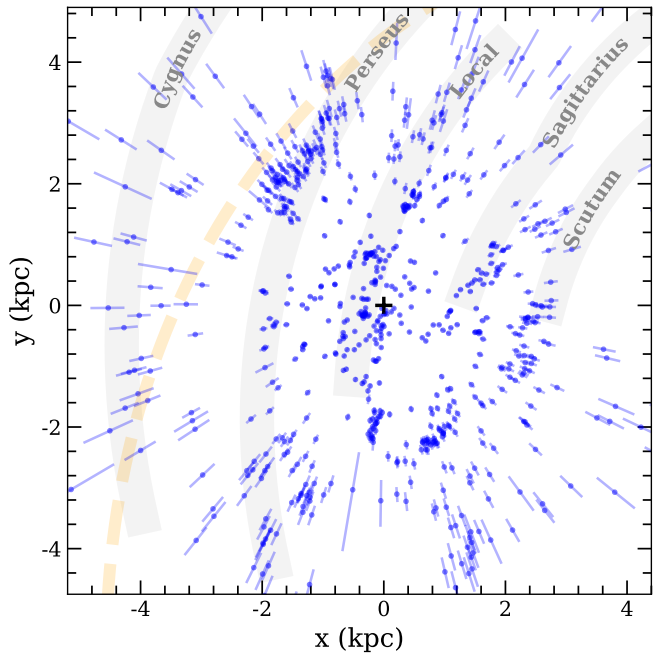


Fig. 14. Heliocentric coordinates of the clusters younger than $\log t = 7.6$ (63 Myr). Thick grey lines are the spiral arm model of Reid et al. (2019), and the dashed line is the trace of the Perseus arm modelled by Levine et al. (2006). The bars represent the 1σ uncertainty on the distance. They take statistical and systematic parallax errors into account.

clearly trace multiple elongated structures, evocative of arms and inter-arm regions, their distribution is not continuous. The young OCs alone do not constitute a sufficient sample to clearly define the main spiral arms. The most striking difference when comparing this distribution to the spiral arm model of Reid et al. (2019; shaded grey arms in Fig. 14) is that the Perseus arm appears interrupted for two kiloparsecs. This discontinuity has been observed before in the cluster distribution (e.g. Cantat-Gaudin et al. 2020) or CO clouds (Peek et al. 2022). On the other hand, the model of Levine et al. (2006) very nicely traces the orientation of the Perseus arm in the upper main-sequence stars (see also P21), and appears to agree reasonably well with the distribution of the OCs as well (see the dashed orange line in Fig. 14). According to this model, the two groups of OCs that Reid et al. (2019) used to define a low-pitch-angle Perseus arm (one in the second and one in the third Galactic quadrant) would in fact belong to two different arms.

Finally, we mapped the spatial distribution of Cepheids younger than 200 Myr using a wavelet transformation (WT). The left panel of Fig. 15 shows a comparison between the single sources (shown as black dots) and the WT coefficients (colored map; see technical details in Ramos et al. 2018, and P21). The right panel of Fig. 15 shows a comparison between the Cepheids WT and some models available in the literature. Solid lines show the four-armed model of Taylor and Cordes (Taylor & Cordes 1993); in the region in which the Cepheids are more abundant ($x < 5$ kpc), the Sagittarius Carina arm appears to agree well below approximately $y \simeq 2.5$ kpc. At approximately $x \simeq 2.5$ kpc and $y \simeq 5$ kpc, the overdensity of Cepheids seems to diverge with respect to the Taylor and Cordes model of the Sag-Car arm in this direction. In the outer regions of the Galaxy, the orientation of the Perseus arm in the Cepheids seems more consistent with the Levine model (Levine et al. 2006) than with either the Taylor and Cordes or Reid models. This outer arm, based on HI data, is remarkably traced by the Cepheids out to a galactocentric radius of at least 16 kpc. Unfortunately, the Cepheids are too sparse to trace the weaker Local (Orion) Arm.

5. Velocity maps

This section studies the kinematics of RGB and OB stars in the disc of the Milky Way to highlight the effects of the disc asymmetries on velocities. We used the selections of OB and RGB stars within $|z| \leq 0.3$ (77 659 stars) and $|z| \leq 1$ kpc (5 730 578 stars) of the Galactic plane, respectively. We first describe the construction of the maps of the mean velocity and velocity dispersion from the individual velocities derived in Sect. 3, and analyse the resulting velocity fields of the RGB sample, which cover a much larger extent of the disc than the OB sample discussed at the end of this section. Table 4 summarises our notation and is provided for convenience.

5.1. Construction and analysis of velocity maps

We built maps of the ordered and random motions for the radial, azimuthal, and vertical velocity components. We designed these maps with a constant 100 pc resolution, with 341×341 pixels. These characteristics result from empirical choices to have sufficient numbers of stars per bin for the current analysis. To perform robust derivations of the velocity per pixel, we considered only the cells with at least 20 stars, and masked all others. This resulted in grids with a median number and maximum number of 58 and 267 stars per pixels for OB stars, respectively, and 152 and 2541 stars per pixel for RGB stars, respectively.

At a given heliocentric position, (x, y) corresponds to a cell j of 100×100 pc in our three velocity components $k = R, \phi, z$ maps, which contains N_* stars. We estimated the stellar mean velocity V_k and its associated dispersion σ_k^* by optimising the log-likelihood of the distribution of observed velocities $v_{k,j}$ (with uncertainties $\sigma_{vk,j}$) of the stars located within the j-cell. We assumed Gaussian uncertainties on the individual independent $v_{k,j}$, so that the negative log-likelihood to minimise is

$$\mathcal{L}(V_k, \sigma_k^*) = \frac{1}{2} \sum_j^{N_*} \left(\ln(\sigma_k^{*2} + \sigma_{v_{k,j}}^2) + \frac{(v_{k,j} - V_k)^2}{\sigma_k^{*2} + \sigma_{v_{k,j}}^2} \right). \quad (19)$$

Appendix B.1 details the derivations of the uncertainty $\sigma_{V k,j}$ of our mean velocities $V_{k,j}$, which also demonstrates that under certain conditions, we can approximate them as $\sigma_{V_k} = \sigma_k^* / \sqrt{N_*}$. (Most inconveniently, σ is the traditional notation for velocity dispersion, but also that for Gaussian uncertainties. To avoid potential confusion, we add a superscript $*$ to the stellar velocity dispersion).

Figure 16 shows the resulting three-component velocity fields for the sample of RGB stars (left panels) and the velocity dispersions (right panels). We optimised the displayed velocity ranges to help visually identify regions where streaming motions occur. The left panels of Fig. B.1 show the associated uncertainty maps for the velocities.

The V_R map shows a remarkable bisymmetric feature on either side of the GC, with negative and positive values on each side of the apparent major axis of the bar. This quadrupole feature is a characteristic of the mean inward motion down to ~ -40 km s^{-1} ($y > 0$) and the mean outward motion up to ~ 45 km s^{-1} generated by the Galactic bar. *Gaia* DR3 allows us to confirm the bar quadrupole V_R pattern identified in Bovy et al. (2019) and Queiroz et al. (2021), who used thousands of stars, but using *Gaia*

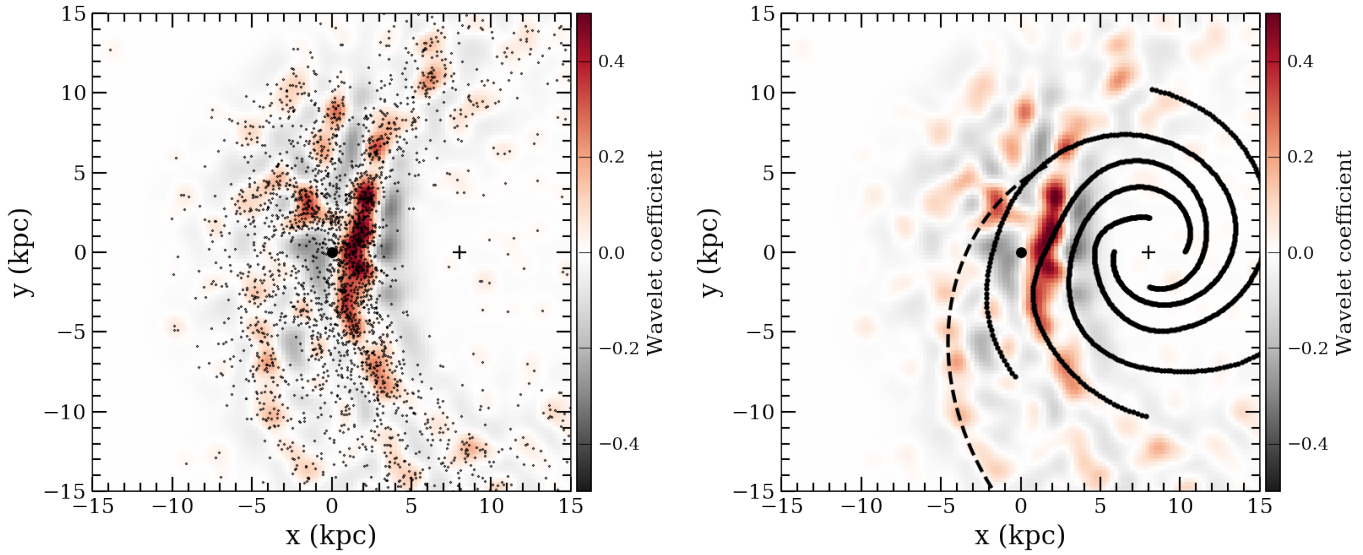


Fig. 15. Wavelet transformation of the Cepheids with age <200 Myr. Black dots in the *left panel* show the positions of the single sources, and the *right panel* shows on a larger scale an overlay of the model from Taylor & Cordes (1993, solid lines) and the model from Levine et al. (2006, dashed line).

Table 4. Notation and nomenclature.

Variables	
$\varpi, \boldsymbol{\mu}$	Astrometry
$\sigma_\varpi, \sigma_{\mu_\alpha}, \sigma_{\mu_\delta}$,	Their uncertainties
$v_{\rm los}$	Line-of-sight (los) velocities
$d, \sigma_{\rm d}$	Distance and related uncertainty
x, y, z	Heliocentric Cartesian coordinates
X, Y, Z	Galactocentric Cartesian coordinates
u, v, w	x, y, z velocity components
R, ϕ, z	LH galactocentric cylindrical coordinates
v_R, v_ϕ, v_z	R, ϕ, z velocity components
$\sigma_{v_R}, \sigma_{v_\phi}, \sigma_{v_z}$	Their uncertainties
V_R, V_ϕ, V_z	Mean v_R, v_ϕ, v_z velocities
$\sigma_{V_R}, \sigma_{V_\phi}, \sigma_{V_z}$	Their uncertainties
V_R	Radial velocity
V_ϕ	Azimuthal velocity
$\overline{V}_\phi(R)$	Mean azimuthal velocity at R
$\sigma^*_R, \sigma^*_\phi, \sigma^*_z$	Velocity dispersions in R, ϕ, z directions

DR2 and EDR3 astrometry (Gaia Collaboration 2018b, 2021c) together with APOGEE line-of-sight velocities (Majewski et al. 2017; Abolfathi et al. 2018). Section 5.3 and Appendix C describe this quadrupole pattern in detail. We also note that the RGB sample contains enough stars to apparently provide us with mean velocity estimates beyond the Galactic centre (GC), but they should be interpreted with caution.

The σ^*_R map shows a bisymmetric pattern as well, but different from V_R, with larger amplitudes that are aligned with the direction in which V_R changes its sign along the major axis of the bar, and lower along a perpendicular direction. Here again, the GC is the node of the quadrupole feature. In addition to the central quadrupole, streaming motions in V_R also occur at larger radii, for example $R = 6.5$ kpc ($x \sim 1.5$ kpc), which shows that V_R is larger for $|y| < 2$ kpc than at smaller and larger azimuths. At $R \sim 10$ kpc ($x, y \sim -1.5, +1$ kpc), V_R shows a clear change of sign with respect to azimuth.

The distribution of the azimuthal velocity V_ϕ is elongated in the bar: Within the central 5 kpc, the rotation at a given radius is slower along the apparent bar axis than perpendicular to the bar axis. The σ^*_ϕ map also seems to exhibit a bisymmetry in the bar region, but rotated by about 45° with respect to that seen in σ^*_R. The azimuthal random motion appears smaller when the radial random component is larger. In other words, the planar velocity dispersion is highly anisotropic in the bar region.

The vertical velocity V_z is mostly positive. Unlike the other two velocity components, it does not show any pattern linked to the presence of the Galactic bar. A streaming is observed around $R = 7$ kpc, as V_z shows among the lowest values on one side ($1 \leq x \leq 4, y < -2$ kpc), while being positive on the opposite side with respect to $y = 0$. However, this pattern, being symmetric about the x-axis, may be an artefact of systematic errors. Vertical motions are also larger with galactocentric radius towards the Galactic anticentre, clearly showing the kinematic signature of the warp of the Galactic disc beyond, in agreement with previous results (Gaia Collaboration 2018a; Romero-Gómez et al. 2019; Poggio et al. 2018, 2020; López-Corredoira & Sylos Labini 2019). We do not observe any bisymmetric feature in the vertical dispersion, which is larger along $l \sim 0$. The vertical velocity component is more sensitive to systematic errors because our sources are near the galactic ($b = 0$) plane, therefore this component is predominantly seen in the tangential velocities that are sensitive to distance errors (see Fig. 10).

In summary, these maps detect the significant signature of the Galactic bar of the Milky Way in the inner disc. We also find some streaming signatures of V_R at larger galactocentric distances, which might be associated with corotation or the outer Lindblad resonance. Section 5.4 discusses the case of the young stellar populations and the similar maps for the OB star sample.

5.2. Analysis of radial profiles

From these maps, we inferred the average axisymmetric variation of velocities following the same procedure as in Gaia Collaboration (2021d), where for each bin in radius of 200 pc size, the median value of the cells in the radial bin define

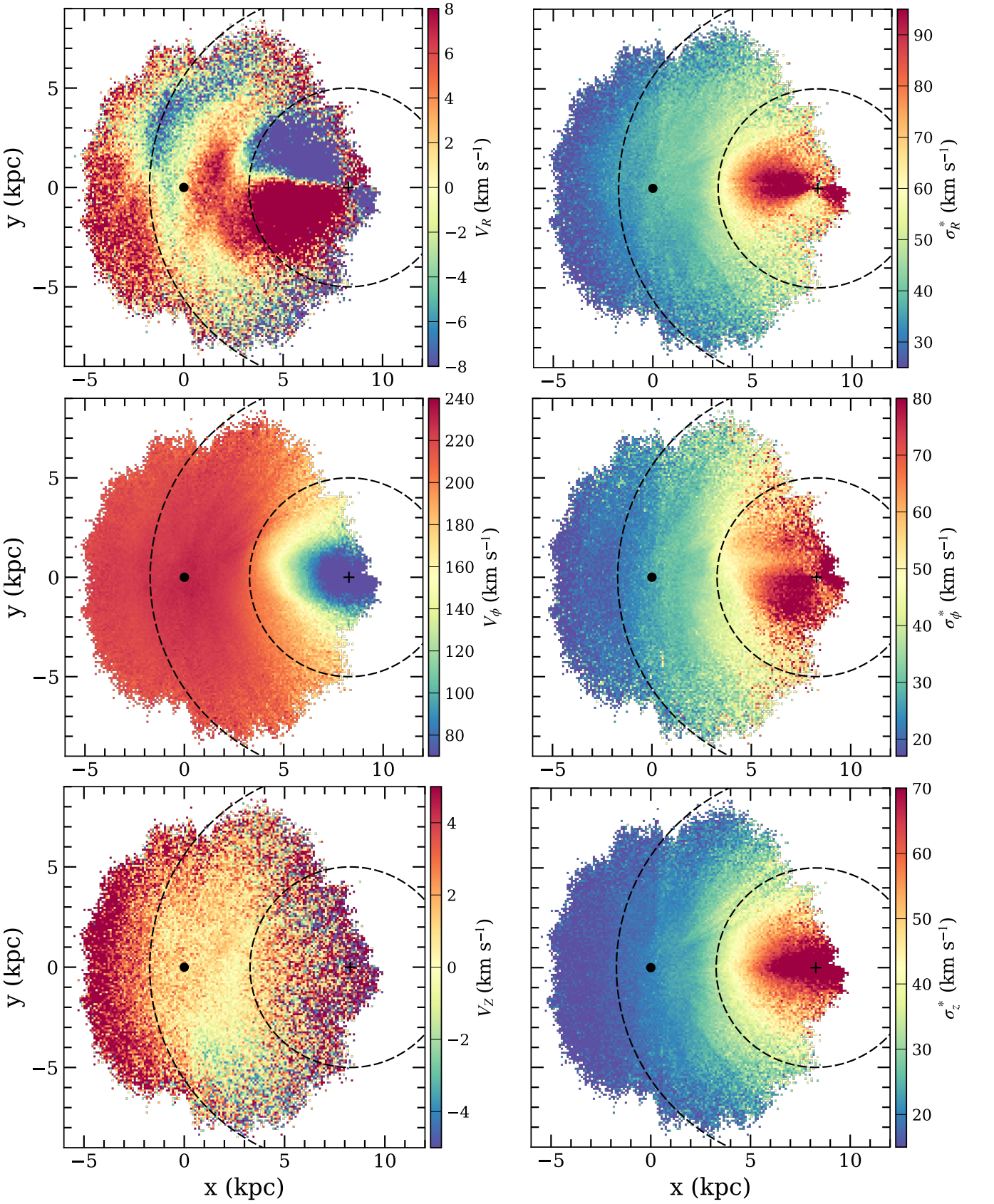


Fig. 16. Velocity maps of RGB stars. *Left* and *right panels*: ordered and random motions, respectively. *From top to bottom panels*: radial, azimuthal, and vertical velocity components. The origin, emphasised by the black dot, indicates the position of the Sun, and a plus symbol indicates the Galactic centre. Dashed circles represent the constant distance to the Galactic centre at $R = 5$ and $R = 10$ kpc. The velocity ranges have been chosen to enhance contrasts to help visually identify regions in which streaming motions occur. The left panels of Fig. B.1 show the associated uncertainty maps. We detail the construction of these maps in Sect. 5.1. These velocity and velocity dispersion maps can be found at the CDS in FITS format.

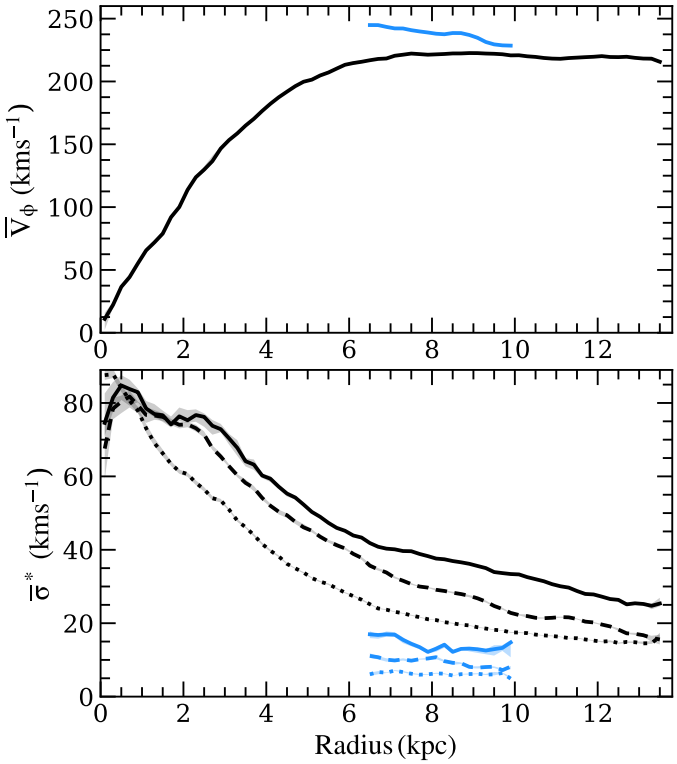


Fig. 17. Velocity profiles of the Milky Way RGB and OB stars (black and blue lines, respectively). *Top panel*: rotation curves. The shaded area represents the uncertainties. *Bottom panel*: radial, azimuthal, and vertical velocity dispersions (solid, dashed, and dotted lines, respectively). The data shown in these figures can be found at the CDS.

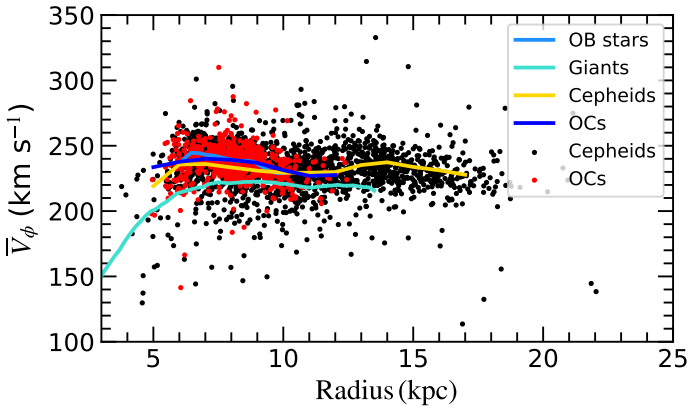


Fig. 18. Comparison of rotation curves of the different samples. We show the mean azimuthal velocity for the open clusters (dark blue) and Cepheids (yellow) as a function of galactocentric radius (calculated as explained in the text), compared to the profiles of the OB (light blue) and RGB stars (turquoise). Coloured points show the single sources for the Cepheids (black dots) and OCs (red points).

the azimuthally-averaged velocity $\overline{V}_\phi(R)$ at that radius. We discarded radial bins with fewer than five pixels from the maps. Bootstrap resamplings were performed at each radius to define the velocity uncertainties, measured at the 16th and 84th percentiles of the velocity distributions. In Fig. 17 we present the Galactic rotation curves, as well as the velocity dispersion profiles for the RGB and OB samples. Despite the asymmetries observed in the velocity field, especially at radii $R < 5$ kpc, the rotation curve of the RGB stars is regular. It smoothly increases like a solid body up to $\overline{V}_\phi \sim 220\,\mathrm{km\,s^{-1}}$ to $R \sim 6$ kpc and then remains constant out to the last measured radius. The amplitude of the curve for the younger OB stars is larger than for RGB giants because their asymmetric drift is smaller, and it decreases with galactocentric radius. It rotates $17\,\mathrm{km\,s^{-1}}$ faster on average than the RGB stars over the radial range $R = 6.5{-}10$ kpc. These average rotation curves were subtracted from the V_ϕ maps to produce residual velocity fields $V_\phi(x,y){-}\overline{V}_\phi(R)$. These are useful to show velocity streaming in the outer disc (Sect. 5.4).

Figure 18 shows a comparison between the azimuthal velocity of the OB stars, the open clusters, the Cepheids, and the RGB giants with respect to galactocentric radii. The median velocities for Cepheids and open clusters were calculated using overlapping radial bins of 1 kpc step and 2 kpc width. As expected, the agreement between the OB stars and the OCs is good. The Cepheids exhibit a mean azimuthal velocity similar to but slightly slower than the OB and the open clusters, but reach significantly larger radii. Finally, the mean azimuthal velocity for the RGB giants is systematically lower than the other tracers, as expected for an asymmetric drift for an older population with a higher velocity dispersion.

The radial and azimuthal velocity dispersion profiles of RGB stars show two distinct regions. Within the inner part of the bar ($R \sim 2.5$ kpc), the profiles are shallow and the dispersions comparable ($\sim$75–80 km s^{-1}), but we note that the (x,y) map of the dispersion (Fig. 16) in this region shows very strong asymmetries. Beyond 2.5 kpc, $\overline{\sigma}^*_z < \overline{\sigma}^*_\phi < \overline{\sigma}^*_R$ and the profiles continuously decrease for all three components. The radial profiles of the velocity dispersion $\overline{\sigma}^*_k$ of the OB stars do not vary strongly with radius, showing average radial, azimuthal, and vertical dispersions of 14.2, 9.4, and 6.2 km s^{-1}, respectively. This agrees very well with the observed random motions of gas within $R = 8$ kpc (4–9 km s^{-1}; Marasco et al. 2017). The axis ratios of the velocity ellipsoid as averaged from these profiles for $R > 3$ kpc are $(\overline{\sigma}^*_\phi/\overline{\sigma}^*_R, \overline{\sigma}^*_z/\overline{\sigma}^*_R, \overline{\sigma}^*_z/\overline{\sigma}^*_\phi) = (0.81, 0.60, 0.75)$ for the RGB stars and $(0.66, 0.44, 0.66)$ for OB stars.

5.3. Kinematics of the bar

In this section, we estimate some fundamental parameters of the Galactic bar, guided by the results obtained from Sect. 5.1 and with the help of a mock galaxy from a numerical test-particle simulation of a barred galaxy. We wish to clarify that this is not a made-to-measure, customised simulation that intends to reproduce the observed data set of RGB stars quantitatively. The simulation has to be considered as a simple diagnostic tool for a qualitative comparison to the observations, and the results presented below are tentative possibilities. We refer to Appendix C for the description and analysis of the simulation. We thus applied the same recipes as described below to the simulations in Appendix C to determine by analogy the orientation and pattern speed of the Galactic bar, as well as the location of the outer Lindblad resonance.

We performed a fit to the non-uniformity of the kinematics in the bar region of the RGB sample, assuming that the Galactic bar perturbs velocities by adding a bisymmetric component to the axisymmetric motions. This should apply to most of the ordered and random motions because all of them but v_z were shown to be similarly structured in the bar region (Sect. 5.1). We therefore performed a simple Fourier decomposition up to second order to characterise the axisymmetric and the bisymmetric components in the maps. This approximation of V_R and V_ϕ is referred to as

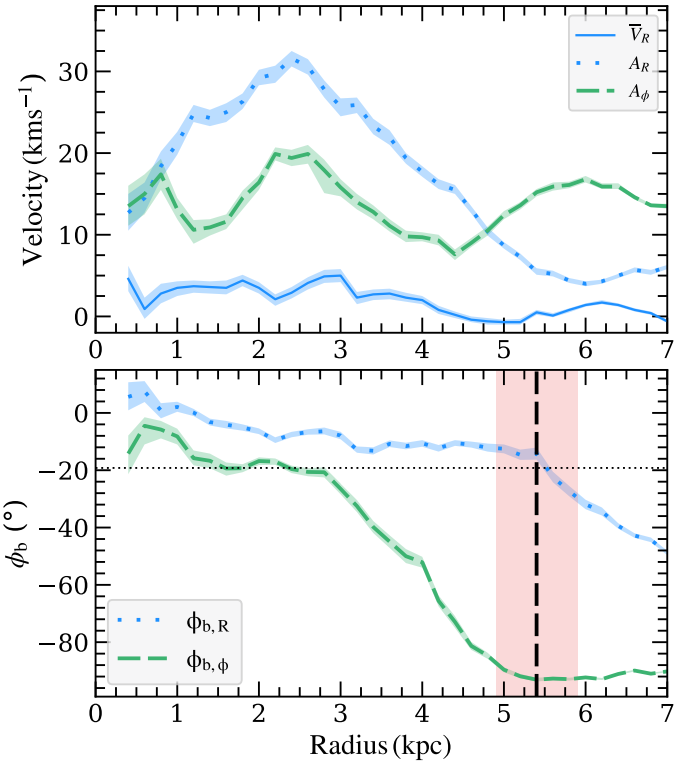


Fig. 19. Results of the bisymmetric model of the V_R and V_ϕ velocity maps. *Top*: amplitudes A_R and A_ϕ of the bisymmetry. The axisymmetric component $\overline{V}_R$ is also shown. *Bottom*: phase angle of the perturbation with respect to the Sun-GC direction. The shaded area represents the uncertainties. The horizontal dotted line marks the estimated bar orientation angle. The vertical dashed line and purple area show the estimated location of the bar corotation.

$V_{R,\mathrm{mod}}$ and $V_{\phi,\mathrm{mod}}$, and is given by

$$V_{R,\mathrm{mod}}(R,\phi) = \overline{V}_R(R) + A_R(R)\cos\left(2(\phi - \phi_R(R))\right), \tag{20}$$

where $\overline{V}_R(R)$ is the axisymmetric mean value, and A_R and ϕ_R are the amplitude and phase angle of the bisymmetric Fourier harmonics of V_R, respectively. Another parameter of interest is the scatter in the modelling, $V_{R,s}$, which absorbs all other asymmetric departures from the bisymmetry in the velocity fields. We use an analogous expression for $V_{\phi,\mathrm{mod}}$.

We performed Bayesian inferences of the model through Markov chain Monte Carlo (MCMC) fits, using the Python library EMCEE (Foreman-Mackey et al. 2013). As this model applies best to regions in which the kinematics is well described by a second-order perturbation, we restricted the analysis to $0 \leq R \leq 7$ kpc and considered a radial bin width of 200 pc. Defining the residual velocity as $V_{R,\mathrm{res}} = V_R - V_{R,\mathrm{mod}}$, the conditional likelihood function for each radial bin is expressed as

$$\mathcal{L}(\overline{V}_R, A_R, \phi_R, V_{R,s}) = -\frac{1}{2}\left(n_{\mathrm{pix}}\ln(2\pi) + \sum^{n_{\mathrm{pix}}}\left(V^2_{R,\mathrm{res}}/\xi^2 + \ln(\xi^2)\right)\right), \tag{21}$$

and similarly for ϕ component, where $\xi^2 = \sigma^2_{V_R} + V^2_{R,s}$, and n_{pix} is the number of pixels inside the corresponding radial bin, requiring $n_{\mathrm{pix}} > 25$. Radial bins that did not satisfy this condition were not considered. We set a number of 32 walkers and 2000 steps in the MCMC fits, which is enough to converge towards robust and stable solutions. The prior distributions were uniform and spanned $[-50, 50]$ km s^{-1} for $\overline{V}_R$, $[0, 300]$ km s^{-1} for $\overline{V}_\phi$, $[0, 50]$ km s^{-1} for A_R, $[0, 30]$ km s^{-1} for $V_{R,s}$, and $[-80, 110]°$ for ϕ_R. Following prescriptions from Appendix C, ϕ_R and ϕ_ϕ were linked to the direction of the bisymmetric perturbation of density with respect to the Sun-GC direction in the bar region, which we call ϕ_b, by $\phi_{\mathrm{b},R} = \phi_R - \pi/4$ in the case of the V_R model, and $\phi_{\mathrm{b},\phi} = \phi_\phi - \pi/2$ in the case of V_ϕ. We quote the uncertainties on the parameters at the 16th and 84th percentiles of the posterior distributions.

Figure 19 shows the resulting fits. The bisymmetry is strongest at $R = 2.5$ kpc in both the azimuthal and radial velocity fields. While the amplitude of the perturbation decreases beyond 2.5 kpc for A_R, it admits other maxima at $R \sim 0.8$ and 6 kpc for A_ϕ. As expected, this simple model shows that V_R is anything but axisymmetric, as A_R exceeds $\overline{V}_R$. The axisymmetric radial velocity is mostly positive, showing a bulk outward motion of 3.6 km s^{-1} for $R < 3$ kpc, and null beyond 3 kpc on average. As the radial velocity should be null on average, for a disc that is nearly relaxed, we attribute this non-negligible $\overline{V}_R$ to the incomplete coverage of azimuthal angles. In other words, this bulk motion is only representative of the observed portion of the Galactic disc. Another feature of interest is the low-velocity scatter parameters $V_{R,s}$ and $V_{\phi,s}$, which is $\sim$6 km s^{-1} at small radius and decreases to <1 km s^{-1} out to $R = 7$ kpc (not shown in Fig. 19). As for $\overline{V}_\phi$, we find that it is very similar to the median rotation curve derived in the previous section.

The orientation of the bisymmetry with respect to the Sun-GC direction is found to be different in the V_R and V_ϕ models, particularly beyond $R = 3$ kpc, as shown in the bottom panel of Fig. 19. At the peak of the strength at $R = 2.5$ kpc, ϕ_b differs by $\sim$12°. Interestingly, ϕ_b in the V_ϕ model remarkably shows the same trend as that seen in the numerical simulation (Fig. C.2), where it faithfully traces the true bar orientation even in the presence of uncertainties. As shown in Fig. C.3, the ϕ_b in the V_R model is more affected by the uncertainties. We can thus infer that the bar angle with respect to the Sun-GC direction is very close to the value for which $\phi_{\mathrm{b},\phi}$ remains flat before the abrupt drop, that is, $-19.2° \pm 1.5°$ for $1.5 < R \leq 2.8$ kpc.

Then, as the location of the minimum of ϕ_b of the V_ϕ model beyond the drop of phase and before it rises at larger radii corresponds to the corotation of the Galactic bar in the simulation (see right panel of Fig. C.2), we find by analogy that the range $R = 5.2$–6 kpc hosts the corotation radius of the Galactic bar, R_CR. We adopted a conservative value $R_\mathrm{CR} = 5.4 \pm 0.5$ kpc. This is surprisingly also the location at which ϕ_b starts to decrease for V_R. This coincidence was not seen in the numerical simulation, maybe because of the lack of spiral structure beyond the bar in the mock data.

In Fig. 20 we show the angular velocity curve, $\Omega = \overline{V}_\phi/R$, and its combination with the epicyclic frequency for the RGB stars (black) and OB stars (blue, only the angular velocity). We emphasise here that the epicyclic frequency was derived by assuming the epicycle approximation, which might not be perfectly correct in a radial range far from the solar neighbourhood. When we assume the corotation radius range obtained above from the phase of the bisymmetry in v, the intersection between R_CR and the Ω curve provides the bar pattern speed, which is $\Omega_\mathrm{bar} = 38.1^{+2.6}_{-2}$ km s^{-1} kpc^{-1}. We can also provide an estimation of the outer Lindblad resonance (OLR), which is the galactocentric radius at which the fixed pattern speed intersects the curve $\Omega + \kappa/2$, that is, the position in the disc at which stars rotate slower than the bar pattern and perform two radial

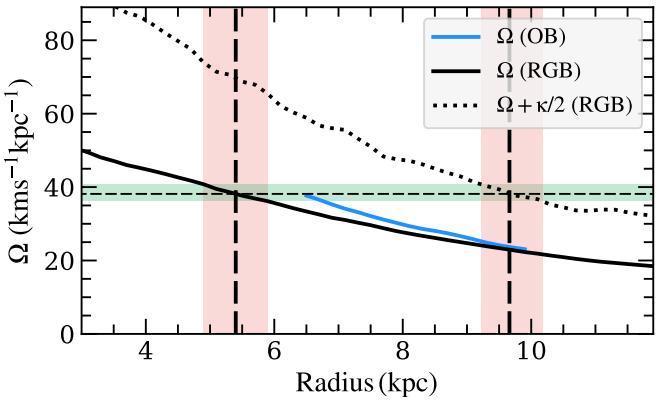


Fig. 20. Lindblad resonances of the Galactic bar. The solid (dotted) black line shows the angular frequency (angular frequency plus half of the epicyclic frequency) for the RGB stars, and the solid blue line shows the angular frequency for the OB stars. The horizontal dashed line represents the bar pattern speed, and the two vertical dashed lines at $R = 5.4$ and 9.7 kpc, with their uncertainty range in purple, are the location ranges of the corotation and outer Lindblad resonance, respectively.

oscillations for one revolution of the bar pattern, κ being the epicyclic frequency. In this case, the RGB sample provides an OLR of 9.7 ± 0.5 kpc, which is outside the solar radius. A word of caution: we estimate $\Omega_{\rm bar}$ and the OLR from the azimuthal angular velocity of the RGB sample, which is not the same as that from the circular velocity due to asymmetric drift. We note that the angular velocity of OB stars, which are younger and less affected by asymmetric drift, is slightly higher than that of RGB stars. By extrapolation to the inner disc, our $\Omega_{\rm bar}$ value could thus be biased towards lower values and should be taken as a lower limit.

5.4. Kinematics of the outer disc

In this section, we present and discuss the velocity maps for the OB and RGB sample in the outer disc (i.e. with galactocentric radius $R > 5$ kpc). We also compare them to the spatial location of the spiral arms in the Galaxy.

Figure 21 shows the velocity maps of the OB stars, with the V_R, V_ϕ, V_Z maps in the left panels. In the right panels we show the same maps (with the exception of the middle panel, where V_ϕ has been replaced by the residual map of V_ϕ, calculated as explained in Sect. 5.1), but compared to the spiral arms found in the overdensity (see Sect. 4), overlaid as grey shaded contours. We note that for the OB stars, the overdensity in the spiral arms and the streaming motions can be studied using the same stellar population (although the two samples are not exactly the same because only the OB stars with line-of-sight velocities were used to derive the velocity maps). This gives us confidence that the maps are self-consistent, and that the comparison between the spatial spiral arms and the corresponding streaming motions is appropriate.

The top right panel of Fig. 21 shows an alternating positive-negative pattern in V_R, the orientation of which is not aligned with the spiral arms in density. A prominent feature of stars with positive V_R is apparent at approximately $x \approx 0$ kpc, crossing the map almost vertically and connecting the upper edge of the Local Arm with the lower side of the Sag-Car arm. The middle right panel of Fig. 21 shows the residual of V_ϕ with respect to the mean $\overline{V}_\phi(R)$. Based on this map, the stars located just outside and inside the Local Arm move systematically more slowly than the mean $\overline{V_\phi}$ (yellow-green regions), while stars lying on the Local Arm appear to move systematically faster than $\overline{V_\phi}$ (red region). However, the alignment of these azimuthal streaming motions with the density contours is not perfect in the lower part of the map. On the other hand, a striking alignment between the local arm and a systematically positive vertical velocities V_z is shown in the bottom right panel of Fig. 21, indicating that the OB stars exhibit both in-plane streaming motions and vertical bending waves, all with a relatively short radial wavelength.

In contrast with the OB sample, the RGB sample is an older, dynamically relaxed stellar population extending much farther from the Sun. This allows us to trace the outer disc kinematics over a much larger extent than the OB stars. In order to better highlight the observed features in the outer disc, we masked out the region $R < 5$ kpc and show the V_R map and the V_ϕ residuals in Fig. 22. To compare the velocity maps of the RGB stars to the spatial position of the spiral arms in the NIR, we compared them with the two-arm model from Drimmel (2000), shown as solid lines, while the $\pi/2$ phase-shifted geometry, corresponding to the minimum inter-arm density, is shown as a dashed curve. While no clear spiral structure is evident in the RGB spatial distribution (see Sect. 3.1), the large-scale streaming motions in the radial velocities suggest some possible correspondence, especially along the inter-arm dashed curve.

Moreover, the V_R map (left panel) shows a large positive V_R feature in the third quadrant (between $180° < l < 270°$) that becomes positive at about $l = 170°$ between about $R = 9$ and 11 kpc. This feature is approximately aligned with an analogous change in the radial velocities in the inner bar region (see also the top left panel of Fig. 16), and is similar to a feature seen in simulations with a bar near the outer Lindblad resonance. In contrast to the V_R map, the V_ϕ residuals in the right panel of Fig. 22 do not show any clear non-axisymmetric features in the outer disc. There is a noticeable gradient in the V_ϕ residuals, however, at about $y = 0$, where the residuals are systematically lower for higher values of $|y|$. Because it is symmetric about the x-axis, this is likely a systematic in the velocity map caused by distance uncertainties, as noted in Sect. 3.4 (Fig. 11). We also recall that features near the edge of these maps may well be artefacts from oversampling sources with overestimated distances, as also discussed in Sect. 3.4.

In addition to exploring non-axisymmetry in the disc, with the increase in spatio-kinematic coverage, we can also explore the asymmetry about the plane of the Galaxy. In Fig. 23 we present velocity difference maps between the $z > 0$ and $z < 0$ hemispheres for the RGB sample (top panels) and OB stars (bottom panels). In each of the components ($k = R, \phi, Z$) we created velocity maps for the upper and the lower hemispheres and then took their difference (i.e. $\Delta V_k = V_{k,Z>0} - V_{k,Z<0}$). As with the other velocity maps, we also overplot the two-arm spiral model (black) based on NIR data from Drimmel (2000). Additionally, we plot the Perseus (red), Sag-Car (purple), and the Local (cyan) Arms from Reid et al. (2019). For the RGB stars, Fig. 23a shows that in ΔV_ϕ, within a heliocentric radius of about 3 kpc, there is no significant difference between the upper and the lower disc, while beyond $R > 11$ kpc, the disc rotates faster below the disc plane ($z < 0$) by up to 10 km s^{-1} in the third quadrant and in the anticentre direction. A similar feature is seen in the ΔV_R map, but in the opposite sense, with more positive radial motion above the disc plane. By comparing this with Fig. 22 (left panel), we see that this feature corresponds with the positive V_R feature in the

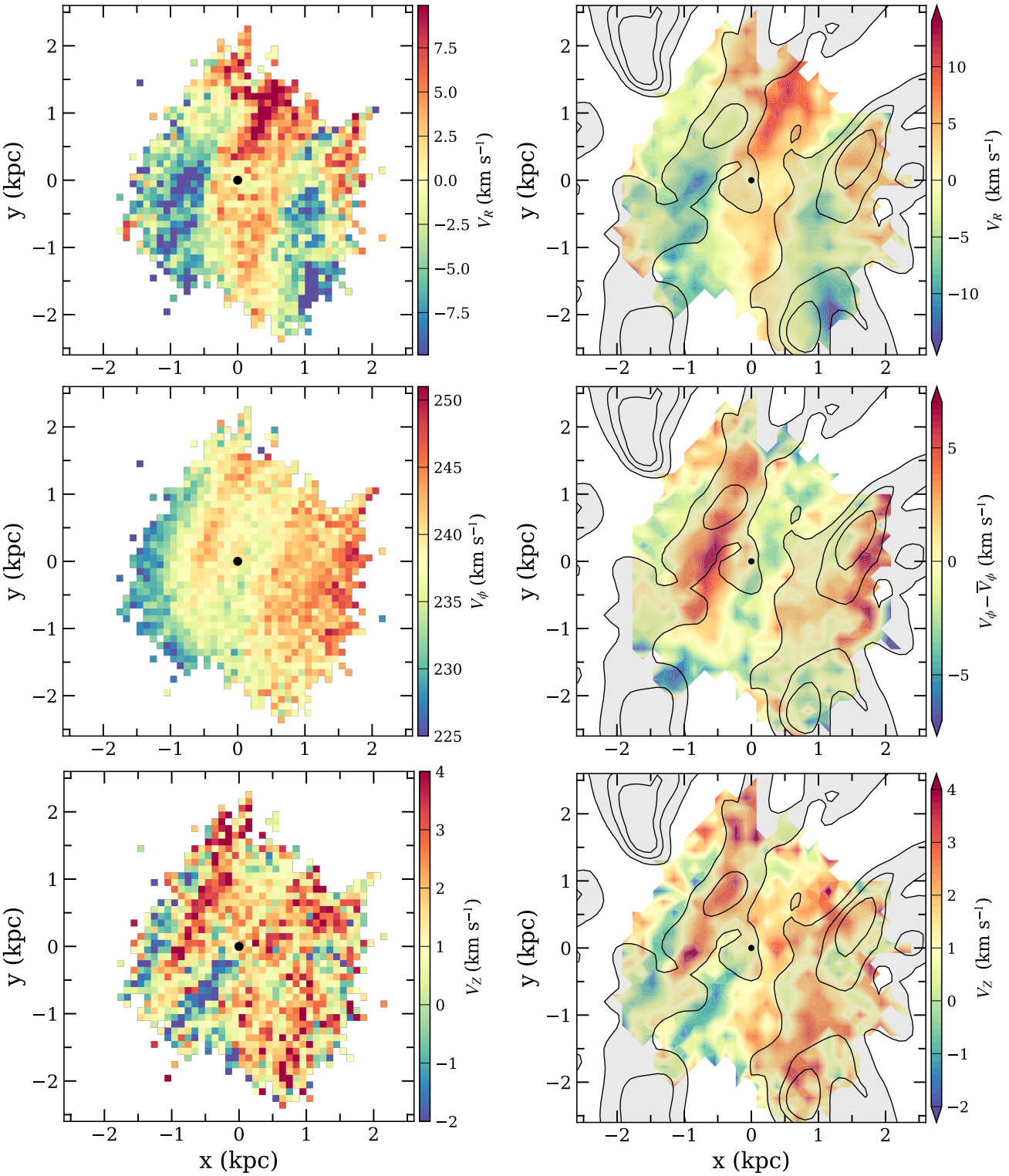


Fig. 21. Velocity maps of OB stars. *Left panels*: inferred radial, azimuthal, and vertical velocity from top to bottom. The velocity ranges have been chosen to enhance contrasts. *Right panels*: maps of the radial velocity (*top panel*), the azimuthal residual velocity (*middle panel*), and the vertical velocity (*bottom panel*), compared to the overdensity contours of the OB stars (grey shaded areas), calculated as explained in Sect. 3.1. In all panels, the position of the Sun is marked by a filled circle. The maps were obtained considering only stars within $|z| \leq 0.3$ kpc. The velocity and maps (left-hand column) can be found at the CDS in FITS format.

third quadrant already noted above. Clearly, the positive V_R in this part of the outer disc is almost entirely located above the disc plane. It is interesting to note that about the plane of the Galaxy, $\Delta V_R \sim 0\,\mathrm{km\,s^{-1}}$ in the rest of the map. Finally, in Fig. 23c, we show the ΔV_z map. This is equivalent to mapping breathing modes (contraction and expansion with respect to $z = 0$) as in Widrow et al. (2014). The absolute amplitude of the ΔV_z is about $2{-}4\,\mathrm{km\,s^{-1}}$, that is, much lower than in the ϕ and R components.

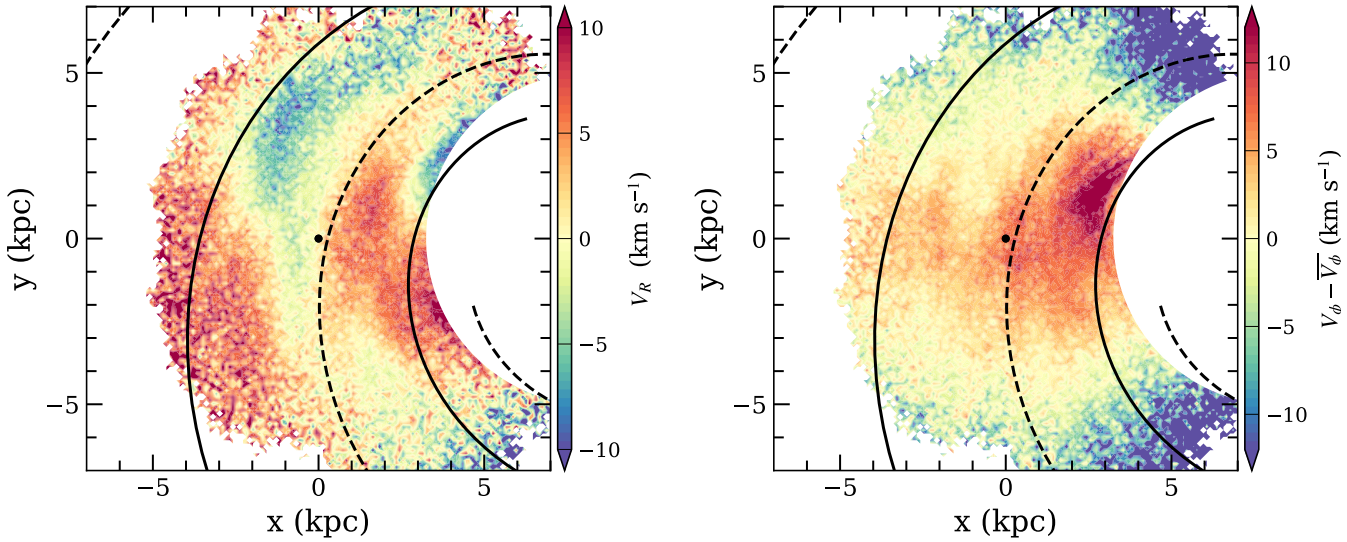


Fig. 22. Velocity maps for the RGB sample. *Left panel*: inferred radial velocity, V_R. *Right panel*: map for $V_\phi - \overline{V_\phi}$, i.e. the residual azimuthal velocity. Overlaid on both maps is the two-arm NIR spiral model from Drimmel (2000), shown as solid lines. The dashed lines correspond to the minimum inter-arm density (see text). The position of the Sun is marked by a black dot.

Nevertheless, the outer disc again shows a marked feature, but more towards the anticentre. We also note that at least one of the features in the ΔV_z map is roughly aligned with the location of the Perseus arm from Reid et al. (2019).

The ΔV map for the OB stars covers a much smaller extent of the disc, so we can only construct difference maps not much beyond 1 kpc from the disc. These are shown in the lower panels of Fig. 23, with the spiral overdensity contours overlaid as in Fig. 21. In Fig. 23d, we note that the residuals in ΔV_ϕ, are positive in between the arms. This would suggest that inside the arms, OB stars rotate faster in the upper disc. In Fig. 23e, we note that ΔV_R is generally negative inside the arms, implying that the OB stars in the upper disc move towards the Galactic centre inside these arms. In Fig. 21 we already noted that for the OB population, ΔV_R is generally negative between the arms; the ΔV_R map for the OB stars shows that this is stronger in the upper disc. Similarly, Fig. 21 also showed that the ΔV_ϕ residuals were also higher in the inter-arm region, and the ΔV_ϕ map shows that this is more prominent in the upper disc. This suggests that there may be some shearing motion in the R and ϕ directions associated with these arms, or that the spiral perturbation that aligns with the OB population is stronger in the upper disc. Finally, for completion, we also present the ΔV_z map for the OB stars in Fig. 23f. This map shows that there may be an associated breathing mode, although here we see a net expansion that may be aligned with the overdensity of the Local Arm. In general, the amplitude of the ΔV_k for the OB stars is much lower than for the RGB stars.

6. Discussion

In Sect. 4 we summarised the distribution of our four samples in the (x, y) plane. As expected, the younger samples indeed trace well-known spiral arm segments, confirming earlier results using *Gaia* EDR3 astrometry and young stellar samples selected using NIR photometry (Zari et al. 2021, P21). Segments of the nearest spiral arms are evident, although we made no attempt to derive the local stellar density. This would require an accurate 3D extinction map, as well as the selection function of the sample being used, which depends both on the survey selection function and on the criteria used to construct the sample of tracers (Rix et al. 2021). For instance, to compile our OB and RGB samples, we used the new astrophysical parameters in *Gaia* DR3, which are only available for a fraction of the stars. As reported in Creevey et al. (2023), Fouesneau et al. (2023) and Andrae et al. (2023), about half of the brighter stars lack astrophysical parameters, which leads to an artificial depression in the apparent stellar density within about 1 kpc of the Sun.

As already discussed in Sect. 4, extinction is responsible for sampling bias with respect to angle, leading to the evident radial features centred on the Sun. The radial features that are so obviously visible in the distribution of our sources are only weakly visible in the velocity and dispersion maps in Sect. 5, and they are a consequence of biased distance estimates. The fact that they are not very evident gives us confidence that we are justified in assuming that our samples are not kinematically biased and that the adopted distances are reliable. Nevertheless, as discussed in Sect. 3.4, beyond some limiting distance, the majority of stars in a given volume element will have overestimated distances, which in turn leads to an overestimated mean velocity component tangential to the line of sight. This causes a direction-dependent distance limit to the velocity maps beyond which systematic errors dominate. These systematic errors show symmetries with respect to the line from the Sun to the Galactic centre. For example, this signature is evident in the map of $V_\phi - \overline{V_\phi}$ (Fig. 22), showing high negative azimuthal velocities for distances beyond about 6 kpc in the directions of $40° < |l| < 60°$. Keeping in mind the principles noted at the end of Sect. 3.4, we discuss the kinematic maps presented in Sect. 5 below.

6.1. Kinematics

While the optical passband of *Gaia* limits its mapping capabilities in configuration space, it nevertheless samples the kinematics of the disc of the Milky Way to large distances. As is the usual practice, we assumed that our samples are not kinematically biased. This is a reasonable assumption as long as each sample either covers a limited range of ages or can be considered as kinematically relaxed and of common origin. In particular, we did not make any effort to distinguish between the young (thin-)

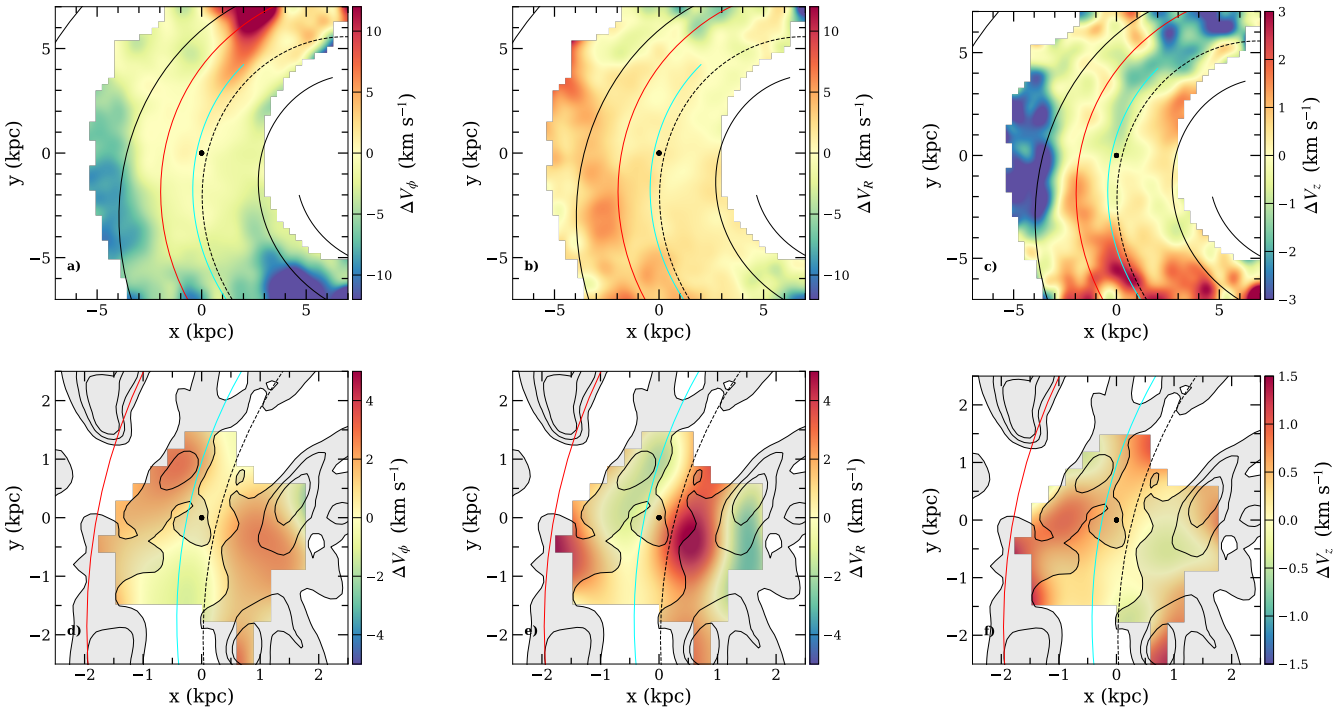


Fig. 23. Heliocentric maps of ΔV_i, i.e. $(V_{Z>0} - V_{Z<0})$, for the components $i = \phi, R, Z$, in the RGB sample (*top*) and the OB star sample (*bottom*). The NIR two-arm spiral model (black) from Drimmel (2000) is overplotted as well as are the Perseus (red), and the Local (cyan) Arms model from Reid et al. (2019). The position of the Sun is indicated by the black dot at $(x, y) = (0, 0)$.

disc stars and the old α-rich (thick-) disc in our RGB sample (Gaia Collaboration 2023a). With these assumptions and caveats in mind, we here discuss the astrophysical significance of some of the features that we noted in the velocity maps in the previous section.

The maps shown in Fig. 22 can be directly compared to the corresponding velocity maps from *Gaia* DR2 (Gaia Collaboration 2018a, their Figs. 19 and 20). While many of the features out to about 3 kpc were already mapped with *Gaia* DR2, we can now map a significantly larger portion of the disc based on the larger sample of stars with line-of-sight velocities. The new data reveal a complex and rich velocity field in the Galactic disc all the way to the Galactic centre, and the in-plane motions of the stars in the inner Galaxy spectacularly reveal the clear signature of the Galactic bar. In particular, we confirm the existence of a quadrupole pattern in the radial velocity field, as previously found by Bovy et al. (2019) and Queiroz et al. (2021). Additionally, we now clearly see the imprints of the Galactic bar on the azimuthal velocity field and on the stellar velocity dispersions. With the additional guidance provided from of a numerical simulation, we are able to estimate the aspect angle of the bar and its corotation radius through a simple bisymmetric model of the kinematic signature of the bar in the azimuthal velocity field. We find that the bar has an angle of 19.5 ± 2.5° with respect to the Sun-GC direction, as measured within $1.5 < R \leq 2.8$ kpc, and a corotation radius of 5.4 ± 0.5 kpc. Then, using the observed angular frequency, we deduce a lower limit of the bar pattern frequency of $\Omega_{\rm bar} = 38.1^{+2.6}_{-2}$ km s^{-1} kpc^{-1}, and an upper limit for the location of the outer Lindblad resonance of 9.7 ± 0.5 kpc within the framework of the epicycle approximation. Bland-Hawthorn & Gerhard (2016) compiled previous estimates of the corotation radius and gave $\Omega_{\rm bar} = 43 \pm 9$ km s^{-1} kpc^{-1} and a corotation radius range of 4.5–7 kpc. Applying the Tremaine-Weinberg method to their kinematic sample, Bovy et al. (2019) estimated a bar pattern speed of 41 ± 3 km s^{-1} kpc^{-1} and a corotation radius of 5.5 ± 0.4 kpc. Other works found 37.5 km s^{-1} kpc^{-1} (Clarke et al. 2019), 39 ± 3.5 km s^{-1} kpc^{-1} (Portail et al. 2017a) and 37.5–40 km s^{-1} kpc^{-1} (Li et al. 2022), which is based on hydrodynamical simulations and made-to-measure models. Our findings are thus in good agreement with other estimates of the fundamental parameters of the bar. For the bar orientation angle, Bland-Hawthorn & Gerhard (2016) compiled a range of 28°–33°, while other recent estimates range from 20° to 28° (e.g. Wegg et al. 2015; Portail et al. 2017b; Bovy et al. 2019; Queiroz et al. 2021). Our value is thus at the low end of the proposed range.

The outer disc has a large variety of features and streaming motions, which likely contain fundamental clues for the dynamical nature of the non-axisymmetric structures in the Milky Way. Monari et al. (2016) modelled the impact of the bar and a two-armed quasi-static spiral pattern in the Galactic disc, both simultaneously and separately. The comparison of the observed kinematic maps of the RGB stars confirms that the influence of the Galactic bar likely dominates even the outer portions of the disc out to at least $R = 11$ kpc. Faure et al. (2014) carried out test-particle simulations to predict the global stellar response to spiral perturbations in the Galactic disc in the absence of external excitation (e.g. from an accreting satellite). They integrated stellar orbits in a two-arm Lin-Shu-type spiral potential (without a bar) and produced maps of mean galactocentric radial velocity (V_R). They showed (their Fig. 6) that inside the spiral arm corotation radius, in the region traced by the arm, the mean V_R is negative (about −7 km s^{-1}), that is, stars have a bulk motion towards the Galactic centre. In the region between the arms, the stellar radial motion is positive, that is, stars have a bulk motion towards the anticentre. Outside corotation, the pattern is reversed. Trends in V_R induced by the spiral arms were also shown in

Antoja et al. (2016) and other works. In our sample of RGB stars, a spiral feature might be visible in the V_R maps, apparent as an elongated systematic positive feature, located inside the dashed line in Fig. 22 (left panel), marking the location of the minimum inter-arm density.

Other features are also seen in the ΔV maps that are worthy of note. Some of them might be explained as extinction artefacts (i.e. those that are elongated along the line-of-sight), while others are likely real. In particular, we see an asymmetry in all three components in the outer disc beyond $R = 10-11$ kpc in the RGB sample that does not yet have a clear explanation. This feature is likely related to an asymmetry already noted in Gaia Collaboration (2018a), where the authors followed the asymmetry in the azimuthal and vertical components, showing a clear bimodality in the (V_ϕ, V_z) plane. Stars are concentrated mainly in two clumps, one with negative V_z at lower V_ϕ, which is more prominent in the north, and one with positive V_z at higher V_ϕ, which is more visible in the south. The different proportions of the clumps of the bimodality at different Z seems to be the cause of the asymmetry.

For the OB sample, one of the main results is that the velocity field of the OB stars shows streaming motions that have a characteristic length similar to the spiral arm density. This has never been shown with such detail in 2D maps for OB stars. We recall, however, that our sample of OB stars is expected to trace the local (out to ≈2−2.5 kpc in heliocentric distance) motions of the gas, rather than the large-scale features of the Galaxy, as they inherit the motion of the gas from which they were recently born. However, because the region sampled by our OB sample is relatively small, the streaming motions in the OB stars really map only the Local Arm.

A comparison between the OB and RGB star velocity fields revealed numerous differences. The observed differences are not unexpected because these two samples trace dynamically cold and hot stellar populations of the Milky Way. In the OB stars, we clearly see streaming motions that are associated with the spiral structure of this population. In contrast, the signature of the spiral arms in the RGB sample is not clearly evident, and, if present, is seen in the radial motions. In any case, if there is a signature of streaming motions related to the spiral arms in the RGB sample, it is consistent with a two-armed structure, possibly driven by the bar.

6.2. Caveats and shortcomings

No method or procedure is perfect, and here we have adopted one that is certainly not without imperfections. In this section we confess all of our sins.

In Sect. 5 we constructed maps of the mean velocity field in galactocentric cylindrical coordinates based on the derived velocities in the same coordinates as the individual sources. These in turn were derived from the individual measures of the proper motions and estimated distances. While our method is relatively straightforward, it has several shortcomings that should be addressed in the future. Beyond a distance of about 3 kpc, the largest source of uncertainty in our velocity maps is derived from the distance uncertainties, yet our treatment of these is not completely satisfactory.

Our distances are taken from CBJ2021, who used a Bayesian approach to estimate the distances from astrometry and photometry, incorporating a prior that includes both current astrophysical knowledge of stellar structure and some informed assumptions about Galactic structure. The probability distribution of the individual distances is asymmetric in general, but we rendered them symmetric in order to apply a traditional approach to propagating the uncertainties to galactocentric coordinates that implicitly assume that the uncertainties are symmetric. As discussed in Sect. 3.3, this was done in part out of necessity as we are not able to sample the probability distribution function of the distance for each star.

We assumed no correlation between the distance and proper motion uncertainties. This cannot be true because these distances are partly informed by the parallax. On the other hand, as pointed out in Sect. 3, these correlations are likely to be unimportant at larger distances, where the distances are more constrained by the photometry than the astrometry.

When propagating our uncertainties, we accounted for the correlations introduced by the coordinate transforms and distance uncertainties, which would result in a correlation between the two velocity components in galactocentric coordinates. However, we did not take these correlations into account when we estimated the mean velocity field in Sect. 5.

Most grievously, when estimating the mean velocity and velocity dispersion for a given volume element, we only considered stars found in this small volume element, according to their estimated distances. That is, although we took the uncertainties of the distances into account when we derived the uncertainties in the individual velocities, we implicitly assumed that these distances were perfect when we binned the stars into cells to estimate the mean velocity field and velocity dispersions.

Finally, we recall that the CBJ2021 distance estimates are based on a prior that includes a bar with an assumed geometry. As this prior becomes increasingly important with increasing distance, there is reason for concern that our velocity field may be influenced by this prior. In addition to the CBJ2021 photogeometric distances, we attempted to use different distance estimates: the CBJ2021 geometric distances show very similar results, Starhorse3 (Anders et al. 2022) distances also show a similar bisymmetric behaviour, while GSP-Phot distances have a similar trend but at an incorrect distance. As mentioned above, all these distance estimators have a prior that includes a bar. In any case, we stress that this potentially introduces a bias in the derived velocity field that is not considered in our qualitative comparison with simulated data.

7. Conclusions

Using *Gaia* DR3, we have mapped the kinematics of the stars over an extensive area of the Milky Way disc. This has been made possible by the new line-of-sight (radial) velocities, and by new and reliable astrophysical parameters that have allowed us to distinguish between young (OB) and old (RGB) stars. While our sample of OB stars with 6D space and velocity data is much more limited, their kinematics are seen to be distinctly different than those of RGB stars, likely reflecting the complex motions of the gas from which they were recently born. Our RGB sample has allowed us to map the kinematics of the Galaxy over nearly a quarter of the disc, providing us a first clear picture of the large-scale kinematic signature of the bar. In order to interpret the features seen in the kinematic maps, we relied on simple comparisons with a simulation of a barred galaxy.

In contrast to the bar signature, clear evidence of streaming motions associated with spiral arms is much less evident and, if present, is consistent with the two-armed structure that we see in the NIR. With regard to the non-axisymmetric structure in 3D configuration space, we made no attempt to reconstruct the stellar density. Nevertheless, we were able to map the young OB sample and young clusters out to 4 to 5 kpc from the Sun,

confirming previous findings that the Local Arm has a length of at least 8 kpc. While weaker than the inner Sag-Car arm or the outer Perseus arm, it seems its nomenclature is perhaps not so appropriate, and we should return to its original designation as the Orion arm (van de Hulst et al. 1954).

This study should only be considered as a preliminary exploration of what *Gaia* DR3 has to offer with regard to Galactic structure. Our kinematic maps are derived from velocities of individual stars based on individual distance estimates. A better approach would be a derivation of the velocity field recognising that the velocities, like the distances, should be inferred quantities rather than derived quantities, as we have treated them here. With regard to Galactic dynamics, the individual velocities are not of direct interest to us at all. Instead, an appropriate model of the mean velocity field should be adopted and incorporated in the prior, and the relevant parameters of the model (e.g. the bar orientation) should then be adjusted to arrive at the most likely set of parameter values given the data. Alternatively, a suite of simulations of the kinematics of the Milky Way could be generated, assuming different bar parameters, and the uncertainties modelled to transform them into a suite of mock catalogues. The one that best matches the *Gaia* data could then be determined. In either case, any fitting should ideally be made against the measurements in data-space rather than in model-space, and take the selection effects on the data into account.

Although we have only taken a first look at the treasure trove of data that *Gaia* DR3 has to offer, it is clear that the *Gaia* mission continues to fulfil its promise to provide the information needed to eventually arrive at a complete understanding of the dynamical state and processes at work in shaping our Galaxy. We can certainly expect further discoveries and insights from the community in the future as it digests this latest census of the stars in our Milky Way.

Acknowledgements. R.D. would like to thank Robert Benjamin for helpful discussions on the treacherous history of mapping the spiral structure of our Galaxy. This work presents results from the European Space Agency (ESA) space mission *Gaia*. *Gaia* data are being processed by the *Gaia* Data Processing and Analysis Consortium (DPAC). Funding for the DPAC is provided by national institutions, in particular the institutions participating in the *Gaia* MultiLateral Agreement (MLA). The *Gaia* mission website is `https://www.cosmos.esa.int/gaia`. The *Gaia* archive website is `https://archives.esac.esa.int/gaia`. This work has used the following software products: TOPCAT (`http://www.starlink.ac.uk/topcat/`), STIL (`http://www.starlink.ac.uk/stil`), and STILTS (`http://www.starlink.ac.uk/stilts`) (Taylor 2005, 2006); Matplotlib (Hunter 2007); IPython (Pérez & Granger 2007); Astropy, a community-developed core Python package for Astronomy (Astropy Collaboration 2018). Full acknowledgements are given in Appendix D.

References

Abdurro'uf, Accetta, K., & Aerts, C., et al. 2022, ApJS, 259, 35
Abolfathi, B., Aguado, D. S., Aguilar, G., et al. 2018, ApJS, 235, 42
Allen, C., & Santillan, A. 1991, Rev. Mex. Astron. Astrofis., 22, 255
Alves, D. R. 2000, ApJ, 539, 732
Anders, F., Khalatyan, A., Queiroz, A. B. A., et al. 2022, A&A, 658, A91
Anderson, R. I., Eyer, L., & Mowlavi, N. 2013, MNRAS, 434, 2238
Anderson, R. I., Saio, H., Ekström, S., Georgy, C., & Meynet, G. 2016, A&A, 591, A8
Anderson, L. D., Wenger, T. V., Armentrout, W. P., Balser, D. S., & Bania, T. M. 2019, ApJ, 871, 145
Andrae, R., Fouesneau, M., Sordo, R., et al. 2023, A&A, 674, A27 (*Gaia* DR3 SI)
Antoja, T., Roca-Fàbrega, S., de Bruijne, J., & Prusti, T. 2016, A&A, 589, A13
Antoja, T., Helmi, A., Romero-Gómez, M., et al. 2018, Nature, 561, 360
Antoja, T., Ramos, P., Mateu, C., et al. 2020, A&A, 635, L3
Astropy Collaboration (Price-Whelan, A., et al.) 2018, AJ, 156, 123
Babusiaux, C., Fabricius, C., Khanna, S., et al. 2023, A&A, 674, A32 (*Gaia* DR3 SI)
Bailer-Jones, C. A. L. 2015, PASP, 127, 994
Bailer-Jones, C. A. L., Rybizki, J., Fouesneau, M., Demleitner, M., & Andrae, R. 2021, AJ, 161, 147
Belokurov, V., Erkal, D., Evans, N. W., Koposov, S. E., & Deason, A. J. 2018, MNRAS, 478, 611
Bennett, M., & Bovy, J. 2019, MNRAS, 482, 1417
Blaauw, A., Gum, C. S., Pawsey, J. L., & Westerhout, G. 1960, MNRAS, 121, 123
Bland-Hawthorn, J., & Gerhard, O. 2016, ARA&A, 54, 529
Blomme, R., Frémat, Y., Sartoretti, P., et al. 2023, A&A, 674, A7 (*Gaia* DR3 SI)
Bono, G., Marconi, M., Cassisi, S., et al. 2005, ApJ, 621, 966
Bovy, J., Bird, J. C., García Pérez, A. E., et al. 2015, ApJ, 800, 83
Bovy, J., Leung, H. W., Hunt, J. A. S., et al. 2019, MNRAS, 490, 4740
Brown, A. G. A. 2021, ARA&A, 59, 59
Cantat-Gaudin, T., Jordi, C., Vallenari, A., et al. 2018, A&A, 618, A93
Cantat-Gaudin, T., Anders, F., Castro-Ginard, A., et al. 2020, A&A, 640, A1
Cardelli, J. A., Clayton, G. C., & Mathis, J. S. 1989, ApJ, 345, 245
Carlin, J. L., DeLaunay, J., Newberg, H. J., et al. 2013, ApJ, 777, L5
Castro-Ginard, A., Jordi, C., Luri, X., Cantat-Gaudin, T., & Balaguer-Núñez, L. 2019, A&A, 627, A35
Castro-Ginard, A., Jordi, C., Luri, X., et al. 2022, A&A, 661, A118
Churchwell, E., Babler, B. L., Meade, M. R., et al. 2009, PASP, 121, 213
Clarke, J. P., Wegg, C., Gerhard, O., et al. 2019, MNRAS, 489, 3519
Clementini, G., Ripepi, V., Leccia, S., et al. 2016, A&A, 595, A133
Clementini, G., Ripepi, V., Molinaro, R., et al. 2019, A&A, 622, A60
Clementini, G., Ripepi, V., Garofalo, A., et al. 2023, A&A, 674, A18 (*Gaia* DR3 SI)
Creevey, O. L., Sordo, R., Pailler, F., et al. 2023, A&A, 674, A26 (*Gaia* DR3 SI)
Cui, X.-Q., Zhao, Y.-H., Chu, Y.-Q., et al. 2012, Res. Astron. Astrophys., 12, 1197
Deepak, & Reddy, B. E. 2018, AJ, 156, 170
De Silva, G. M., Freeman, K. C., Bland-Hawthorn, J., et al. 2015, MNRAS, 449, 2604
De Somma, G., Marconi, M., Cassisi, S., et al. 2021, MNRAS, 508, 1473
Do, T., Hees, A., Ghez, A., et al. 2019, Science, 365, 664
Drimmel, R. 2000, A&A, 358, L13
Drimmel, R., & Poggio, E. 2018, Res. Notes Am. Astron. Soc., 2, 210
Drimmel, R., Cabrera-Lavers, A., & López-Corredoira, M. 2003, A&A, 409, 205
Faure, C., Siebert, A., & Famaey, B. 2014, MNRAS, 440, 2564
Feast, M. W., & Catchpole, R. M. 1997, MNRAS, 286, L1
Ferrers, N. 1877, Q. J. Pure Appl. Math., 14, 1
Foreman-Mackey, D., Hogg, D. W., Lang, D., & Goodman, J. 2013, PASP, 125, 306
Fouesneau, M., Frémat, Y., Andrae, R., et al. 2023, A&A, 674, A28 (*Gaia* DR3 SI)
Fragkoudi, F., Katz, D., Trick, W., et al. 2019, MNRAS, 488, 3324
Gaia Collaboration (Katz, D., et al.) 2018a, A&A, 616, A11
Gaia Collaboration (Brown, A. G. A., et al.) 2018b, A&A, 616, A1
Gaia Collaboration (Antoja, T., et al.) 2021a, A&A, 649, A8
Gaia Collaboration (Smart, R. L., et al.) 2021b, A&A, 649, A6
Gaia Collaboration (Brown, A. G. A., et al.) 2021c, A&A, 649, A1
Gaia Collaboration (Luri, X., et al.) 2021d, A&A, 649, A7
Gaia Collaboration (Klioner, S. A., et al.) 2022, A&A, 667, A148
Gaia Collaboration (Recio-Blanco, A., et al.) 2023a, A&A, 674, A38 (*Gaia* DR3 SI)
Gaia Collaboration (Creevey, O. L., et al.) 2023b, A&A, 674, A39 (*Gaia* DR3 SI)
GRAVITY Collaboration (Abuter, R., et al.) 2022, A&A, 657, L12
Gualandris, A., & Merritt, D. 2008, ApJ, 678, 780
Gum, C. S., Kerr, F. J., & Westerhout, G. 1960, MNRAS, 121, 132
Helmi, A., Babusiaux, C., Koppelman, H. H., et al. 2018, Nature, 563, 85
Hou, L. G. 2021, Front. Astron. Space Sci., 8, 103
Hunt, J. A. S., & Bovy, J. 2018, MNRAS, 477, 3945
Hunt, J. A. S., Bub, M. W., Bovy, J., et al. 2019, MNRAS, 490, 1026
Hunter, J. D. 2007, Comput. Sci. Eng., 9, 90
Inno, L., Rix, H.-W., Stanek, K. Z., et al. 2021, ApJ, 914, 127
Jönsson, H., Holtzman, J. A., Allende Prieto, C., et al. 2020, AJ, 160, 120
Jurić, M., Ivezić, Ž., Brooks, A., et al. 2008, ApJ, 673, 864
Katz, D., Sartoretti, P., Cropper, M., et al. 2019, A&A, 622, A205
Katz, D., Sartoretti, P., Guerrier, A., et al. 2023, A&A, 674, A5 (*Gaia* DR3 SI)
Khanna, S., Sharma, S., Tepper-Garcia, T., et al. 2019a, MNRAS, 489, 4962
Khanna, S., Sharma, S., Bland-Hawthorn, J., et al. 2019b, MNRAS, 482, 4215
Khoperskov, S., & Gerhard, O. 2022, A&A, 663, A38

Laporte, C. F. P., Famaey, B., Monari, G., et al. 2020, A&A, 643, L3
Leung, H. W., Bovy, J., Mackereth, J. T., et al. 2022, MNRAS, 519, 948
Levine, E. S., Blitz, L., & Heiles, C. 2006, Science, 312, 1773
Li, Z., Shen, J., Gerhard, O., & Clarke, J. P. 2022, ApJ, 925, 71
Lindegren, L., Bastian, U., Biermann, M., et al. 2021, A&A, 649, A4
López-Corredoira, M., & Sylos Labini, F. 2019, A&A, 621, A48
Luri, X., Brown, A. G. A., Sarro, L. M., et al. 2018, A&A, 616, A9
Madore, B. F. 1982, ApJ, 253, 575
Majewski, S. R., Schiavon, R. P., Frinchaboy, P. M., et al. 2017, AJ, 154, 94
Marasco, A., Fraternali, F., van der Hulst, J. M., & Oosterloo, T. 2017, A&A, 607, A106
Mathur, S., Huber, D., Batalha, N. M., et al. 2017, ApJS, 229, 30
Miyamoto, M., & Nagai, R. 1975, PASJ, 27, 533
Monari, G., Famaey, B., Siebert, A., et al. 2016, MNRAS, 461, 3835
Monari, G., Famaey, B., Siebert, A., Wegg, C., & Gerhard, O. 2019, A&A, 626, A41
Morgan, W. W., Whitford, A. E., & Code, A. D. 1953, ApJ, 118, 318
Peek, J. E. G., Tchernyshyov, K., & Miville-Deschenes, M.-A. 2022, ApJ, 925, 201
Pérez, F., & Granger, B. E. 2007, Comput. Sci. Eng., 9, 21
Pietrukowicz, P., Soszyński, I., & Udalski, A. 2021, Acta Astron., 71, 205
Poggio, E., Drimmel, R., Lattanzi, M. G., et al. 2018, MNRAS, 481, L21
Poggio, E., Drimmel, R., Andrae, R., et al. 2020, Nat. Astron., 4, 590
Poggio, E., Drimmel, R., Cantat-Gaudin, T., et al. 2021, A&A, 651, A104
Portail, M., Gerhard, O., Wegg, C., & Ness, M. 2017a, MNRAS, 465, 1621
Portail, M., Wegg, C., Gerhard, O., & Ness, M. 2017b, MNRAS, 470, 1233
Queiroz, A. B. A., Chiappini, C., Perez-Villegas, A., et al. 2021, A&A, 656, A156
Ramos, P., Antoja, T., & Figueras, F. 2018, A&A, 619, A72
Reid, M. J., & Brunthaler, A. 2020, ApJ, 892, 39
Reid, M. J., Menten, K. M., Brunthaler, A., et al. 2019, ApJ, 885, 131
Riello, M., De Angeli, F., Evans, D. W., et al. 2021, A&A, 649, A3
Ripepi, V., Molinaro, R., Musella, I., et al. 2019, A&A, 625, A14
Ripepi, V., Catanzaro, G., Clementini, G., et al. 2022, A&A, 659, A167
Ripepi, V., Clementini, G., Molinaro, S., et al. 2023, A&A, 674, A17 (*Gaia* DR3 SI)
Rix, H.-W., Hogg, D. W., Boubert, D., et al. 2021, AJ, 162, 142
Romero-Gómez, M., Figueras, F., Antoja, T., Abedi, H., & Aguilar, L. 2015, MNRAS, 447, 218
Romero-Gómez, M., Mateu, C., Aguilar, L., Figueras, F., & Castro-Ginard, A. 2019, A&A, 627, A150
Rybizki, J., Green, G. M., Rix, H.-W., et al. 2022, MNRAS, 510, 2597
Sartoretti, P., Blomme, R., David, M., & Seabroke, G. 2022, Gaia DR3 Documentation Chapter 6: Spectroscopy
Spekkens, K., & Sellwood, J. A. 2007, ApJ, 664, 204
Steinmetz, M., Matijevič, G., Enke, H., et al. 2020, AJ, 160, 82
Tarricq, Y., Soubiran, C., Casamiquela, L., et al. 2022, A&A, 659, A59
Taylor, J. H., & Cordes, J. M. 1993, ApJ, 411, 674
Taylor, M. B. 2005, ASP Conf. Ser., 347, 29
Taylor, M. B. 2006, ASP Conf. Ser., 351, 666
Tepper-Garcia, T., Bland-Hawthorn, J., Vasiliev, E., et al. 2021, ArXiv e-prints [arXiv:2111.05466]
Trick, W. H., Coronado, J., & Rix, H.-W. 2019, MNRAS, 484, 3291
Trick, W. H., Fragkoudi, F., Hunt, J. A. S., Mackereth, J. T., & White, S. D. M. 2021, MNRAS, 500, 2645
van de Hulst, H. C., Muller, C. A., & Oort, J. H. 1954, Bull. Astron. Inst. Neth., 12, 117
Vasiliev, E., & Baumgardt, H. 2021, MNRAS, 505, 5978
Wegg, C., Gerhard, O., & Portail, M. 2015, MNRAS, 450, 4050
Widmark, A. 2019, A&A, 623, A30
Widrow, L. M., Gardner, S., Yanny, B., Dodelson, S., & Chen, H.-Y. 2012, ApJ, 750, L41
Widrow, L. M., Barber, J., Chequers, M. H., & Cheng, E. 2014, MNRAS, 440, 1971
Williams, M. E. K., Steinmetz, M., Binney, J., et al. 2013, MNRAS, 436, 101
Xiang, M., Rix, H.-W., Ting, Y.-S., et al. 2022, A&A, 662, A66
Yao, J. M., Manchester, R. N., & Wang, N. 2017, MNRAS, 468, 3289
York, D. G., Adelman, J., Anderson, J. E., Jr., et al. 2000, AJ, 120, 1579
Zari, E., Rix, H. W., Frankel, N., et al. 2021, A&A, 650, A112
Zhao, G., Zhao, Y.-H., Chu, Y.-Q., Jing, Y.-P., & Deng, L.-C. 2012, Res. Astron. Astrophys., 12, 723

[1] INAF – Osservatorio Astrofisico di Torino, Via Osservatorio 20, 10025 Pino Torinese, TO, Italy
[2] Institut de Ciències del Cosmos (ICCUB), Universitat de Barcelona (IEEC-UB), Martí i Franquès 1, 08028 Barcelona, Spain
[3] Centro de Astronomía – CITEVA, Universidad de Antofagasta, Avenida Angamos 601, Antofagasta 1270300, Chile
[4] Université de Strasbourg, CNRS, Observatoire astronomique de Strasbourg, UMR 7550, 11 Rue de l'Université, 67000 Strasbourg, France
[5] Université Côte d'Azur, Observatoire de la Côte d'Azur, CNRS, Laboratoire Lagrange, Bd de l'Observatoire, CS 34229, 06304 Nice Cedex 4, France
[6] INAF – Osservatorio Astronomico di Capodimonte, Via Moiariello 16, 80131 Napoli, Italy
[7] Max Planck Institute for Astronomy, Königstuhl 17, 69117 Heidelberg, Germany
[8] Royal Observatory of Belgium, Ringlaan 3, 1180 Brussels, Belgium
[9] Leiden Observatory, Leiden University, Niels Bohrweg 2, 2333 CA Leiden, The Netherlands
[10] INAF – Osservatorio di Astrofisica e Scienza dello Spazio di Bologna, Via Piero Gobetti 93/3, 40129 Bologna, Italy
[11] Radagast Solutions, Simon Vestdijkpad 24, 2321WD Leiden, The Netherlands
[12] Kapteyn Astronomical Institute, University of Groningen, Landleven 12, 9747 AD Groningen, The Netherlands
[13] IRAP, Université de Toulouse, CNRS, UPS, CNES, 9 Av. colonel Roche, BP 44346, 31028 Toulouse Cedex 4, France
[14] INAF – Osservatorio Astronomico di Padova, Vicolo Osservatorio 5, 35122 Padova, Italy
[15] European Space Agency (ESA), European Space Research and Technology Centre (ESTEC), Keplerlaan 1, 2201 AZ Noordwijk, The Netherlands
[16] GEPI, Observatoire de Paris, Université PSL, CNRS, 5 Place Jules Janssen, 92190 Meudon, France
[17] Univ. Grenoble Alpes, CNRS, IPAG, 38000 Grenoble, France
[18] Astronomisches Rechen-Institut, Zentrum für Astronomie der Universität Heidelberg, Mönchhofstr. 12-14, 69120 Heidelberg, Germany
[19] Laboratoire d'Astrophysique de Bordeaux, Univ. Bordeaux, CNRS, B18N, Allée Geoffroy Saint-Hilaire, 33615 Pessac, France
[20] Institute of Astronomy, University of Cambridge, Madingley Road, Cambridge CB3 0HA, UK
[21] Department of Astronomy, University of Geneva, Chemin Pegasi 51, 1290 Versoix, Switzerland
[22] European Space Agency (ESA), European Space Astronomy Centre (ESAC), Camino Bajo del Castillo, s/n, Urbanizacion Villafranca del Castillo, Villanueva de la Cañada 28692, Madrid, Spain
[23] Aurora Technology for European Space Agency (ESA), Camino Bajo del Castillo, s/n, Urbanizacion Villafranca del Castillo, Villanueva de la Cañada 28692, Madrid, Spain
[24] Lohrmann Observatory, Technische Universität Dresden, Mommsenstraße 13, 01062 Dresden, Germany
[25] Lund Observatory, Department of Astronomy and Theoretical Physics, Lund University, Box 43, 22100 Lund, Sweden
[26] CNES Centre Spatial de Toulouse, 18 Avenue Edouard Belin, 31401 Toulouse Cedex 9, France
[27] Institut d'Astronomie et d'Astrophysique, Université Libre de Bruxelles CP 226, Boulevard du Triomphe, 1050 Brussels, Belgium
[28] F.R.S.-FNRS, Rue d'Egmont 5, 1000 Brussels, Belgium
[29] INAF – Osservatorio Astrofisico di Arcetri, Largo Enrico Fermi 5, 50125 Firenze, Italy
[30] European Space Agency (ESA), Noordwijk, The Netherlands
[31] University of Turin, Department of Physics, Via Pietro Giuria 1, 10125 Torino, Italy
[32] DAPCOM for Institut de Ciències del Cosmos (ICCUB), Universitat de Barcelona (IEEC-UB), Martí i Franquès 1, 08028 Barcelona, Spain
[33] Observational Astrophysics, Division of Astronomy and Space Physics, Department of Physics and Astronomy, Uppsala University, Box 516, 751 20 Uppsala, Sweden
[34] ALTEC S.p.a, Corso Marche, 79, 10146 Torino, Italy
[35] Sednai Sàrl, Geneva, Switzerland

[36] Department of Astronomy, University of Geneva, Chemin d'Ecogia 16, 1290 Versoix, Switzerland
[37] Mullard Space Science Laboratory, University College London, Holmbury St Mary, Dorking, Surrey RH5 6NT, UK
[38] Gaia DPAC Project Office, ESAC, Camino Bajo del Castillo, s/n, Urbanizacion Villafranca del Castillo, Villanueva de la Cañada 28692, Madrid, Spain
[39] Telespazio UK S.L. for European Space Agency (ESA), Camino Bajo del Castillo s/n, Urbanizacion Villafranca del Castillo, Villanueva de la Cañada 28692, Madrid, Spain
[40] SYRTE, Observatoire de Paris, Université PSL, CNRS, Sorbonne Université, LNE, 61 Avenue de l'Observatoire, 75014 Paris, France
[41] National Observatory of Athens, I. Metaxa and Vas. Pavlou, Palaia Penteli, 15236 Athens, Greece
[42] IMCCE, Observatoire de Paris, Université PSL, CNRS, Sorbonne Université, Univ. Lille, 77 Av. Denfert-Rochereau, 75014 Paris, France
[43] Serco Gestión de Negocios for European Space Agency (ESA), Camino Bajo del Castillo s/n, Urbanizacion Villafranca del Castillo, Villanueva de la Cañada 28692, Madrid, Spain
[44] Institut d'Astrophysique et de Géophysique, Université de Liège, 19c, Allée du 6 Août, 4000 Liège, Belgium
[45] CRAAG – Centre de Recherche en Astronomie, Astrophysique et Géophysique, Route de l'Observatoire Bp 63 Bouzareah, 16340 Algiers, Algeria
[46] Institute for Astronomy, University of Edinburgh, Royal Observatory, Blackford Hill, Edinburgh EH9 3HJ, UK
[47] RHEA for European Space Agency (ESA), Camino Bajo del Castillo s/n, Urbanizacion Villafranca del Castillo, Villanueva de la Cañada 28692, Madrid, Spain
[48] ATG Europe for European Space Agency (ESA), Camino Bajo del Castillo s/n, Urbanizacion Villafranca del Castillo, Villanueva de la Cañada 28692, Madrid, Spain
[49] CIGUS CITIC – Department of Computer Science and Information Technologies, University of A Coruña, Campus de Elviña s/n, A Coruña 15071, Spain
[50] Kavli Institute for Cosmology Cambridge, Institute of Astronomy, Madingley Road, Cambridge CB3 0HA, USA
[51] Leibniz Institute for Astrophysics Potsdam (AIP), An der Sternwarte 16, 14482 Potsdam, Germany
[52] CENTRA, Faculdade de Ciências, Universidade de Lisboa, Edif. C8, Campo Grande, 1749-016 Lisboa, Portugal
[53] Department of Informatics, Donald Bren School of Information and Computer Sciences, University of California, Irvine, 5226 Donald Bren Hall, 92697-3440, CA Irvine, USA
[54] INAF – Osservatorio Astrofisico di Catania, Via S. Sofia 78, 95123 Catania, Italy
[55] Dipartimento di Fisica e Astronomia "Ettore Majorana", Università di Catania, Via S. Sofia 64, 95123 Catania, Italy
[56] INAF – Osservatorio Astronomico di Roma, Via Frascati 33, 00078 Monte Porzio Catone, Roma, Italy
[57] Space Science Data Center – ASI, Via del Politecnico SNC, 00133 Roma, Italy
[58] Department of Physics, University of Helsinki, PO Box 64, 00014 Helsinki, Finland
[59] Finnish Geospatial Research Institute FGI, Geodeetinrinne 2, 02430 Masala, Finland
[60] Institut UTINAM CNRS UMR6213, Université Bourgogne Franche-Comté, OSU THETA Franche-Comté Bourgogne, Observatoire de Besançon, BP 1615, 25010 Besançon Cedex, France
[61] HE Space Operations BV for European Space Agency (ESA), Keplerlaan 1, 2201 AZ Noordwijk, The Netherlands
[62] Dpto. de Inteligencia Artificial, UNED, c/ Juan del Rosal 16, 28040 Madrid, Spain
[63] Konkoly Observatory, Research Centre for Astronomy and Earth Sciences, Eötvös Loránd Research Network (ELKH), MTA Centre of Excellence, Konkoly Thege Miklós út 15-17, 1121 Budapest, Hungary
[64] ELTE Eötvös Loránd University, Institute of Physics, 1117 Pázmány Péter sétány 1A, Budapest, Hungary
[65] Instituut voor Sterrenkunde, KU Leuven, Celestijnenlaan 200D, 3001 Leuven, Belgium
[66] Department of Astrophysics/IMAPP, Radboud University, PO Box 9010, 6500 GL Nijmegen, The Netherlands
[67] University of Vienna, Department of Astrophysics, Türkenschanzstraße 17, 1180 Vienna, Austria
[68] Institute of Physics, Laboratory of Astrophysics, Ecole Polytechnique Fédérale de Lausanne (EPFL), Observatoire de Sauverny, 1290 Versoix, Switzerland
[69] School of Physics and Astronomy/Space Park Leicester, University of Leicester, University Road, Leicester LE1 7RH, UK
[70] Thales Services for CNES Centre Spatial de Toulouse, 18 Avenue Edouard Belin, 31401 Toulouse Cedex 9, France
[71] Depto. Estadística e Investigación Operativa, Universidad de Cádiz, Avda. República Saharaui s/n, 11510 Puerto Real, Cádiz, Spain
[72] Center for Research and Exploration in Space Science and Technology, University of Maryland Baltimore County, 1000 Hilltop Circle, Baltimore, MD, USA
[73] GSFC – Goddard Space Flight Center, Code 698, 8800 Greenbelt Rd, 20771, MD Greenbelt, USA
[74] EURIX S.r.l., Corso Vittorio Emanuele II 61, 10128 Torino, Italy
[75] Porter School of the Environment and Earth Sciences, Tel Aviv University, Tel Aviv 6997801, Israel
[76] Harvard-Smithsonian Center for Astrophysics, 60 Garden St., MS 15, Cambridge, MA 02138, USA
[77] HE Space Operations BV for European Space Agency (ESA), Camino Bajo del Castillo s/n, Urbanizacion Villafranca del Castillo, Villanueva de la Cañada 28692, Madrid, Spain
[78] Instituto de Astrofísica e Ciências do Espaço, Universidade do Porto, CAUP, Rua das Estrelas, 4150-762 Porto, Portugal
[79] LFCA/DAS,Universidad de Chile, CNRS, Casilla 36-D, Santiago, Chile
[80] SISSA – Scuola Internazionale Superiore di Studi Avanzati, Via Bonomea 265, 34136 Trieste, Italy
[81] Telespazio for CNES Centre Spatial de Toulouse, 18 Avenue Edouard Belin, 31401 Toulouse Cedex 9, France
[82] University of Turin, Department of Computer Sciences, Corso Svizzera 185, 10149 Torino, Italy
[83] Dpto. de Matemática Aplicada y Ciencias de la Computación, Univ. de Cantabria, ETS Ingenieros de Caminos, Canales y Puertos, Avda. de los Castros s/n, 39005 Santander, Spain
[84] DLR Gesellschaft für Raumfahrtanwendungen (GfR), mbH Münchener Straße 20, 82234 Weßling, Germany
[85] Centre for Astrophysics Research, University of Hertfordshire, College Lane, AL10 9AB Hatfield, UK
[86] University of Turin, Mathematical Department "G. Peano", Via Carlo Alberto 10, 10123 Torino, Italy
[87] INAF – Osservatorio Astronomico d'Abruzzo, Via Mentore Maggini, 64100 Teramo, Italy
[88] Instituto de Astronomia, Geofísica e Ciências Atmosféricas, Universidade de São Paulo, Rua do Matão, 1226, Cidade Universitaria, 05508-900 São Paulo, SP, Brazil
[89] APAVE SUDEUROPE SAS for CNES Centre Spatial de Toulouse, 18 Avenue Edouard Belin, 31401 Toulouse Cedex 9, France
[90] Mésocentre de calcul de Franche-Comté, Université de Franche-Comté, 16 Route de Gray, 25030 Besançon Cedex, France
[91] ATOS for CNES Centre Spatial de Toulouse, 18 Avenue Edouard Belin, 31401 Toulouse Cedex 9, France
[92] School of Physics and Astronomy, Tel Aviv University, Tel Aviv 6997801, Israel
[93] Astrophysics Research Centre, School of Mathematics and Physics, Queen's University Belfast, Belfast BT7 1NN, UK
[94] Centre de Données Astronomique de Strasbourg, Strasbourg, France
[95] Institute for Computational Cosmology, Department of Physics, Durham University, Durham DH1 3LE, UK

[96] European Southern Observatory, Karl-Schwarzschild-Str. 2, 85748 Garching, Germany
[97] Max-Planck-Institut für Astrophysik, Karl-Schwarzschild-Straße 1, 85748 Garching, Germany
[98] Data Science and Big Data Lab., Pablo de Olavide University, 41013 Seville, Spain
[99] Barcelona Supercomputing Center (BSC), Plaça Eusebi Güell 1-3, 08034 Barcelona, Spain
[100] ETSE Telecomunicación, Universidade de Vigo, Campus Lagoas-Marcosende, 36310 Vigo, Galicia, Spain
[101] Asteroid Engineering Laboratory, Space Systems, Luleå University of Technology, Box 848, 981 28 Kiruna, Sweden
[102] Vera C. Rubin Observatory, 950 N. Cherry Avenue, Tucson, AZ 85719, USA
[103] Department of Astrophysics, Astronomy and Mechanics, National and Kapodistrian University of Athens, Panepistimiopolis Zografos 15783, Athens, Greece
[104] TRUMPF Photonic Components GmbH, Lise-Meitner-Straße 13, 89081 Ulm, Germany
[105] IAC – Instituto de Astrofisica de Canarias, Via Láctea s/n, 38200 La Laguna S.C., Tenerife, Spain
[106] Department of Astrophysics, University of La Laguna, Via Láctea s/n, 38200 La Laguna S.C., Tenerife, Spain
[107] Faculty of Aerospace Engineering, Delft University of Technology, Kluyverweg 1, 2629 HS Delft, The Netherlands
[108] Laboratoire Univers et Particules de Montpellier, CNRS Université Montpellier, Place Eugène Bataillon, CC72, 34095 Montpellier Cedex 05, France
[109] Université de Caen Normandie, Côte de Nacre Boulevard Maréchal Juin, 14032 Caen, France
[110] LESIA, Observatoire de Paris, Université PSL, CNRS, Sorbonne Université, Université de Paris, 5 Place Jules Janssen, 92190 Meudon, France
[111] SRON Netherlands Institute for Space Research, Niels Bohrweg 4, 2333 CA Leiden, The Netherlands
[112] Astronomical Observatory, University of Warsaw, Al. Ujazdowskie 4, 00-478 Warszawa, Poland
[113] Scalian for CNES Centre Spatial de Toulouse, 18 Avenue Edouard Belin, 31401 Toulouse Cedex 9, France
[114] Université Rennes, CNRS, IPR (Institut de Physique de Rennes), UMR 6251, 35000 Rennes, France
[115] Shanghai Astronomical Observatory, Chinese Academy of Sciences, 80 Nandan Road, Shanghai 200030, PR China
[116] University of Chinese Academy of Sciences, No. 19(A) Yuquan Road, Shijingshan District, Beijing 100049, PR China
[117] Niels Bohr Institute, University of Copenhagen, Juliane Maries Vej 30, 2100 Copenhagen Ø, Denmark
[118] DXC Technology, Retortvej 8, 2500 Valby, Denmark
[119] Las Cumbres Observatory, 6740 Cortona Drive Suite 102, Goleta, CA 93117, USA
[120] CIGUS CITIC, Department of Nautical Sciences and Marine Engineering, University of A Coruña, Paseo de Ronda 51, 15071 A Coruña, Spain
[121] Astrophysics Research Institute, Liverpool John Moores University, 146 Brownlow Hill, Liverpool L3 5RF, UK
[122] IPAC, Mail Code 100-22, California Institute of Technology, 1200 E. California Blvd., Pasadena, CA 91125, USA
[123] MTA CSFK Lendület Near-Field Cosmology Research Group, Konkoly Observatory, MTA Research Centre for Astronomy and Earth Sciences, Konkoly Thege Miklós út 15-17, 1121 Budapest, Hungary
[124] Departmento de Física de la Tierra y Astrofísica, Universidad Complutense de Madrid, 28040 Madrid, Spain
[125] Ruđer Bošković Institute, Bijenička cesta 54, 10000 Zagreb, Croatia
[126] Villanova University, Department of Astrophysics and Planetary Science, 800 E Lancaster Avenue, Villanova, PA 19085, USA
[127] INAF – Osservatorio Astronomico di Brera, Via E. Bianchi, 46, 23807 Merate, LC, Italy
[128] STFC, Rutherford Appleton Laboratory, Harwell, Didcot OX11 0QX, UK
[129] Charles University, Faculty of Mathematics and Physics, Astronomical Institute of Charles University, V Holesovickach 2, 18000 Prague, Czech Republic
[130] Department of Particle Physics and Astrophysics, Weizmann Institute of Science, Rehovot 7610001, Israel
[131] Department of Astrophysical Sciences, Princeton University, 4 Ivy Lane, Princeton, NJ 08544, USA
[132] Departamento de Astrofísica, Centro de Astrobiología (CSIC-INTA), ESA-ESAC, Camino Bajo del Castillo s/n, 28692 Villanueva de la Cañada, Madrid, Spain
[133] naXys, University of Namur, Rempart de la Vierge, 5000 Namur, Belgium
[134] CGI Deutschland B.V. & Co. KG, Mornewegstr. 30, 64293 Darmstadt, Germany
[135] Institute of Global Health, University of Geneva, Geneva, Switzerland
[136] Astronomical Observatory Institute, Faculty of Physics, Adam Mickiewicz University, Poznań, Poland
[137] H H Wills Physics Laboratory, University of Bristol, Tyndall Avenue, Bristol BS8 1TL, UK
[138] Department of Physics and Astronomy G. Galilei, University of Padova, Vicolo dell'Osservatorio 3, 35122 Padova, Italy
[139] CERN, Esplanade des Particules 1, PO Box 1211, Geneva, Switzerland
[140] Applied Physics Department, Universidade de Vigo, 36310 Vigo, Spain
[141] Association of Universities for Research in Astronomy, 1331 Pennsylvania Ave., NW, Washington, DC 20004, USA
[142] European Southern Observatory, Alonso de Córdova 3107, Casilla 19, Santiago, Chile
[143] Sorbonne Université, CNRS, UMR7095, Institut d'Astrophysique de Paris, 98bis bd. Arago, 75014 Paris, France
[144] Faculty of Mathematics and Physics, University of Ljubljana, Jadranska ulica 19, 1000 Ljubljana, Slovenia

Appendix A: Queries used to select samples

For the OB sample, the following query was used:

```
SELECT g.*, ap.*
FROM gaiadr3.gaia_source AS g
INNER JOIN gaiadr3.astrophysical_parameters AS ap
ON g.source_id = ap.source_id
WHERE ((ap.teff_gspphot > 10000 AND
     (ap.spectraltype_esphs = 'O' OR
     ap.spectraltype_esphs = 'B' OR
     ap.spectraltype_esphs = 'A') AND ap.teff_esphs
     IS NULL) OR (ap.teff_esphs > 10000 AND
     ap.teff_gspphot > 8000) OR (ap.teff_esphs >
     10000 AND ap.teff_esphs < 50000 AND
     ap.teff_gspphot IS NULL))
AND power(g.parallax/100.,5) <
     power(10.,2.-g.phot_g_mean_mag+1.8*g.bp_rp)
```

For the RGB sample, the following query was used:

```
SELECT g.*
FROM gaiadr3.gaia_source AS g
WHERE (g.teff_gspphot<5500 and g.teff_gspphot>3000)
     and (g.logg_gspphot<3.)
```

Subsequent cross-matches to the tables containing the CBJ2021 distances and the astrometric fidelity flag were made after saving the results of this query as a user table. The final selection on $|Z| < 300$ pc and $|Z| < 1$ kpc for the OB sample and the RGB samples, respectively, was made during the creation of the maps in Section 4 and 5.

As written, these queries will pull all columns from the tables `gaia_source` and `astrophysical_parameters`. To save space, the user is recommended to pull only the columns of interest.

Appendix B: Maps of velocity uncertainties

B.1. Velocity uncertainties with Fisher formalism

We briefly explain how we estimated the uncertainties of the velocity V_k from the negative log-likelihood given in Eq. (19): First, we minimised the negative log-likelihood in order to obtain estimates of the mean velocity V_k and the dispersion σ_k^*. Second, we employed the Fisher formalism by computing the Hessian matrix of second derivatives of Eq. (19) with respect to the two fit parameters V_k and σ_k^*, and the covariance matrix of the two fit parameters was then given by the inverse of the Hessian.

We computed the first derivatives of Eq. (19) with respect to V_k and σ_k^*, and equate them to zero:

$$\frac{\partial \mathcal{L}}{\partial V_k} = -\sum_j^{N_*} \frac{v_{k,j} - V_k}{\sigma_k^{*2} + \sigma_{v_{k,j}}^2} = 0 \quad \Leftrightarrow \quad V_k = \frac{\sum_j^{N_*} \frac{v_{k,j}}{\sigma_k^{*2}+\sigma_{v_{k,j}}^2}}{\sum_j^{N_*} \frac{1}{\sigma_k^{*2}+\sigma_{v_{k,j}}^2}} \tag{B.1}$$

$$\frac{\partial \mathcal{L}}{\partial \sigma_k^*} = \frac{1}{2}\sum_j^{N_*} \left[\frac{2\sigma_k^*}{\sigma_k^{*2} + \sigma_{v_{k,j}}^2} - 2\sigma_k^* \frac{(v_{k,j} - V_k)^2}{(\sigma_k^{*2} + \sigma_{k v_{k,j}}^{*2})^2} \right] = 0. \tag{B.2}$$

Since $\sigma_k^* = 0$ is not an allowed solution because the dispersion has to be strictly positive, we can cancel out this factor from this and obtain

$$\sum_j^{N_*} \frac{1}{\sigma_k^{*2} + \sigma_{v_{k,j}}^2} = \sum_j^{N_*} \frac{(v_{k,j} - V_k)^2}{(\sigma_k^{*2} + \sigma_{k v_{k,j}}^{*2})^2}. \tag{B.3}$$

This cannot be solved analytically for σ_k^*, and we employed a numerical solution instead.

Next, we need to compute the Hessian matrix of second derivatives of $\mathcal{L}$,

$$\frac{\partial^2 \mathcal{L}}{\partial V_k^2} = \sum_j^{N_*} \frac{1}{\sigma_k^{*2} + \sigma_{v_{k,j}}^2} \tag{B.4}$$

$$\frac{\partial^2 \mathcal{L}}{\partial V_k \partial \sigma_k^*} = 2\sigma_k^* \sum_j^{N_*} \frac{v_{k,j} - V_k}{(\sigma_k^{*2} + \sigma_{k v_{k,j}}^{*2})^2} \tag{B.5}$$

$$\frac{\partial^2 \mathcal{L}}{\partial \sigma_k^{*2}} = \sum_j^{N_*} \left[4\sigma_k^{*2} \frac{(v_{k,j} - V_k)^2}{(\sigma_k^{*2} + \sigma_{k v_{k,j}}^{*2})^3} - \frac{2\sigma_k^{*2}}{(\sigma_k^{*2} + \sigma_{k v_{k,j}}^{*2})^2} \right]. \tag{B.6}$$

The last equation has already been simplified by using Eq. (B.3). We now write all the second derivatives into the Hessian matrix,

$$H = \begin{pmatrix} \frac{\partial^2 \mathcal{L}}{\partial V_k^2} & \frac{\partial^2 \mathcal{L}}{\partial V_k \partial \sigma_k^*} \\ \frac{\partial^2 \mathcal{L}}{\partial V_k \partial \sigma_k^*} & \frac{\partial^2 \mathcal{L}}{\partial \sigma_k^{*2}} \end{pmatrix}. \tag{B.7}$$

Given the numerical best-fit solutions for V_k and σ_k^*, the Hessian H is just a 2×2 matrix of numerical values that we can invert. According to the Fisher information criterion, the covariance matrix of the fit parameters is equal to the negative of the inverse Hessian. Because Eq. (19) is the negative log-likelihood, the covariance matrix is the inverse Hessian without the minus sign,

$$C = H^{-1}. \tag{B.8}$$

The standard deviation on V_k is then simply given by $\sqrt{C_{00}}$. Note that we cannot give an analytic expression for it because we cannot solve Eq. (B.3) analytically for σ_k^*, but we can compute $\sqrt{C_{00}}$ from the numerical solution for σ_k^*.

B.2. Solution for $\sigma_k^* \gg \sigma_{v_{k,j}}$

The dispersion σ_k^* may be much higher than all individual measurement errors $\sigma_{v_{k,j}}$. In this case, we can approximate $\sigma_k^{*2} + \sigma_{v_{k,j}}^2 \approx \sigma_k^{*2}$ such that Eq. (B.1) and Eq. (B.3) simplify to

$$V_k = \frac{1}{N_*}\sum_j^{N_*} v_{k,j} \quad \text{and} \quad \sigma_k^{*2} = \frac{1}{N_*}\sum_j^{N_*} (v_{k,j} - V_k)^2. \tag{B.9}$$

In this specific case, there now is an analytic solution for σ_k^*. The Hessian from Eq. (B.7) reduces to

$$H = \begin{pmatrix} \frac{N_*}{\sigma_k^{*2}} & \frac{2}{\sigma_k^{*3}} \sum_j^{N_*} (v_{k,j} - V_k) \\ \frac{2}{\sigma_k^{*3}} \sum_j^{N_*} (v_{k,j} - V_k) & 4\frac{\sum_j^{N_*} (v_{k,j} - V_k)^2}{\sigma_k^{*4}} - \frac{2N_*}{\sigma_k^{*2}} \end{pmatrix}. \tag{B.10}$$

Given $V_k = \frac{1}{N_*}\sum_j^{N_*} v_{k,j}$, we have $\sum_j^{N_*} (v_{k,j} - V_k) = 0$ such that the off-diagonal elements of H disappear and we are left with

$$H = \begin{pmatrix} \frac{N_*}{\sigma_k^{*2}} & 0 \\ 0 & 4\frac{\sum_j^{N_*} (v_{k,j} - V_k)^2}{\sigma_k^{*4}} - \frac{2N_*}{\sigma_k^{*2}} \end{pmatrix} = \begin{pmatrix} \frac{N_*}{\sigma_k^{*2}} & 0 \\ 0 & \frac{2N_*}{\sigma_k^{*2}} \end{pmatrix}. \tag{B.11}$$

Since this Hessian has a 2×2 format, we can easily invert it by hand to obtain the covariance matrix C. Indeed, we are only interested in the first element of the diagonal of C,

$$C_{00} = \frac{H_{11}}{H_{00}H_{11} - H_{01}H_{10}} = \frac{\frac{2N_*}{\sigma_k^{*2}}}{\frac{N_*}{\sigma_k^{*2}}\frac{2N_*}{\sigma_k^{*2}} - 0} = \frac{\sigma_k^{*2}}{N_*}. \tag{B.12}$$

Consequently, the uncertainty on the mean velocity V_k is approximately $\frac{\sigma_k^*}{\sqrt{N_*}}$ if the dispersion satisfies $\sigma_k^* \gg \sigma_{v_{k,j}}$.

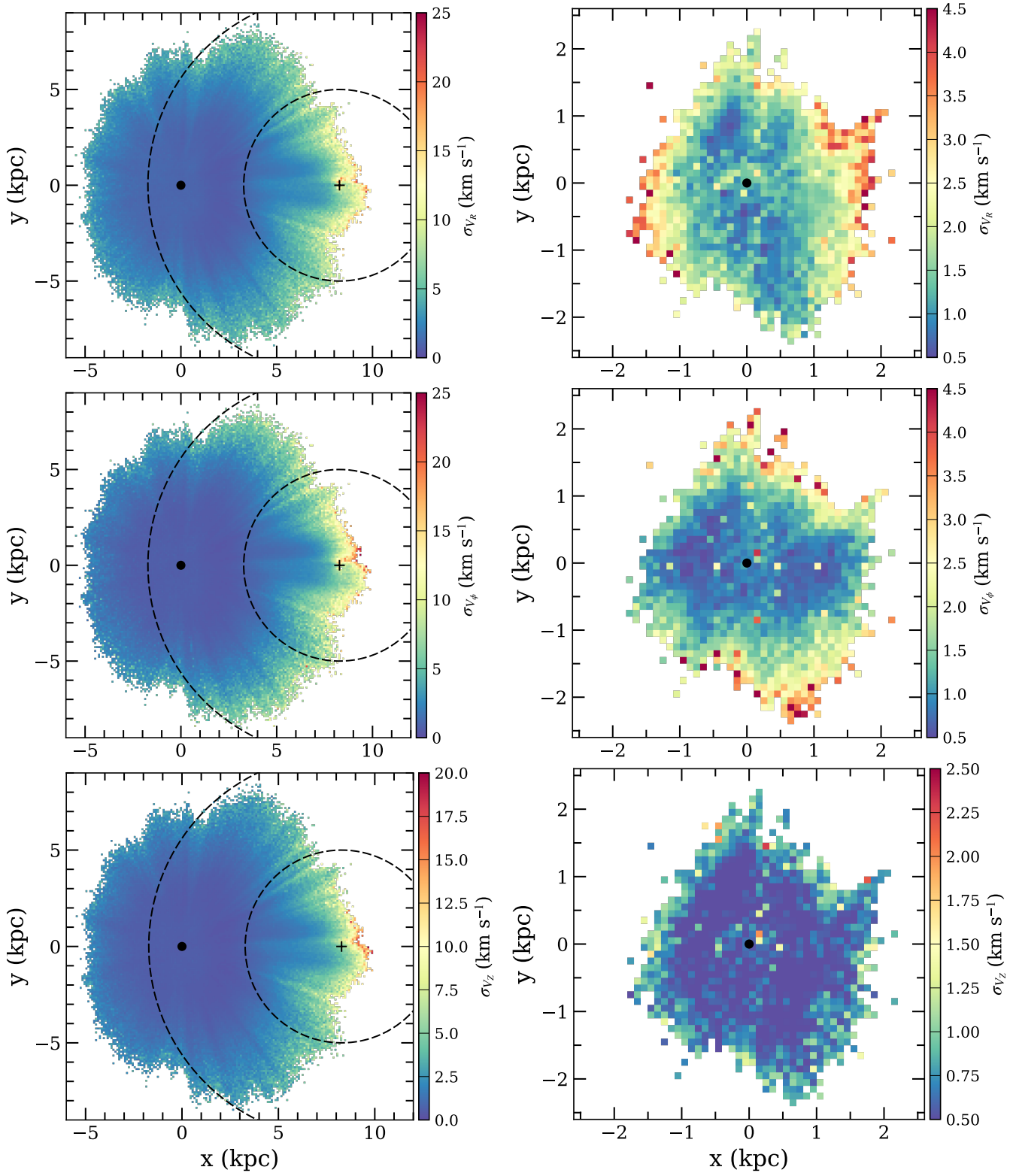


Fig. B.1. Velocity uncertainty maps for Milky Way RGB giants (left column) and OB stars (right column). From top to bottom, the radial, azimuthal, and vertical uncertainties are shown. The position of the Sun is marked by a filled circle and that of the Galactic centre by a plus sign. The velocity ranges have been chosen to enhance contrasts. These uncertainty maps can be found at the CDS in FITS format.

Appendix C: Test particle simulations and *Gaia*, mock catalogues

We used test-particle simulations to guide an interpretation of the velocity maps shown by the RGB sample in the inner regions, and no dynamical modelling was undertaken. The initial conditions, the Galactic potential, and the steps performed in the integration process are described in Romero-Gómez et al. (2015), here summarized briefly.

The initial conditions for positions and velocities were drawn for a disc density distribution following a Miyamoto-Nagai disc potential (Miyamoto & Nagai 1975) with a typical scale-height (h_z = 300 pc) and radial velocity dispersion (σ_U = 30.3 km s^{-1}) of a red clump star. We first integrated the initial conditions in the axisymmetric potential of Allen & Santillan (1991) for 10 Gyr, then we introduced the Galactic bar potential adiabatically during four bar rotations, and we integrated another four bar rotations so that the particles achieve a statistical equilibrium with the final bar potential. The Galactic bar consists of the superposition of two aligned Ferrers ellipsoids (Ferrers 1877), one modelling the triaxial bulge with a semi-major axis of 3.13 kpc, and the second modelling the long thin bar with a semi-major axis of 4.5 kpc. The bar rotates as a rigid body with a constant pattern speed of 45 km s^{-1} kpc^{-1}, placing the corotation and the outer Lindblad resonances at 4.7 kpc and 8.4 kpc, respectively.

In order to mimic the RGB sample, we generated two sets. One sample in which for each particle an absolute magnitude of $M_K = -1.61$ mag (Alves 2000) and no dispersion was assumed, and the other sample with an absolute magnitude of $M_K = -3.0$ mag and a dispersion of 1 mag, corresponding to the red clump and the bright red giant branch, respectively. We assigned an observed colour typical of a red clump star (Alves 2000). We balanced the particles in each set so that it mimics the RGB proportion of red clump stars and brighter sources and the apparent magnitude and spatial distribution. Using absorption (Drimmel et al. 2003) and extinction models (Cardelli et al. 1989), we obtained the *Gaia*, G magnitude. We followed the prescriptions described in the *Gaia* science performance webpage[8] to obtain the astrometric and spectroscopic uncertainties. In this case, because we used photogeo distances, we adopted a constant relative uncertainty in distance of 15%, but we also made tests with a relative uncertainty of 10% and 20%.

The spatial distribution (top), radial (middle), and azimuthal (bottom) velocity maps corresponding to a density distribution with a Galactic bar oriented 20° from the Sun – Galactic centre line is shown in Fig. C.1, without (left) and with (right) uncertainties. As in the RGB sample, we only show cells with at least 20 stars, and masked all others. The solid black line shows the orientation of the major axis of the bar in the simulation.

We fit the asymmetric velocity model of Eq. 20 to the mock velocity fields in order to assess to which extent the strength and phase angle of the bisymmetric perturbation can be constrained. This simple model is motivated by the presence of periodic features seen in both V_R and V_ϕ maps at small radius, which are caused by the dynamics of the bar. Furthermore, comparable forms are regularly used to model the kinematics in barred galaxies (see e.g. Spekkens & Sellwood 2007), although the axisymmetric radial component $\overline{V}_R$ is rarely derived in the literature. For a disc in relative equilibrium, this component should indeed cancel out as a function of radius. However, with the current *Gaia* data set, is evident that this is not the case in the azimuthal range covered by the RGB sample. We therefore decided to fit $\overline{V}_R$ as well with both mock and real kinematics.

Fig. C.1 shows that the angle ϕ_b that the main axis of the bisymmetry creates with $Y = 0$, the pseudo direction Sun – Galactic centre, can be measured independently using V_R or V_ϕ. This angle is that of the bar at low radius. With V_R, this angle is the direction in which the right term of Eq. 20 changes its sign, that is, $\phi_\mathrm{b} = \phi_R - \pi/4$. With V_ϕ, it is the angle in which this term is minimum, that is, $\phi_\mathrm{b} = \phi_\phi - \pi/2$. An interesting feature the middle right panel of Fig. C.1 (mock data with uncertainties) is that the direction of the change of sign of V_R is no longer perfectly aligned with the major axis of the bar, but is closer to the Sun – Galactic centre line. We thus expect from the derivation of the simple asymmetric model that ϕ_bisym is smaller than the true bar orientation.

Figure C.2 shows the amplitudes and phase angles of the bisymmetric model of V_R and V_ϕ applied to the simulation with a bar phase angle of −20°, where we masked bins with $X > 0$ to have the spatial distribution almost similar to that of the *Gaia* data. The bottom and top panels show the results obtained with and without uncertainties, respectively, to the mock variables. The asymmetric model applied to V_ϕ recovers the bar orientation within R = 2.2 kpc well, regardless of the uncertainties, while for V_R, the phase angle of the bar is only recovered when the uncertainties are not present, and is overestimated otherwise.

To understand why the bisymmetric model works better with V_ϕ than with V_R when uncertainties are added to the variables, we show in Fig. C.3 the phase angle of V_R (blue curves) and V_ϕ (green curves) obtained from a set of three simulations. The only difference between them is the relative uncertainty in distance used, namely 10%, 15%, and 20%. As expected, it shows that the larger the uncertainty in distance, the larger the difference between the recovered and the real phase angle. Interestingly, we also see that for V_ϕ the difference between the estimated bar angle and the real orientation starts to be significant, but only in the case of the largest relative uncertainty in distance of 20%. The reason for the larger discrepancy in the radial case is that geometrically, an error on the heliocentric distance translates into an incorrect azimuthal angle, and a small change in azimuth affects the radial velocity more strongly than the azimuthal component.

[8] https://www.cosmos.esa.int/web/gaia/science-performance

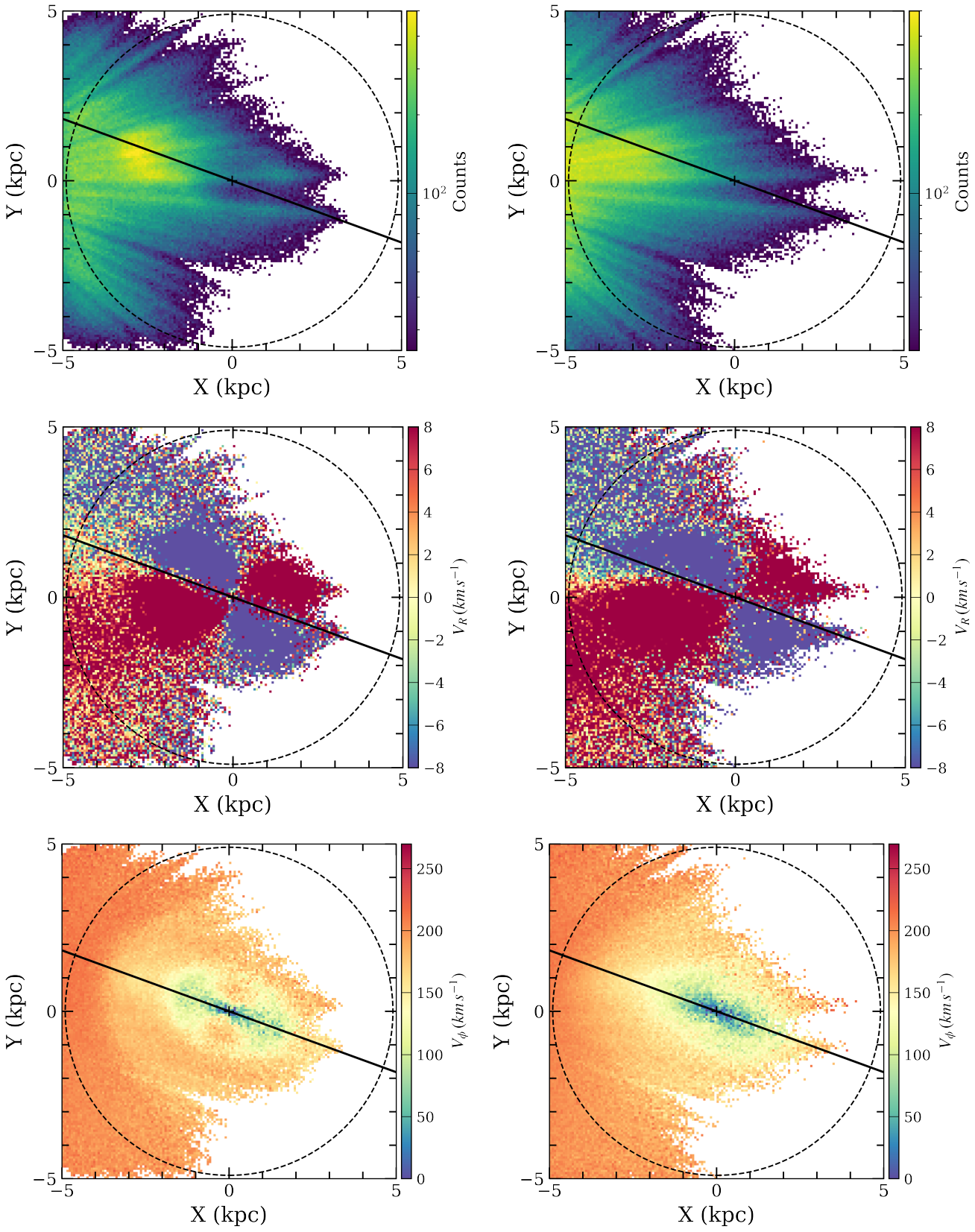


Fig. C.1. Spatial distribution (top), median V_r (middle), and median V_ϕ (bottom) from a barred test-particle simulation. Left: Variables without uncertainties. Right: Variables with uncertainties. The dashed black circle shows the corotation radius, the solid black line depicts the bar orientation angle of 20°, and the black cross shows the position of the Galactic centre.

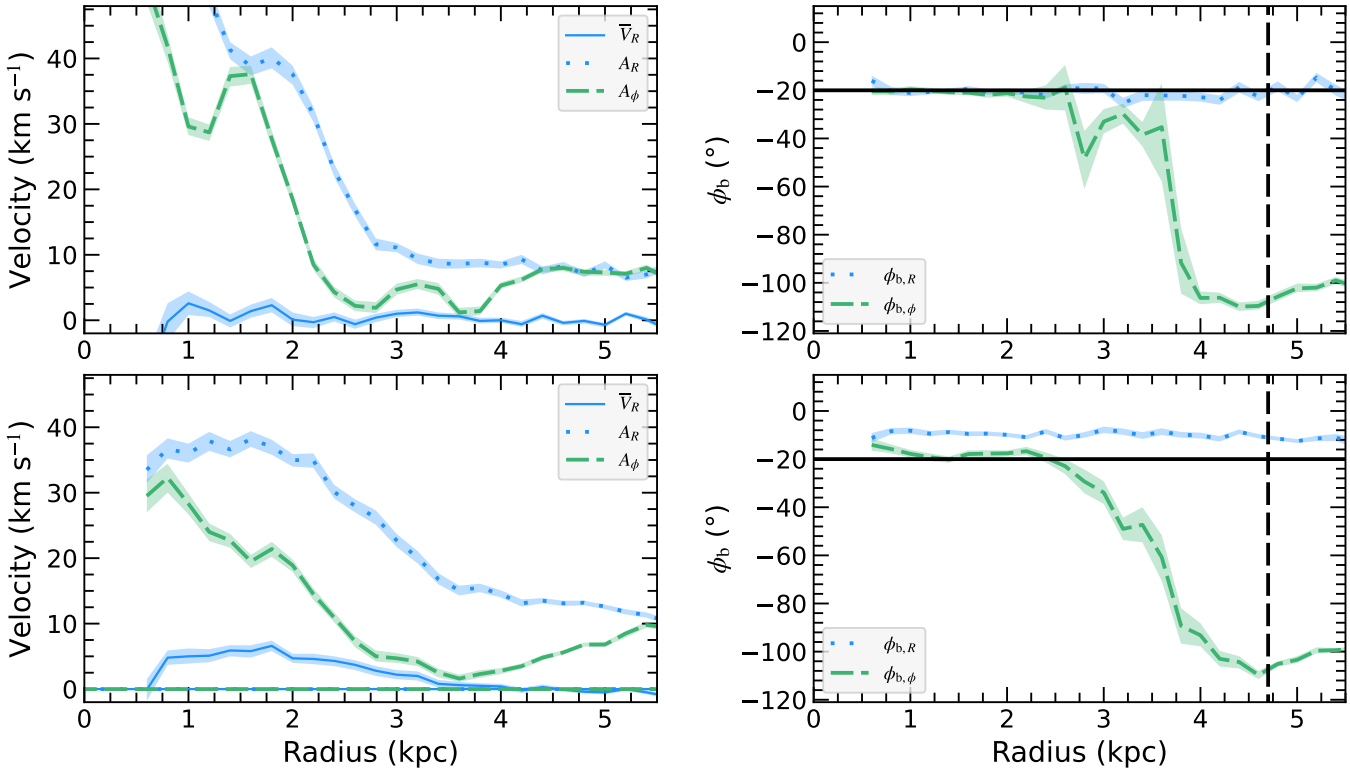


Fig. C.2. As in Fig. 19, applied to the simulation. Results for the model with and without errors are shown in the bottom and top rows, respectively.

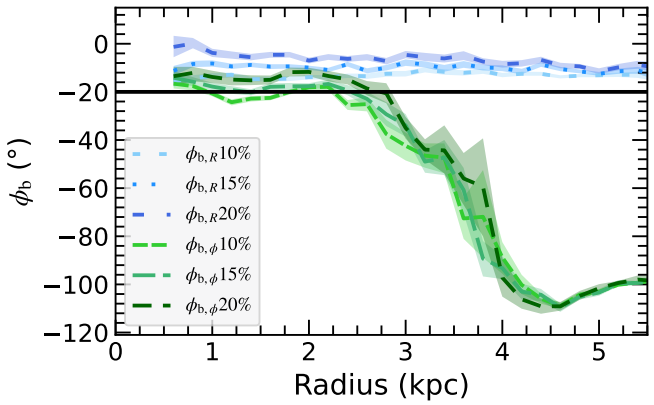


Fig. C.3. Phase angle of the bisymmetric model of V_R (blues) and V_ϕ (greens) applied to the simulation with a bar phase angle of 20° (shown as the solid black line). Different curves show a different relative uncertainty in distance applied in the simulation, namely 10% (light colour), 15% (normal colour), and 20% (dark colour).

Appendix D: Gaia funding acknowledgements

The *Gaia* mission and data processing have financially been supported by, in alphabetical order by country:

- the Algerian Centre de Recherche en Astronomie, Astrophysique et Géophysique of Bouzareah Observatory;
- the Austrian Fonds zur Förderung der wissenschaftlichen Forschung (FWF) Hertha Firnberg Programme through grants T359, P20046, and P23737;
- the BELgian federal Science Policy Office (BELSPO) through various PROgramme de Développement d'Expériences scientifiques (PRODEX) grants and the Polish Academy of Sciences – Fonds Wetenschappelijk Onderzoek through grant VS.091.16N, and the Fonds de la Recherche Scientifique (FNRS), and the Research Council of Katholieke Universiteit (KU) Leuven through grant C16/18/005 (Pushing AsteRoseismology to the next level with TESS, GaiA, and the Sloan DIgital Sky SurvEy – PARADISE);
- the Brazil-France exchange programmes Fundação de Amparo à Pesquisa do Estado de São Paulo (FAPESP) and Coordenação de Aperfeicoamento de Pessoal de Nível Superior (CAPES) - Comité Français d'Evaluation de la Coopération Universitaire et Scientifique avec le Brésil (COFECUB);
- the Chilean Agencia Nacional de Investigación y Desarrollo (ANID) through Fondo Nacional de Desarrollo Científico y Tecnológico (FONDECYT) Regular Project 1210992 (L. Chemin);
- the National Natural Science Foundation of China (NSFC) through grants 11573054, 11703065, and 12173069, the China Scholarship Council through grant 201806040200, and the Natural Science Foundation of Shanghai through grant 21ZR1474100;
- the Tenure Track Pilot Programme of the Croatian Science Foundation and the École Polytechnique Fédérale de Lausanne and the project TTP-2018-07-1171 'Mining the Variable Sky', with the funds of the Croatian-Swiss Research Programme;
- the Czech-Republic Ministry of Education, Youth, and Sports through grant LG 15010 and INTER-EXCELLENCE grant LTAUSA18093, and the Czech Space Office through ESA PECS contract 98058;
- the Danish Ministry of Science;
- the Estonian Ministry of Education and Research through grant IUT40-1;
- the European Commission's Sixth Framework Programme through the European Leadership in Space Astrometry (ELSA) Marie Curie Research Training Network (MRTN-CT-2006-033481), through Marie Curie project PIOF-GA-2009-255267 (Space AsteroSeismology & RR Lyrae stars, SAS-RRL), and through a Marie Curie Transfer-of-Knowledge (ToK) fellowship (MTKD-CT-2004-014188); the European Commission's Seventh Framework Programme through grant FP7-606740 (FP7-SPACE-2013-1) for the *Gaia* European Network for Improved data User Services (GENIUS) and through grant 264895 for the *Gaia* Research for European Astronomy Training (GREAT-ITN) network;
- the European Cooperation in Science and Technology (COST) through COST Action CA18104 'Revealing the Milky Way with *Gaia* (MW-Gaia)';
- the European Research Council (ERC) through grants 320360, 647208, and 834148 and through the European Union's Horizon 2020 research and innovation and excellent science programmes through Marie Skłodowska-Curie grant 745617 (Our Galaxy at full HD – Gal-HD) and 895174 (The build-up and fate of self-gravitating systems in the Universe) as well as grants 687378 (Small Bodies: Near and Far), 682115 (Using the Magellanic Clouds to Understand the Interaction of Galaxies), 695099 (A sub-percent distance scale from binaries and Cepheids – CepBin), 716155 (Structured ACCREtion Disks – SACCRED), 951549 (Sub-percent calibration of the extragalactic distance scale in the era of big surveys – UniverScale), and 101004214 (Innovative Scientific Data Exploration and Exploitation Applications for Space Sciences – EXPLORE);
- the European Science Foundation (ESF), in the framework of the *Gaia* Research for European Astronomy Training Research Network Programme (GREAT-ESF);
- the European Space Agency (ESA) in the framework of the *Gaia* project, through the Plan for European Cooperating States (PECS) programme through contracts C98090 and 4000106398/12/NL/KML for Hungary, through contract 4000115263/15/NL/IB for Germany, and through PROgramme de Développement d'Expériences scientifiques (PRODEX) grant 4000127986 for Slovenia;
- the Academy of Finland through grants 299543, 307157, 325805, 328654, 336546, and 345115 and the Magnus Ehrnrooth Foundation;
- the French Centre National d'Études Spatiales (CNES), the Agence Nationale de la Recherche (ANR) through grant ANR-10-IDEX-0001-02 for the 'Investissements d'avenir' programme, through grant ANR-15-CE31-0007 for project 'Modelling the Milky Way in the *Gaia* era' (MOD4Gaia), through grant ANR-14-CE33-0014-01 for project 'The Milky Way disc formation in the *Gaia* era' (ARCHEOGAL), through grant ANR-15-CE31-0012-01 for project 'Unlocking the potential of Cepheids as primary distance calibrators' (UnlockCepheids), through grant ANR-19-CE31-0017 for project 'Secular evolution of galxies' (SEGAL), and through grant ANR-18-CE31-0006 for project 'Galactic Dark Matter' (GaDaMa), the Centre National de la Recherche Scientifique (CNRS) and its SNO *Gaia* of the Institut des Sciences de l'Univers (INSU), its Programmes Nationaux: Cosmologie et Galaxies (PNCG), Gravitation Références Astronomie Métrologie (PNGRAM), Planétologie (PNP), Physique et Chimie du Milieu Interstellaire (PCMI), and Physique Stellaire (PNPS), the 'Action Fédératrice *Gaia*' of the Observatoire de Paris, the Région de Franche-Comté, the Institut National Polytechnique (INP) and the Institut National de Physique nucléaire et de Physique des Particules (IN2P3) co-funded by CNES;
- the German Aerospace Agency (Deutsches Zentrum für Luft- und Raumfahrt e.V., DLR) through grants 50QG0501, 50QG0601, 50QG0602, 50QG0701, 50QG0901, 50QG1001, 50QG1101, 50QG1401, 50QG1402, 50QG1403, 50QG1404, 50QG1904, 50QG2101, 50QG2102, and 50QG2202, and the Centre for Information Services and High Performance Computing (ZIH) at the Technische Universität Dresden for generous allocations of computer time;
- the Hungarian Academy of Sciences through the Lendület Programme grants LP2014-17 and LP2018-7 and the Hungarian National Research, Development, and Innovation Office (NKFIH) through grant KKP-137523 ('SeismoLab');
- the Science Foundation Ireland (SFI) through a Royal Society – SFI University Research Fellowship (M. Fraser);

– the Israel Ministry of Science and Technology through grant 3-18143 and the Tel Aviv University Center for Artificial Intelligence and Data Science (TAD) through a grant;
– the Agenzia Spaziale Italiana (ASI) through contracts I/037/08/0, I/058/10/0, 2014-025-R.0, 2014-025-R.1.2015, and 2018-24-HH.0 to the Italian Istituto Nazionale di Astrofisica (INAF), contract 2014-049-R.0/1/2 to INAF for the Space Science Data Centre (SSDC, formerly known as the ASI Science Data Center, ASDC), contracts I/008/10/0, 2013/030/I.0, 2013-030-I.0.1-2015, and 2016-17-I.0 to the Aerospace Logistics Technology Engineering Company (ALTEC S.p.A.), INAF, and the Italian Ministry of Education, University, and Research (Ministero dell'Istruzione, dell'Università e della Ricerca) through the Premiale project 'MIning The Cosmos Big Data and Innovative Italian Technology for Frontier Astrophysics and Cosmology' (MITiC);
– the Netherlands Organisation for Scientific Research (NWO) through grant NWO-M-614.061.414, through a VICI grant (A. Helmi), and through a Spinoza prize (A. Helmi), and the Netherlands Research School for Astronomy (NOVA);
– the Polish National Science Centre through HARMONIA grant 2018/30/M/ST9/00311 and DAINA grant 2017/27/L/ST9/03221 and the Ministry of Science and Higher Education (MNiSW) through grant DIR/WK/2018/12;
– the Portuguese Fundação para a Ciência e a Tecnologia (FCT) through national funds, grants SFRH/BD/128840/2017 and PTDC/FIS-AST/30389/2017, and work contract DL 57/2016/CP1364/CT0006, the Fundo Europeu de Desenvolvimento Regional (FEDER) through grant POCI-01-0145-FEDER-030389 and its Programa Operacional Competitividade e Internacionalização (COMPETE2020) through grants UIDB/04434/2020 and UIDP/04434/2020, and the Strategic Programme UIDB/00099/2020 for the Centro de Astrofísica e Gravitação (CENTRA);
– the Slovenian Research Agency through grant P1-0188;
– the Spanish Ministry of Economy (MINECO/FEDER, UE), the Spanish Ministry of Science and Innovation (MICIN), the Spanish Ministry of Education, Culture, and Sports, and the Spanish Government through grants BES-2016-078499, BES-2017-083126, BES-C-2017-0085, ESP2016-80079-C2-1-R, ESP2016-80079-C2-2-R, FPU16/03827, PDC2021-121059-C22, RTI2018-095076-B-C22, and TIN2015-65316-P ('Computación de Altas Prestaciones VII'), the Juan de la Cierva Incorporación Programme (FJCI-2015-2671 and IJC2019-04862-I for F. Anders), the Severo Ochoa Centre of Excellence Programme (SEV2015-0493), and MICIN/AEI/10.13039/501100011033 (and the European Union through European Regional Development Fund 'A way of making Europe') through grant RTI2018-095076-B-C21, the Institute of Cosmos Sciences University of Barcelona (ICCUB, Unidad de Excelencia 'María de Maeztu') through grant CEX2019-000918-M, the University of Barcelona's official doctoral programme for the development of an R+D+i project through an Ajuts de Personal Investigador en Formació (APIF) grant, the Spanish Virtual Observatory through project AyA2017-84089, the Galician Regional Government, Xunta de Galicia, through grants ED431B-2021/36, ED481A-2019/155, and ED481A-2021/296, the Centro de Investigación en Tecnologías de la Información y las Comunicaciones (CITIC), funded by the Xunta de Galicia and the European Union (European Regional Development Fund – Galicia 2014-2020 Programme), through grant ED431G-2019/01, the Red Española de Supercomputación (RES) computer resources at MareNostrum, the Barcelona Supercomputing Centre – Centro Nacional de Supercomputación (BSC-CNS) through activities AECT-2017-2-0002, AECT-2017-3-0006, AECT-2018-1-0017, AECT-2018-2-0013, AECT-2018-3-0011, AECT-2019-1-0010, AECT-2019-2-0014, AECT-2019-3-0003, AECT-2020-1-0004, and DATA-2020-1-0010, the Departament d'Innovació, Universitats i Empresa de la Generalitat de Catalunya through grant 2014-SGR-1051 for project 'Models de Programació i Entorns d'Execució Parallels' (MPEXPAR), and Ramon y Cajal Fellowship RYC2018-025968-I funded by MICIN/AEI/10.13039/501100011033 and the European Science Foundation ('Investing in your future');
– the Swedish National Space Agency (SNSA/Rymdstyrelsen);
– the Swiss State Secretariat for Education, Research, and Innovation through the Swiss Activités Nationales Complémentaires and the Swiss National Science Foundation through an Eccellenza Professorial Fellowship (award PCEFP2_194638 for R. Anderson);
– the United Kingdom Particle Physics and Astronomy Research Council (PPARC), the United Kingdom Science and Technology Facilities Council (STFC), and the United Kingdom Space Agency (UKSA) through the following grants to the University of Bristol, the University of Cambridge, the University of Edinburgh, the University of Leicester, the Mullard Space Sciences Laboratory of University College London, and the United Kingdom Rutherford Appleton Laboratory (RAL): PP/D006511/1, PP/D006546/1, PP/D006570/1, ST/I000852/1, ST/J005045/1, ST/K00056X/1, ST/K000209/1, ST/K000756/1, ST/L006561/1, ST/N000595/1, ST/N000641/1, ST/N000978/1, ST/N001117/1, ST/S000089/1, ST/S000976/1, ST/S000984/1, ST/S001123/1, ST/S001948/1, ST/S001980/1, ST/S002103/1, ST/V000969/1, ST/W002469/1, ST/W002493/1, ST/W002671/1, ST/W002809/1, and EP/V520342/1.

The GBOT programme uses observations collected at (i) the European Organisation for Astronomical Research in the Southern Hemisphere (ESO) with the VLT Survey Telescope (VST), under ESO programmes 092.B-0165, 093.B-0236, 094.B-0181, 095.B-0046, 096.B-0162, 097.B-0304, 098.B-0030, 099.B-0034, 0100.B-0131, 0101.B-0156, 0102.B-0174, and 0103.B-0165; and (ii) the Liverpool Telescope, which is operated on the island of La Palma by Liverpool John Moores University in the Spanish Observatorio del Roque de los Muchachos of the Instituto de Astrofísica de Canarias with financial support from the United Kingdom Science and Technology Facilities Council, and (iii) telescopes of the Las Cumbres Observatory Global Telescope Network.